AD-A254 854

②

COMPRESSIBLE MIXING LAYERS WITH AND WITHOUT PARTICLES

M. Samimy, G.S. Elliott, D.D. Glawe,
M.F. Reeder, and S.A. Arnette

Department of Mechanical Engineering
The Ohio State University
Columbus, Ohio 43210

DTIC
S ELECTE
SEP 03 1992
A D

Technical Report MEMS-92-101

August 1992

403200

92-23936

92 8 28 039

COMPRESSIBLE MIXING LAYERS WITH AND WITHOUT PARTICLES

M. Samimy*, G.S. Elliott**, D.D. Glawe**,
M.F. Reeder**, and S.A. Arnette**

Department of Mechanical Engineering
The Ohio State University
Columbus, Ohio 43210

Technical Report MEMS-92-101

Sponsored by

August 1992

DTIC QUALITY INSPECTED 3

* Associate Professor
** Graduate Student

ABSTRACT

An extensive experimental research program has been carried out to explore the effects of compressibility in high Reynolds number turbulent free mixing layers. Three mixing layers with convective Mach numbers of 0.51 (Case 1), 0.64 (Case 3), and 0.86 (Case 2) were investigated. While Case 1 marks the onset of the compressibility effect on the mixing layer growth rate, the vorticity growth rate of Case 3 is approximately 50% less than that of an incompressible mixing layer with the same velocity ratio. Various experimental techniques such as laser Doppler velocimetry, two-point space-time correlations, filtered Rayleigh scattering based flow visualizations, and conventional laser sheet lighting have been utilized. The results indicate that as the compressibility level is increased 1) the mixing layer growth rate and the entrainment and dispersion of solid particles are substantially decreased, 2) the spatial correlation levels are drastically reduced, 3) all three measured components of the Reynolds stress ($\sigma_u/\Delta U$, $\sigma_v/\Delta U$, and $\overline{uv}/\Delta U^2$) are decreased, 4) the extent of the turbulent mixing region is significantly decreased, and 5) the large scale structures become more three-dimensional, less organized, and predominately oblique. The effect of compressibility is more pronounced on the Reynolds shear stress than on the normal stresses, as evidenced by the fact that the correlation coefficient($R_{uv} = -\overline{uv}/\sigma_u\sigma_v$) significantly decreases with increasing compressibility, especially toward the edges of the mixing layer. The anisotropy ratio (σ_u/σ_v) remains relatively constant for all three M_c cases indicating that the compressibility effect is similar on the two normal components of Reynolds stress. The large scale structures in the low compressibility mixing layer ($M_c = 0.51$) are two-dimensional, aligned in the spanwise direction, and possess well defined braid and core regions similar to the structures of incompressible mixing layers. For a range of Stokes numbers, these structures are strong enough to entrain solid particles, originally present in the subsonic freestream, into the mixing region and eject some of them into the supersonic freestream. However, the structures of the highly compressible mixing layer ($M_c = 0.86$) are spanwise-oblique with angles in the range of approximately $\pm 70°$, highly three-dimensional, and much less organized than the structures of Case 1 ($M_c = 0.51$). Two-point space-time correlations suggest the structures resemble the horse-shoe type vortices observed in wall bounded shear layers. These structures lack the ability to entrain and disperse particles.

ACKNOWLEDGEMENTS

TABLE OF CONTENTS

LIST OF TABLES

LIST OF FIGURES

v

NOMENCLATURE

Roman Symbols

a_1 Speed of sound in the supersonic free stream

a_2 Speed of sound in the subsonic free stream

b   Shear layer thickness, between $0.1U^*$ and $0.9U^*$

d_p Particle diameter

M_c Convective Mach number

M_{c1} Convective Mach number of supersonic stream

M_{c2} Convective Mach number of subsonic stream

R_{uv} Correlation coefficient

St   Stokes number

St_δ Dimensional Stokes number, $(St) \times (\delta)$

U   Streamwise mean flow velocity

U^* $(U-U_2)/(U_1-U_2)$

U_c Convective velocity of large scale structures

U_1 Supersonic free stream velocity

U_2 Subsonic free stream velocity

u   Streamwise velocity fluctuations

v   Lateral velocity fluctuations

x   Distance from the trailing edge of the splitter plate in the direction of the free stream flow; streamwise; $x=0$ at the splitter plate trailing edge

x_0 Location at virtual origin

y   Axis perpendicular to both the flow direction and the splitter plate edge; lateral; $y=0$ at the splitter plate level

y_{ref} Lateral location where the experimentally measured U_c is equal to the theoretical U_c

$y_{0.5}$ Lateral location where $U=(U_1+U_2)/2$

y^* Either $(y-y_{ref})/\delta_w$ or $(y-y_{0.5})/\delta_w$

z   Distance from the center of the tunnel parallel to the edge of the splitter plate; spanwise.

Greek Symbols

β Angle of large scale structures in the x-z plane

γ Ratio of specific heats

γ_1 Ratio of specific heats for the supersonic stream

γ_2 Ratio of specific heats for the subsonic stream

ΔU $U_1 - U_2$

δ Flow length scale

δ_w Vorticity thickness

δ_1 Incoming supersonic stream boundary layer thickness

η Similarity parameter; Eqn. 9

θ_1 Incoming supersonic stream momentum thickness

μ Absolute fluid viscosity

ρ_f Fluid density

ρ_p Particle material density

ρ_1 Supersonic free stream density

ρ_2 Subsonic free stream density

σ Spread rate parameter; Eqn. 9

σ_u rms streamwise velocity fluctuations

σ_v rms lateral velocity fluctuations

τ Time shift of peak correlation levels

τ_f Fluid time scale

τ_p Particle time scale

Subscripts

c   Compressible

i   Incompressible

1   Supersonic free stream

2   Subsonic free stream

1.0 INTRODUCTION

The combustion chamber of a scramjet engine, the exhaust nozzle of a commercial or a military aircraft, and a supersonic ejector pump are a few examples of engineering systems whose performance relies heavily on the understanding of compressible mixing layers. The main goal in designing these systems is to achieve efficient mixing and combustion in the first system, to eliminate noise and/or plume signature in the second system, and to have an efficient pumping capability in the last system. These goals can only be achieved by designing systems based on a fundamental understanding of the structure of compressible mixing layers.

The well known mixing layer entrainment and growth rate reduction with increasing Mach number in single-stream free mixing layers [e.g., Birch and Eggers 1972] was attributed for a long time to the density gradient across the mixing layer rather than the compressibility, even though Morkovin in a 1961 paper hypothesized compressibility effects in free mixing layers [1961 and 1991, also see Bradshaw 1977]. This erroneous notion was finally refuted by Brown and Roshko's variable density, incompressible mixing layer experiments [1974].

For about a decade after Brown and Roshko's experiment, there was no major progress on identifying a compressibility parameter to account for the reduced growth rate in mixing layers. However, the past several years have witnessed substantial research activities in the field of compressible mixing layers accompanied by a noticeable improvement in our understanding of these flows. Although major hurdles on both the experimental and computational fronts have made attaining success in exploring these flows difficult, progress has been made. This active and productive compressible mixing layer research era started about the time a compressibility parameter was identified by Bogdanoff [1983] based on a theoretical analysis and by Papamoschou and Roshko [1988] based on an experimental work. This parameter, called the convective Mach number, M_c, by Papamoschou and Roshko, is derived in a frame of reference travelling with the large scale structures in the flow and has been shown to correlate the reduction in growth rate quite well [e.g., Papamoschou and Roshko 1988, Bogdanoff 1983].

The renewed interest in developing an air-breathing hypersonic vehicle with some sort of supersonic combustion ramjet engine and the crucial role of compressible flow entrainment and mixing in such a system prompted an intense period of research on various aspects of

compressible mixing layers using both experimental and computational/theoretical techniques. A brief review of the experimental and computational/ theoretical research findings from various research groups is presented in this chapter. The intention here is not a comprehensive review, but rather an attempt to put the research conducted on this subject by the Ohio State University group in perspective.

1.1 Review of Experimental Research

1.1.1 Mean Flow and Turbulence Fields: The assessment of the effect of compressibility on the growth rate requires measurement of the mean mixing layer thickness at multiple streamwise locations with either a simple schlieren/shadowgraph system or a stagnation pressure probe [Chinzei et al. 1986, Papamoschou and Roshko 1988 Gutmark et al. 1991, and Clemens and Mungal 1992], or measurement of velocity profiles at multiple streamwise locations using laser Doppler velocimetry (LDV) or hot-wire anemometry [Ikawa and Kubota 1975, Petrie et al. 1986, Samimy et al. 1986, Samimy and Elliott 1990, Elliott and Samimy 1990, Goebel and Dutton 1991, Bonnet et al. 1992, and Barre et al. 1992]. All of these experiments, and some not referenced here, have shown that as the compressibility level increases the mixing layer growth rate decreases.

Turbulence and mean velocity information in compressible mixing layers are much more scarce than growth rate data due to the inherent difficulties of most experimental techniques in these flows. Recent LDV data [Samimy and Elliott 1990, Elliott and Samimy 1990, and Bonnet et al. 1992] and hot-wire data [Barre et al. 1992] all show significant suppression of both Reynolds normal and shear stresses due to compressibility effects. However, the anisotropy of the turbulence does not seem to be significantly affected by compressibility. An exception to these results are the data obtained by Goebel and Dutton [1991]. These data show that compressibility reduces the Reynolds shear stress and the lateral turbulence intensity, confirming the results of others, but does not substantially affect the streamwise turbulence intensity, which does not agree with other results. Barre et al.[1992] have shown that the trend in the reduction of Reynolds shear stress with M_c follows very closely that of the growth rate. This is expected in light of the fact that large scale structures are the major contributors to both the Reynolds shear stresses and the entrainment of free stream fluid into the mixing layer. Elliott and Samimy

2

[1990] and Bonnet et al.[1992] have used higher order moments of turbulence such as the skewness and flatness to show that compressibility suppresses both the breadth of the turbulent mixing region and the extension of large scale structures or 'tongues' into the free stream, which is the dominant mechanism for the entrainment of free stream fluid into the mixing layer. This is in obvious accord with the reduced growth rate due to compressibility.

1.1.2 Large Scale Structures: The observation of large scale spanwise structures in incompressible planar free shear layers by Brown & Roshko [1974] drastically altered researchers' perceptions of mixing and entrainment processes in these flows. These structures were initially thought to be a manifestation of low Reynolds number flows, thus reminiscent of transition to turbulence. However, similar large scale structures were later observed in higher Reynolds number mixing layers by Dimotakis & Brown [1976] and others. Later studies by Jimenez [1983], Bernal & Roshko [1986], and Lasheras et al. [1986] showed that streamwise streaks or structures are embedded within the spanwise large structures.

Large scale structures have also been observed with the schlieren technique in high Reynolds number compressible mixing layers by some researchers [Papamoschou and Roshko 1988, Elliott and Samimy 1990, McIntyre and Settles 1991 and Clemens and Mungal 1992]. However, some other researchers have reported no discernable large scale structures [Goebel and Dutton 1991]. Difficulties in detecting the large structures in high Reynolds number compressible flows arise mostly from their three-dimensionality, decreased strength, and decreased degree of organization relative to the structures of incompressible mixing layers. Because of the high Reynolds numbers associated with compressible mixing layers, the large structures tend to be concealed by small scale turbulence. As a result, large scale structure detection with the schlieren technique can be accomplished only with a knife edge set high enough to filter out the gradients associated with the small scale turbulence. This knife edge height is substantially higher than that normally used to obtain schlieren photographs. It is also important to note that the inherent line-of-sight averaging of schlieren technique tends to mask the structures given the three-dimensional nature of the large scale structures in highly compressible cases.

Mie and/or Rayleigh scattering based flow visualizations have been used to identify and characterize large scale structures in compressible mixing layers [Fourguette et al. 1991,

Messersmith et al. 1991, Clemens et al. 1992, and Elliott et al. 1992]. These results show that the structures become increasingly disorganized and three-dimensional at higher compressibility levels [Clemens and Mungal 1992 and Elliott et al. 1992] and the nominally two-dimensional structures become oblique with respect to the spanwise direction in highly compressible mixing layers [Elliott et al. 1992].

Some data have also been obtained on these structures using two-point pressure correlation measurements [Shau and Dolling 1990 and Samimy et al. 1992]. These data show that the streamwise correlation levels drop drastically with increasing probe separation for high compressibility cases [Samimy et al. 1992]. The spanwise correlations show a time shift in the maximum correlation level and a significant variation, rather than a monotonous decrease, in the maximum correlation level with increasing spanwise probe distance [Samimy et al. 1992]. These findings confirm the flow visualization results on the obliqueness and increased three-dimensionality of structures at higher compressibility levels. On this note, a recent experimental work by McLaughlin et al. [1992] in a low Reynolds number mixing layer indicates that highly compressible mixing layers are much more receptive to oblique forcing than two-dimensional forcing.

1.1.3 The Convective Mach Number Issue: As discussed earlier, the convective Mach number is a Mach number based on a frame of reference travelling with large structures in the flow, and is defined for the two streams of the mixing layer by Papamoschou and Roshko [1988] as:

$$M_{cl} = \frac{U_1 - U_c}{a_1} \tag{1}$$

$$M_{c2} = \frac{U_c - U_2}{a_2} \tag{2}$$

In these equations subscripts 1 and 2 refer to the high and low speed streams, respectively, U is the free stream velocity, 'a' is the speed of sound, and U_c is the convection velocity of the structures which is given by:

4

$$U_c = \frac{a_1 U_2 + a_2 U_1}{a_1 + a_2} \tag{3}$$

Assuming that the streamlines from both streams will isentropically stagnate, in the braid region of a structure, Papamoschou and Roshko showed that $M_{c1} = M_{c2}$ if $\gamma_1 = \gamma_2$ where γ is the specific heats ratio of the gas. In fact, even with different γ's, the convective Mach numbers are relatively close.

Experimental results have shown that in some supersonic convective Mach number cases, the M_c values for the two streams are vastly different when the convective velocity is obtained experimentally and Eqns. 1 and 2 are used to calculate M_c's [Papamoschou 1991 and McIntyre and Settles 1991]. This is because the measured convection velocity tends to be close to one of the two free stream velocities. Two assumptions, other than the isentropic stagnation assumption, are invoked in obtaining $M_{c1} = M_{c2}$. They are: (1) there is a roll up in the flow with well defined core and braid regions and (2) the structures are two-dimensional and extend from one free stream to the other. The planar flow visualizations of Clemens and Mungal [1992] and Elliott et al.[1992] and two-point correlation results of Samimy et al.[1992] show that assumptions (1) and (2) are not valid even for subsonic convective Mach numbers ($M_c = 0.79$ and 0.86). The results show highly three-dimensional structures with no well defined core and braid regions. In fact, the results using two-point correlations show major variation in the convective velocity across the mixing layer with the convective velocity being close to the local velocity [Samimy et al. 1992]. Therefore, it is not surprising to see convection velocities close to free stream velocities if schlieren photographs [Papamoschou 1991 and McIntyre and Settles 1991] are used to obtain a convection velocity. As will be discussed later, an inviscid stability analysis by Jackson and Grosch [1989] for a single-stream flow exhausting into a stagnant ambient has shown that two families of instability waves exist for supersonic convective Mach numbers, one supersonic with respect to the stagnant ambient which they termed fast mode and the other supersonic with respect to the moving stream which they termed slow mode. Whether the observed experimental results are manifestations of these two families of stabilities is not

clear. It is possible that in a given experiment one of these two modes is excited; however, more experimental work is needed to clarify this issue.

The argument above does not undermine the convective Mach number concept. If Eqn. 3 is substituted into Eqns. 1 or 2, the expression for the convective Mach number becomes:

$$M_c = \frac{U_1 - U_2}{a_1 + a_2} \qquad (4)$$

which simply states that the convective Mach number is the ratio of the velocity difference across the mixing layer to twice the average speed of sound of the two streams. Some researchers have used what they termed a relative Mach number, which is simply twice the convective Mach number obtained from Eqn. 4 (e.g., Ragab and Wu 1989). Using the convective Mach number in this context does not pose any problem and in fact has proven over and over to correlate the compressibility effect relatively well. However, trying to measure U_c in highly compressible flows based on a few structures will not be useful. This issue will be further discussed below.

1.1.4 Mixing Enhancement Efforts: In the wake of the finding discussed above that compressibility significantly reduces the turbulent momentum exchange and thus the mixing rate in free mixing layers, some sort of enhancement mechanism will be needed in most of the engineering systems relying on efficient compressible mixing. Various attempts have been made with conflicting and inconclusive results, at best. It is fair to say that compressible mixing layers are relatively insensitive to perturbations. This can be clearly seen in schlieren photographs of mixing layers which are formed with unmatched static pressures at the trailing edge of the splitter plate in wind tunnels with a small test section. Even in such extreme cases, the mixing layer thickness, after many successive interactions with the reflected waves, does not seem to change substantially.

Some of the techniques that have been used to enhance mixing in two-dimensional mixing layers are: vortex generators in the incoming boundary layer [Papamoschou 1991 and Dolling et al. 1990], shock wave interaction with the incoming boundary layer [Shau and Dolling 1990 and Clemens and Mungal 1992] or with the mixing layer [Clark et al. 1988, Samimy et al. 1989 and 1991a], and a lobed splitter plate [Tillman et al. 1992]. Examples of

mixing enhancement attempts in jets are a swirling inlet flow [Naughton et al. 1989] and vortex generators at the nozzle exit [Samimy et al. 1991b and Zaman et al. 1992]. Of the cases mentioned, the shock interaction at the splitter plate [Clemens and Mungal, 1992], the lobed mixer [Tillman et al. 1992], and vortex generators at the jet exit [Samimy et al. 1991b and Zaman et al. 1992] have shown major impact on the mixing layer. However, the enhancement has been shown only in terms of the deflection and distortion of the mixing layer in the first case. The primary intention in the last two cases has been noise reduction rather than mixing enhancement. Therefore, further exploration of these techniques is needed for more concrete conclusions.

1.1.5 Particle Dispersion in Mixing Layers: Presently, gaseous, liquid, and solid fuels are all being considered to fuel the scramjet engine for an airbreathing hypersonic vehicle. Each one possesses advantages and disadvantages relative to the others. While mixing of gases in a compressible environment has received considerable attention, the dispersion of solid or liquid particles has definitely not. The dispersion of liquid and solid particles in a combustor using liquid or solid fuels is a controlling factor in determining the stability and efficiency of such an engine [e.g., Waltrup 1987 and Snyder et a. 1990]. Recent numerical simulations [Crowe et al. 1985 and 1988, and Chein and Chung 1988] and experiments [Kamalu et al. 1988 and 1989, Lazaro and Lasheras 1989, and Longmire 1990] have shown that the extent of particle dispersion in incompressible mixing layers is largely a function of the Stokes number (St). The Stokes number is a time scale ratio, the ratio of a characteristic flow time scale (τ_f) to a particle response time scale (τ_p).

$$St = \frac{\tau_p}{\tau_f} \qquad (5)$$

These results suggest there are three ranges of particle response to fluid motion depending on the value of the Stokes number. For small Stokes numbers (Category 1), the particles respond to changes in the flow and thus closely follow the fluid motion. For large Stokes numbers (Category 3), the particles are nearly unaffected by changes in the flow and disperse much less than the fluid. For mid-size Stokes numbers (Category 2), the particles seem

to become entrapped in the vortices (large scale structures) and flung outward by centrifugal forces. This centrifuging effect results in particles dispersing more than the carrier fluid. There seems to be a general agreement among researchers on the dependence of particle dispersion on the Stokes number and on the existence of the three categories discussed above, however, the exact Stokes number ranges for these three categories depend on the definition of τ_f, which generally differs between investigators.

For a free mixing layer, the characteristic flow time scale (τ_f) reflects the time scale of the large scale structures which dominate the entrainment in these flows. One simple representation of τ_f is the ratio of the width of the mixing layer (δ, large eddy length scale) to the velocity difference between the two free streams on either side of the shear layer ($\Delta U = U_1 - U_2$, large eddy velocity scale). This expression is given by:

$$\tau_f = \frac{\delta}{\Delta U} \tag{6}$$

The particle response time scale (τ_p) is the time required for a particle released from rest to accelerate to 63% of a constant free stream velocity, assuming a spherical particle and Stokes drag. The particle response time is given by:

$$\tau_p = \frac{d_p^2(\rho_f + 2\rho_p)}{36\mu} \tag{7}$$

If $\rho_f << \rho_p$ the above equation reduces to a simpler form given by:

$$\tau_p = \frac{d_p^2\rho_p}{18\mu} \tag{8}$$

Direct numerical simulation results of Samimy and Lele [1990 and 1991] in mixing layers with a low compressibility level ($M_c < 0.6$) show that both the dependency of the dispersion on Stokes number and the existence of a range of Stokes numbers where the dispersion of particles is much higher than the dispersion of fluid itself are similar to those of

8

the incompressible mixing layers, hence no observable compressibility effect. However, recent experimental results [Glawe 1991 and Glawe and Samimy 1992] show significant compressibility effects at $M_c = 0.86$.

1.2 Review of Computational/Theoretical Research

Inviscid stability analyses [e.g., Ragab and Wu 1989] and direct numerical simulations [e.g. Lele 1989 and Sandham and Reynolds 1991] have shown that the trend in the reduction of the maximum instability wave growth rate with M_c is very similar to the experimentally observed mixing layer growth rate reduction. This surprisingly close similarity merely points to the inviscid nature of the large-scale mixing and entrainment. Following this finding, many other aspects of compressible mixing have been explored, of which only some have been confirmed experimentally. Inviscid stability analyses [e.g. Ragab and Wu 1989 and Sandham and Reynolds 1991] and three-dimensional direct numerical simulations [Sandham and Reynolds 1991] have shown that at higher convective Mach numbers, spanwise-oblique instability waves have much higher growth rates than two-dimensional waves. This has been verified by limited experimental data using two-point correlations by Samimy et al. [1992] and visualizations by Elliott et al. [1992] in high Reynolds number mixing layers and using schlieren photography by McLaughlin et al. [1992] in low Reynolds number mixing layers. The aforementioned inviscid stability analysis of Jackson and Grosch [1989] for a single-stream flow exhausting into stagnant ambient air has shown that two families of instability waves exist in supersonic convective Mach numbers, one supersonic with respect to the stagnant ambient which they termed fast mode and the other supersonic with respect to the moving stream which they termed slow mode. Whether the observed experimental results, which show that M_{c1} and M_{c2} are different for theoretical supersonic M_c [Papamoschou 1991 and McIntyre and Settles 1991], are manifestations of these two families of stabilities is not clear. It is possible that in a given experiment one of these two modes is excited. However, more experimental work is needed to clarify this issue.

While the stability analyses discussed above were conducted with no physical boundaries, several researchers have investigated compressible mixing layers within a rectangular channel [Tam and Hu 1989, Soetrisno et al. 1989, Morris and Giridharan 1991, and Lu and Wu 1991]. It seems that when the convective Mach number is supersonic, a strong

interaction between the shear layer instabilities and the channel acoustics produce new instability modes [Tam and Hu 1989, Soetrisno et al. 1989, and Lu and Wu 1991]. It has also been shown that the aspect ratio of the channel plays a major role in the stability waves' growth rate and that one could maximize the instability growth rates by judicious selection of the aspect ratio [Morris and Giridharan 1991].

Even though experimental, inviscid linear stability, and some direct numerical simulation results show several similarities in terms of shear layer growth rate reduction with M_c, obliquity of structures at high M_c values, and other trends, one should keep in mind that the Reynolds number in almost all the experimental mixing layers discussed earlier is very high and the flows are fully turbulent. Therefore, nonlinear and viscous effects which govern the interactions between different scales are important, and cannot be ignored. Unfortunately, direct numerical simulations are very far away from being capable of including a range of scales similar to that found in experiments. Thus, a need for improved turbulence modeling arises. A new generation of turbulence modeling which directly includes the effect of compressibility in the dissipation equation [Zeman 1990, and Sarkar and Lokshmanan 1991] seems to correctly predict at least the trend of decreasing Reynolds stresses with increasing compressibility. Also, a recent diffusion type model which casts the equations in terms of a convective frame of reference and the convective Mach number seems to predict the compressibility effect quite well [Barre et al. 1992].

2.0 EXPERIMENTAL FACILITY AND TECHNIQUES

All the experiments were conducted at the Ohio State University Aeronautical and Astronautical Research Laboratory (AARL). At AARL, the cold and dry air generated at 16.4 MPa (2400 psi) by two four-stage compressors is stored in two storage tanks with 42.5 m³ (1500 ft³) capacity. The high Reynolds number wind tunnel used in these experiments has a 152.4 x 152.4 mm test section. The tunnel is set up in a dual-stream configuration in which two independent streams merge downstream of a splitter plate to form a constant pressure mixing layer as shown in Fig. 1. The air is fed into the tunnel by two separate control valves. Therefore, the flow to both streams can be independently controlled. The tunnel can be operated from a few minutes to several minutes depending on the nozzles used.

Optical access to the test section is provided through the combination of an interchangeable glass window and access panel on the side walls and glass windows on the top and bottom walls. Interchanging the window and access panel creates a viewing area approximately 80 mm high and 500 mm long. This area includes a 20 mm long view of the incoming boundary layer. The top and bottom viewing areas are 30 mm wide and 300 mm long. A more detailed description of the experimental setup has been given previously by Elliott [1989] and Glawe [1991].

In all the experiments reported here, one stream was always supersonic and the other was subsonic. When the incoming supersonic flow fully expands at the trailing edge of the splitter plate, the convective Mach numbers for the mixing layer (Cases 1 and 2) are 0.51 and 0.86, respectively. In order to obtain a mixing layer with a convective Mach number between those of Cases 1 and 2, the high speed stream was passed through expansion waves centered at the trailing edge of the splitter plate. The convective Mach number for this case (Case 3) was 0.64. While in Cases 1 and 2 the constant pressure mixing region was sustained throughout the test section, in Case 3 the constant pressure region was limited to about 235 mm from the splitter plate. The expansion waves generated at the trailing edge of the splitter plate for Case 3 reflected from the top wall and intersected the mixing layer around 235 mm from the splitter plate, thereby imposing a gradual pressure gradient on the mixing layer. The Mach numbers,

convective Mach numbers, theoretical convective velocities, free stream velocity and density ratios of the mixing layer for all three cases are given in Table I.

Table I Relevant Mean Flow Parameters

	Case 1	Case 2	Case 3
M_1	1.80	3.01	1.96
M_2	0.51	0.45	0.37
M_c	0.51	0.86	0.64
U_c/U_1 (Theor.)	0.76	0.73	0.68
U_2/U_1	0.36	0.25	0.25
ρ_2/ρ_1	0.64	0.37	0.58

For the supersonic stream in Cases 1 and 2, the incoming boundary layer thickness, momentum thickness, and the Reynolds number based on the momentum thickness are given in Table II. Needless to say, the supersonic boundary layer characteristics are the same for Cases 1 and 3.

TABLE II Incoming Flow Conditions

	Case 1	Case 2
M_1	1.83	3.0
M_2	0.51	0.45
δ_1 [mm]	8.0	9.2
Θ_1 [mm]	0.62	0.37
$Re_{\Theta1}$	27700	24700

In these experiments two schlieren systems were utilized. The purposes for using the schlieren systems were twofold. First, it was insured that the test section was free of any undesirable waves that could impose external disturbances on the mixing layer. Second, structures in the mixing layer were visualized. In the later experiments, filtered Rayleigh/Mie

scattering was used for the visualization of structures. One of the schlieren systems is a standard system with a 500 ns flash and a 35 mm camera, the other is a laser based system utilizing an intensified CCD camera to record images and store them on either a 486 personal computer or on a Panasonic super VHS video recorder with editing features.

The static pressure in the test section was measured by pressure taps in the top and bottom walls of the tunnel and also in a plexiglass window which can be mounted in the side wall instead of the glass windows for this purpose. For the matched pressure cases (Cases 1 and 2) in the entire viewing area, and for the underexpanded case (Case 3) in the region before the expansion waves generated at the trailing edge of the splitter plate reflect off the top wall and interact with the shear layer ($x < 235$ mm), the pressure variation was within 6% of the mean pressure.

Four sets of experiments, namely (1) laser Doppler velocimetry (LDV) experiments, (2) space-time correlation experiments, (3) particle-laden mixing layer experiments, and (4) filtered Rayleigh/Mie scattering based experiments have been conducted. All three convective Mach number cases were investigated in the LDV experiments. However, only Cases 1 and 2 were explored in the other experiments. The first three sets of experiments have been completed and the fourth set is currently underway. The fourth set is an extensive effort to not only visualize the mixing layer, but to also obtain simultaneous planar velocity and density data based on filtered Rayleigh/Mie scattering. Therefore, only preliminary data from this set will be presented in this report. The experimental techniques and instrumentation for these experiments will be discussed in this section and the results will be presented in the following section.

2.1 Laser Doppler Velocimetry Experiments

To evaluate the effects of compressibility on the mixing layer, a two-component coincident laser Doppler velocimetry (LDV) system was used to obtain detailed mean velocity and turbulence data. The LDV system was set at a 10-degree off-axis forward scatter mode in these experiments. The measurement volume diameter and length, to e^{-2} intensity level, were 0.13 mm and 0.90 mm, respectively. The two components were set at ± 45 degrees relative to the mean flow direction in order to decrease the Doppler frequency to a manageable level. Both flows were seeded in the settling chamber with atomized silicone oil less than 1 μm in diameter

[Samimy and Abu-Hijleh, 1989]. All the LDV results presented here are based on 2048 samples per channel. Although the number of samples taken is sufficient for the mean velocity results, a larger sample size would be desirable to reduce the scatter in the turbulence results arising from statistical uncertainty. The reader is referred to Elliott [1989] for more information on the LDV experiments.

2.2 Space-Time Correlation Experiments

In order to explore the effects of compressibility on the large scale structures of mixing layers, pressure space-time correlation measurements were obtained with fast response pressure transducers. Figure 2 gives a schematic of the pressure probe arrangement in the shear layer. The two probes were fitted with Endevco fast response differential pressure transducers, model 8514-20, with a sensitivity from 0 to 20 psi. The pressure sensitive diaphragm of these transducers is approximately 0.7 mm in diameter with an estimated frequency response of better than 50 kHz, which is more than sufficient to capture the signature of large scale structures in these experiments. The pressure transducers were mounted perpendicular to the incoming streams, extending about 10 mm out of the probe tip to approximately measure the static pressure fluctuations. The mean static pressure is approximately constant across the mixing layer; however, there is a significant stagnation pressure change across the mixing layers. Therefore, static pressure probes were used, instead of pitot-pressure probes as in the study by Shau and Dolling [1990], to increase the sensitivity of the pressure transducer. It should be emphasized that the intention was not to obtain highly accurate static pressure measurements, but to detect large scale structures. An Ectron model 563F signal conditioner was used with each transducer to provide the excitation voltage and to amplify the output signal. A MASSCOMP 5520 computer was used to acquire and process 100 blocks of data per measurement location with 1024 samples per block and a 250 kHz sampling rate.

2.3 Particle-Laden Mixing Layer Experiments

These experiments were designed and performed to explore the dispersion of solid particles and basic mixing phenomena in compressible free shear layers. Changing either one of the time scales (τ_p or τ_f) changes the time scale ratio (Stokes number, St) and ultimately the

14

particle dispersion; see Eqn. 5. In these experiments, the particle size alone was changed to vary τ_p and two different flow conditions were used to vary τ_f. These combinations comprised six different Stokes numbers.

To assure consistent drag force as calculated by Stokes drag law, the particles need to be spherical and uniform in both size and density. Spherical glass beads from Potters Industries, Inc. were the most economical material for our purposes. The particles purchased from this company were sorted (air classified) by the Vortec Products Company to obtain particle groups with nominal diameters of $5\mu m$, $17\mu m$, and $62\mu m$, all with a nominal diameter tolerance of ± 2 μm.

A two-phase flow of spherical particles suspended in air was pumped through two tubes, each passed through opposite tunnel sidewalls and into channels in an injection wedge, which was mounted on the subsonic side of the splitter plate. The wedge was made from a 1.27 x 152 x 152 mm aluminum plate. The thickness of the trailing and leading edges of the wedge was approximately 0.5 mm. This was obtained by machining the 1.27 mm thick plate with an approximately 10^0 slope toward the leading and trailing edges to minimize flow disturbances and modification of the incoming nozzle flow.

Since the particle injection wedge was located in the subsonic side, which is driven by the supersonic flow (similar to a supersonic-subsonic ejector system), the wedge's effect on the base flow was expected to be very small. Figures 3 and 4 are long-exposure ($\approx$ 1 ms) schlieren photographs of the flow field without and with the particle injection wedge mounted for Cases 1 and 2, respectively. Each photograph has two segments; one for the upstream and one for the downstream regions of the mixing layer. There is an overlap between the images for Case 1 and a gap for Case 2 due to physical restraints in the tunnel. The dark line on the photographs indicates the physical $y = 0$ location, which corresponds to the lateral position of the splitter plate. This line was drawn on the schlieren image plane. As expected, these images (and also short exposure, $0.5\mu s$, images not reported here) did not show any observable effect of the injection wedge on the flow fields. Also, since the shear layer is not deflected toward either freestream, the photographs confirm that the pressure in the test section was constant with and without the particle injection system. The particles were injected in the streamwise direction, through a series of holes on the rear-facing slope of the wedge at a station 14.6 cm

15

upstream of the trailing edge of the splitter plate. A MARK XII fine powder feeder was used to supply a reasonably constant, low mass flow of glass beads to the injection wedge. The powder feeder consists of a pressurized, sealed powder canister, a variable speed screw assembly, and a carburetor.

A Quanta-Ray GCR-4 Pulsed Nd:YAG laser manufactured by Spectra Physics was used in these experiments. The laser, operated without amplification (oscillator only), produced approximately 250 mJ/pulse of energy. The pulsed laser was operated at a wavelength of 532 nm, a pulse width of approximately 9 ns, and a repetition rate of 10 Hz. Mirrors and lenses were used to form a sheet of laser light in the test section approximately 14.5 mm wide and calculated to be a fraction of a millimeter thick. The laser sheet was oriented to illuminate the glass beads in a streamwise slice of the shear layer, parallel to the wind tunnel's side walls. Figure 5 illustrates the laser sheet lighting and image recording system.

A double-intensified gated CCD camera, focused on the vertical sheet of laser light passed through the wind tunnel, recorded instantaneous images onto super VHS tape. The images on the tape were later transferred to a computer using a frame grabber. The resulting raw data was the intensity (on a scale of 0-255) of each pixel in a 480x512 grid configuration which was stored on a MASSCOMP 5520 computer and subsequently used for image processing.

2.3.1 Digital Image Processing: Flow visualization and subsequent analysis of digitized images were used to locate the particles' positions for statistical analysis. Approximately one-hundred and fifty images were selected and digitized from each of the six flow conditions. The image selection criteria were (1) the image contained enough particles to contribute to the statistical calculations (minimum of about twenty particles) and (2) the image was not dominated by clumping and visually overlapping particles, characteristic of a surge in the particle injection system. The criterion (2) was used to minimize the effect of particles (due to sporadic high particle loading) on the flow field.

The laser beam was expanded into a sheet and brought into the tunnel from the top window; see Fig. 5. The Gaussian nature of the laser sheet light caused a nonuniform distribution of illuminating intensity in the x-direction of the image. Note that in the coordinate system of the images, the flow is in the x-direction. The average intensity values of the center

column pixels were larger than the average intensity values of the edge column pixels. This prohibited the use of a global threshold intensity value to distinguish between particle and background intensities in the original images. This problem was circumvented by computing local thresholds that vary along the direction of the non-uniformity. The program identified particle images by examining group patterns of adjacent pixels brighter than their corresponding threshold intensities. The size and intensity of the bright pixel groups representing the particles depend jointly on particle light scattering characteristics, particle motion, illuminating properties, and recording device properties. Mean and standard deviation values for particle image size and particle image average intensity were used to identify and eliminate data generated by means other than a single particle passing through the laser sheet. The total number of particles included in the calculations for figures showing the average particle dispersion (which will be shown and discussed later) ranged from 3537 to 8653 particles depending on the case.

After verifying that the particle images were the result of light scattered from one of the glass beads passing through the laser sheet, the data were scaled and rotated to align the images with physical reference points placed on the far sidewall of the test section. This enabled direct physical comparison between all the test runs. The physical reference points were produced by passing light through a series of pinholes in the black masking on the far wall of the wind tunnel. Readers are referred to Glawe [1991] for details on the image processing.

2.4 Filtered Rayleigh/Mie Scattering Based Experiments

In order to obtain planar images of structures, rather than spanwise averaged images obtained using schlieren, a filtered Rayleigh/Mie scattering technique was utilized. The resulting images shown in this report represent the first step of an effort currently underway to obtain simultaneous planar density and velocity measurements.

The light source used in these experiments was a Quanta Ray GCR-4 frequency-doubled (532 nm) Nd:YAG laser which was injection seeded to provide a narrow line width and approximately 50 GHz tuning capability. The Nd:YAG laser used in these experiments is the same one used in the particle dispersion experiments and has a pulse width of 9 ns. This exposure time is sufficiently short to effectively freeze the flow field. A combination of prisms,

spherical lenses, and cylindrical lenses were used to construct a sheet of light with a fraction of a millimeter thickness in the test section.

Two different recording systems were used to capture and store the images. The first is an ITT 8-bit double intensified CCD camera with an RS-170 video output, and is the same system used in the particle dispersion experiments. The images were stored on a Panasonic super VHS recorder. The other system is a Princeton Instruments intensified CCD camera with 14-bit output stored on a 486 personal computer. Cooling provided to this camera decreases the background signal, enabling it to have a sensitivity on the order of a single photoelectron. In the following section, a brief description of the filtered Rayleigh/Mie scattering technique will be given.

2.4.1 Filtered Rayleigh/Mie Scattering: Visualizations of supersonic flows have traditionally been made using schlieren or shadowgraph techniques. Unfortunately, these techniques make it difficult to evaluate details of the flow field due to their inherent spanwise averaging effects. Laser sheet lighting techniques, however, make it possible to view scattering in a thin plane. The collected signal can be from the fluorescence of molecules naturally present in the flow or artificially seeded [e.g. Hanson et al., 1990]. In scattering techniques, Mie scattering[e.g., Samimy et al. 1991b, Clemens and Mungal, 1991, Messersmith et al., 1991, Komine et al., 1991], or Rayleigh scattering[e.g. Miles et al., 1991, Smith et al., 1991] from small particles or molecules within the flow field is collected. One problem often encountered in scattering techniques is the presence of background noise from the light scattered off of walls or windows. This situation is especially evident in Rayleigh scattering techniques because of the low level of the scattered intensity. One way to eliminate this background noise is through the use of a molecular absorption filter placed in front of the collecting optics.

One of the first uses of the molecular filter was by Shimizu et al.[1983] who used them as blocking filters in atmospheric measurements of temperature and pressure. Miles et al.[1991] extended the use of molecular filters to flow visualizations, a technique that they call filtered Rayleigh scattering [FRS]. There are basically two sources of scattering. Figure 6a gives a schematic of the scattering from the particles in the flowfield, which experience a Doppler shift whose magnitude depends on the angle of the collection optics, incident beam from the laser, and the velocity vector orientation and magnitude. Also, there is unwanted scattering from the

18

windows and walls of the wind tunnel which experiences no Doppler shift. By using an injection seeded frequency-doubled Nd:YAG laser, the line width is narrow enough and the frequency can be tuned on the injection seeder so that the hyperfine absorption bands of iodine absorb the unshifted background light while allowing the Doppler shifted light to pass through. This situation is illustrated in Fig. 6b. The molecular filter for this technique is made by placing a small amount of iodine crystals in an optical cell and evacuating the cell so that the iodine vaporizes. The absorption profile of the filter can be controlled by the length, concentration, temperature, and pressure of the iodine cell. For background suppression, an optically thick filter with a sharp cut off is used. Miles et al.[1991] used this type of filter to not only cut out background light, but to also demonstrate that the average velocity in a supersonic flow can be measured.

Komine et al.[1991] used a similar molecular filter operating in the optically thin regime (which has more gradual, rather than sharp, cutoff slopes) to obtain velocity measurements from a seeded jet using a multiple camera system. The role of the filter was not to suppress the background noise (since the scattering from the seeded particles was in the Mie scattering regime which is much stronger), but rather to attenuate the collected intensity as a function of frequency, so that the amount of Doppler shift present in the signal could be obtained. This allowed planar velocity maps to be calculated.

The filter used in the present visualizations is similar to the optically thick filter used in the FRS technique by Miles et al.[1991]. The filter is a glass cylinder 3.5 inches in diameter and 10 inches long, operated at a pressure and temperature of .18 torr and 298 K, respectively. These conditions were used to reduce, if not eliminate, the background scattering from the walls and windows. Currently, we are investigating a possible method of measuring instantaneous velocity using an absorption filter which has the background suppression characteristics of an optically thick filter, but with a sloping profile caused by changing the temperature, pressure, length and composition of the gas used in the filter [Elliott et al., 1992].

3.0 RESULTS AND DISCUSSIONS

In this section we will present and discuss the results obtained in our laboratory and compare them with the results of other investigators when appropriate. We will first present the LDV results, which include the mean velocity and turbulence results for the incoming boundary layers and the mixing layers, followed by the results on the large scale structures obtained using both filtered Rayleigh/Mie scattering based visualizations and two-point correlation measurements. We will finally present results on the particle dispersion in compressible mixing layers.

3.1 Laser Doppler Velocimetry Based Results

As discussed in Section 2, a two-component coincident laser Doppler velocimetry operated in a forward-scatter 10° off-axis configuration was utilized to obtain detailed mean flow and turbulence data in mixing layers with convective Mach numbers of 0.51 (Case 1), 0.64 (Case 3), and 0.86 (Case 2). Details of the LDV system and concerns about the seed particles and velocity bias are given by Samimy and Elliott [1990] and Elliott and Samimy [1990]. The pertinent parameters for the three cases are given in Tables I & II in Section 2. Next, the incoming boundary layers results will be presented.

3.1.1 Incoming Boundary Layers:
In all three convective Mach number cases, the top stream was supersonic and the bottom stream was subsonic (see Fig. 1); very similar to a supersonic-subsonic ejector where the supersonic stream is the driver stream and the subsonic stream is the driven stream. In such a mixing layer, one would expect the incoming boundary layer characteristics of the driven flow to play an insignificant role on the mixing process. Therefore, only the characteristics of the incoming boundary layers of the driver streams were documented. As was discussed earlier, Cases 1 and 3 had exactly the same incoming boundary layer in the supersonic side. While the boundary layer in Cases 1 and 2 passed through either a very weak expansion or compression wave at the trailing edge of the splitter plate, the boundary layer in Case 3 passed through a much stronger centered expansion wave.

Figure 7 shows the mean velocity (U/U_1), streamwise turbulence intensity (σ_u/U_1), and correlation coefficient ($R_{uv} = -\overline{u\,v}/\sigma_u\sigma_v$) for the boundary layers in Cases 1 and 2. A

relatively small compressibility effect on the streamwise turbulence level, but a large effect on the correlation coefficient, especially toward the upper edge of the boundary layer, agree well with the results compiled by Smits et al. [1988].

3.1.2 Mean Velocity Profiles: Originally, Schlichting [1964] extended Gortler's single-stream analysis to a planar two-stream incompressible mixing layer and obtained the following solution for the mean velocity profile in the fully developed region

$$U^* = \frac{U - U_2}{U_1 - U_2} = \frac{1}{2}[1 + erf(\sigma \frac{y - y_{0.5}}{x - x_0})] \qquad (9)$$

In this equation, the argument of the error function, $\eta = [\sigma(y-y_{0.5})/(x-x_0)]$, is called the similarity parameter. The similarity parameter contains three unknown parameters that must be determined experimentally. They are the spread rate parameter (σ), the location of the virtual origin (x_0), and $y_{0.5}$ which is the lateral location where $U = (U_1+U_2)/2$.

In the fully developed region where the mixing layer grows linearly, $b = (x-x_0)/\sigma$ is a measure of the thickness of the mixing layer. Samimy and Elliott [1990] showed that the normalized mean velocity $[U^* = (U-U_2)/(U_1-U_2)]$ profiles, in mixing layers with a wide range of compressibility levels, collapse onto a single curve when b is taken to be the mixing layer vorticity thickness defined as:

$$\delta_w = \frac{U_1 - U_2}{[\partial U/\partial y]_{max}} \qquad (10)$$

Figure 8 shows the mean velocity profiles from various experiments together with a curve given by:

$$U^* = \frac{1}{2}[1 + \tanh(2.4y^*)] \qquad (11)$$

where $y^* = (y-y_{0.5})/\delta_w$. The collapse of the data onto a single curve indicates that the vorticity thickness and the velocity difference across the mixing layer (U_1-U_2) are good

measures of the lateral length scale and velocity scale in mixing layers, whether compressible or incompressible. More information on the mean velocity profiles is given by Elliott [1989] and Samimy and Elliott [1990].

3.1.3 Mixing Layer Growth Rate: Various thickness measures have been used in the literature to determine the growth rate of compressible mixing layers. To isolate the compressibility effect, the growth rate is normalized by the growth rate of an incompressible mixing layer to remove the effects due to the velocity and density gradients across the mixing layers. Some of the thickness measures are a visual thickness from a schlieren photograph, a percentage velocity change (e.g. the thickness between $0.1U^*$ to $0.9U^*$), the momentum thickness, and the vorticity thickness. From the discussion in Section 3.1.2, it is apparent that the vorticity thickness is the best choice. However, the mean velocity profile is required to determine the vorticity thickness, which is not always available.

Figure 9, taken from Bogdannof [1983], shows the normalized vorticity thickness growth rate for a wide range of convective Mach numbers. The vorticity growth rate for incompressible mixing layers used to normalize the compressible growth rates in Fig. 9 is taken from Brown and Roshko [1974]; $(d\delta_w/dx)_i = 0.181(U_1-U_2)/(U_1+U_2)$. While the mixing layer in Case 1 exhibits only a small compressibility effect, Case 2 displays an approximately 50% reduction in the growth rate. A similar trend has been reported by many other investigators.

3.1.4 Turbulence Results: Using a simultaneous two-component LDV system, detailed turbulence data were obtained in both the developing and the fully developed regions of all three convective Mach number cases. Only some results in the fully developed region will be reported here. The results show a reasonable collapse of data in this region. For detailed results, the reader is referred to Elliott [1989], Samimy and Elliott [1990], and Elliott and Samimy [1990].

Figures 10-13 show the streamwise ($\sigma_u/\Delta U$) and lateral turbulence intensities ($\sigma_v/\Delta U$), anisotropy ratio (σ_u/σ_v), and the Reynolds shear stress ($\overline{u\,v}/\Delta U^2$) for all three cases; $\Delta U = U_1 - U_2$. These figures also include results for the incompressible mixing layer studied by Oster and Wygnanski [1982] for comparison. The strong effect of compressibility on all three components of the Reynolds stress is evident. However, there does not seem to be any

observable effect of compressibility on the anisotropy ratio, indicating a similar effect of compressibility on both normal components of the Reynolds stress. Similar results have also been reported by Barre et al. [1992] and Bonnet et al. [1992]. Goebel and Dutton [1991] have shown similar compressibility effects on the lateral turbulence intensity and the Reynolds shear stress, but a relatively minor effect on the streamwise turbulence intensity.

Figure 14 shows the correlation coefficient defined as $R_{uv} = -\overline{u\,v}/\sigma_u\sigma_v$ which is also called the turbulence structure parameter. While the major contributors to $\overline{u\,v}$ are large scale structures, both large and small scale structures contribute to $\sigma_u\sigma_v$. The compressibility seems to affect the structure parameter mostly in the intermittent region of the high speed side. In this region of a mixing layer, the large scale structures extend into the free stream, engulf fresh fluid and entrain it into the mixing region. Therefore, the results of Fig. 14 imply that compressibility affects the large scale structures and limits their entrainment ability. In comparing the results presented in Figs. 7 and 14, one notices that the compressibility influences the turbulence structure parameter in a similar fashion in both the free and bounded shear layers.

The effects of compressibility on large scale structures are even more clearly demonstrated by looking at higher moments of turbulence fluctuations. Figure 15 shows the flatness parameter for the streamwise velocity fluctuations, $\overline{u^4}/\sigma_u^4$. The flatness indicates whether there are high probabilities of fluctuations occurring far from the mean in the probability density function (PDF) of the velocity fluctuations. The flatness value for a normal distribution is 3. There are two points to notice in Fig. 15. First, the maximum value of the flatness at the high speed side is much lower for Case 2. Second, if the maximum flatness in both sides of the mixing layer marks the edges of the mixing layer, then the extent of the turbulent mixing region has been drastically reduced in the highest compressibility case. These findings basically complement and support the conclusions drawn from Fig. 14 on the effects of compressibility on the structures. Also, these results give some clue as to how the compressibility reduces the growth rate of mixing layers.

One of the concerns associated with using LDV in high speed flows is whether the LDV seed particles follow the high frequency fluctuations encountered in these flows. The seed particles used in these experiments were atomized silicone oil particles of approximately

1 μm diameter. The computational results of Samimy and Lele [1991] indicate that these particles would definitely follow the large scale structures.

The main contributions to Reynolds shear stress comes from the large scale energy containing eddies. Fernandez and Zukoski [1969] showed that the Reynolds shear stress can be obtained from the mean velocity using the following equation:

$$\frac{\tau[y]}{\rho_1(U_1 - U_2)} = \frac{d\theta}{dx}\left(U^* - U^*\int_0^{\bar{y}} \frac{\rho}{\rho_1} U^* d\bar{y} + \int_0^{\bar{y}} \frac{\rho}{\rho_1} U^{*2} d\bar{y}\right) \quad (12)$$

where $\bar{y}$ is y/θ, and θ is the local momentum thickness. In equation 12, ρ is the average density which can be calculated using the local mean velocity, stagnation temperature, and static pressure. The shear stress results determined using Eqn. 12 are shown in Fig. 16. Details of this calculation are given by Elliott and Samimy [1990]. Comparing these results with those in Fig. 13, one observes a similar compressibility effect on the directly measured and the indirectly determined Reynolds shear stress. In order to have a more direct comparison, the results presented in Fig. 13 are replotted in Fig. 17 to include the density change across the shear layer. In Fig. 17, one observes good agreement not only in terms of trend, but also in terms of magnitude. This definitely lends credibility to turbulence measurements using LDV in the current experiments.

The Reynolds shear stress in compressible flows has two other terms besides the one shown in Figs. 13 or 17. The other two terms represent density-velocity fluctuation correlations. Following Morkovin's hypothesis that the effects of density fluctuations on turbulence are negligible if the root-mean-square density fluctuation is small relative to the mean density, these two terms have been generally ignored [Bradshaw 1977]. Bradshaw suggests a Mach number of 5 as the upper limit of Morkovin's hypothesis for boundary layer and wake flows. The good comparison of the results in Figs. 16 and 17 seems to show that Morkovin's hypothesis is also valid in mixing layers of moderate compressibility level.

24

3.2 Results on Large Scale Structures

Initial flow visualizations using schlieren photography indicated the existence of large scale structures even in the highly compressible mixing layer of Case 2 [Elliott and Samimy 1990]. Therefore, an effort was initiated to obtain detailed qualitative and quantitative data on these structures. Pressure correlation measurements were used to obtain quantitative data and filtered Rayleigh/Mie scattering based visualizations were used to obtain qualitative data on large scale structures.

3.2.1 Pressure Correlation Results: Only sample results from static pressure based two-point correlation measurements will be reported here. The details of these results have been reported by Reeder [1991] and Samimy et al.[1992]. Figure 18 shows the streamwise coherence for Cases 1 and 2 at a single lateral location in the fully developed region. When $\Delta x/\delta_w \approx 0.5$ (Δx = streamwise probe separation, denoted by dx in the figures), the coherence levels are comparable for the two cases. The coherence level drops by about 50% after increasing probe-separation to $\Delta x/\delta_w = 4.7$ and 1, for Cases 1 and 2, respectively. This indicates a tremendous compressibility effect on the streamwise evolution of large scale structures in Case 2 ($M_c = 0.86$). Note that the local Reynolds numbers are comparable for the two cases. Results obtained in the developing region and at other lateral locations show a similar compressibility effect [Reeder 1991]. The streamwise space-time correlations shown in Fig. 19 exhibit a similar compressibility effect. In the pressure results reported here, the lateral nondimensional coordinate is defined as $y^* = (y-y_{ref})/\delta_w$ where y is the lateral location measured from the top surface of the splitter plate, y_{ref} is the lateral distance from the splitter plate where the measured convective velocity using spatial correlation matches the theoretical value, and δ_w is the local vorticity thickness. In the LDV results, y_{ref} is replaced by $y_{0.5}$ in defining y^*, where $y_{0.5}$ is the location of $(U_1+U_2)/2$.

The streamwise spatial correlations shown in Fig. 19 can be used directly to calculate the average convective velocity over many structures at specific probe locations, and thus the convective Mach number. Instead we have used the pressure signals from the two probes to calculate the convective velocity of individual structures [Reeder 1991]. This gives information concerning the variance of the convective velocity at a given location. Figures 20 and 21 show histograms of convective velocity for Cases 1 and 2 at two lateral locations.

Based on these results and others not reported here [see Reeder 1991], the following observations can be made: 1) even at $y^* \approx 0$ where the average U_c is equal to the theoretical U_c, structures have a wide range of convective velocities, 2) both the average and distribution change with y^*, and 3) the variation with y^* becomes larger as the compressibility is increased. The lateral variation of average U_c has been reported before in both incompressible [Jones et al. 1973] and compressible mixing layers [Ikawa and Kubota 1975]. In light of these results and flow visualization results to be reported in Section 3.2.2, which show the large scale structures of Case 2 tend to be highly three-dimensional, three things need to be kept in mind: 1) while M_c is a good indicator of overall compressibility level, one should not overemphasize it, 2) any U_c measurements depend a great deal on the lateral position where they are taken, and 3) any U_c, and thus M_c measurements based on a limited number of structures could potentially produce highly erroneous results.

Single-point pressure fluctuations and two-point pressure correlation measurements in the spanwise direction were obtained to assess the three-dimensionality and obliqueness of large scale structures. The rms pressure fluctuations in the developing region did not show any observable variations in the spanwise direction in either Case 1 or 2 [Samimy et al. 1992]. Some spanwise variations with no clear pattern were developed downstream in Case 1. However, spanwise variations up to 3 fold with a relatively distinct pattern can be seen in the fully developed region of Case 2 (Fig. 22). The tunnel span is from 0 to ± 76 mm, but the measurements are taken only in the midsection of the tunnel far from the side walls. The results in Fig. 22 indicate that some sort of structures are developed in Case 2 which seem to have relatively good spatial organization as they convect downstream. The maximum rms pressure-producing region of the structures in this case seems to start from the spanwise center of the low speed side and branch out in the spanwise direction as the legs extend upward in the lateral direction.

As was discussed earlier, the stability analyses of Ragab and Wu [1989] and Sandham and Reynolds [1991] show that oblique instability waves are more amplified than two-dimensional waves in highly compressible mixing layers. In fact, the direct numerical simulations of Sandham and Reynolds with two initial oblique instability waves of opposite signs produced a pressure field which appears similar to the experimental results described

in the above paragraph. However, their results showed two horseshoe-type vortices; one with the head at the high speed side and the other similar to the one described above. With only three lateral locations examined herein, it would be premature to definitively describe details of the structures' topology and orientation.

Spanwise correlations normalized by the rms fluctuations are shown in Fig. 23 for Case 1 ($M_c = 0.51$) at $y^* = -0.21$ in the fully developed region of the mixing layer. The correlation level dropped from 0.27 to 0.08 when $\Delta z/\delta_w$ was changed from 0.25 to 1.2. The maximum correlations occurred at zero time delay, indicating the two-dimensional, spanwise-aligned nature of the structures. This behavior is similar to incompressible mixing layer results [Browand and Troutt 1980]. Figure 24 shows the spanwise correlation for Case 2 in the fully developed region at two y^* locations. The general trend of these correlations indicates the complex nature of the structures. When one probe is at $z = 0$, $y^* = -0.6$, and $\Delta z/\delta_w = 0.17$, the peak correlation level is relatively high and positive with a small time shift. However, the correlation peak changes sign and the level drops significantly with a relatively large time shift for $\Delta z/\delta_w \geq 0.25$. At the $y^* = -0.15$ location with a small $\Delta z/\delta_w$ both positive and negative correlations are present; but when $\Delta z/\delta_w$ is increased, the correlations are negative and the level of correlations first increases then drops. The spanwise angle of these structures can be calculated using $\beta = \tan^{-1}(U_c^* \tau/\Delta z)$, where U_c is the theoretical convective velocity and τ is the time delay corresponding to maximum correlation. There is a large variation in the calculated angle (from -74° to +69°) of these structures [Reeder, 1991 and Samimy et al., 1992].

The conceptual picture of the structures arising from the pressure results presented for Case 2 is a complex one. Pressure correlations indicate that the most dominant structures are highly three-dimensional, inclined both in the x-y and in the x-z planes, and that they have a relatively good spatial organization (tend to occur at the same "preferred" spanwise location as evidenced by the spanwise rms pressure distributions). One element of the structure may be a horseshoe-type vortex with the head in the low speed side and the legs, inclined both in the x-y and the x-z planes, extending toward the high speed side. This is similar to one of the structures observed by Sandham and Reynolds [1991] in their simulation of highly compressible mixing layers with initial oblique disturbances. Since only the midsection of the tunnel

was probed, it is possible to imagine that a large structure is composed of two or more horseshoe-type structures connected at the low speed and/or high speed edge(s) of the mixing layer.

3.2.2 Filtered Rayleigh/Mie Scattering Based Visualizations:

In the flow visualization results presented here, it should be kept in mind that hundreds of images have been taken for each case and only a few are presented here. Most of the visualization images for the higher convective Mach number are from the passive scalar technique, and all of the lower convective Mach number images are from the product formation technique. The flow direction in all streamwise-transverse (X-Y) and plan view (X-Z) images is from right to left. As mentioned earlier, the pulse width of the laser is 9 ns, effectively freezing the flow for each image. However, the time lapse between two consecutive images is 0.1 s making them totally uncorrelated.

Figure 25 shows streamwise-transverse (X-Y) views of the developing and fully developed regions for Case 1 at four unrelated instances. Many images in both the developing and the fully developed regions for this Case (e.g. Fig. 25a & c) show the flow is dominated by large scale structures with distinct braid and core regions similar to those observed originally by Brown and Roshko [1974] in incompressible mixing layers. Of course, some other images show large scale structures which are not as well defined (e.g. Fig. 25b & d). Clemens and Mungal [1992] have reported similar structures in compressible layers with low compressibility levels.

Plan (X-Z) views of the Case 1 mixing layer are shown in Fig. 26. Figures 26a and 26b show plan view images in the middle and at the upper edge of the developing region, respectively, and 25c is a plan view at the upper edge of the fully developed region. Streamwise streaks seems to emanate from the splitter plate and remain quite distinct for about 30 mm downstream (Fig. 26a). These streaks resemble the streamwise vortices observed in incompressible shear layers which are attributed to the amplification of upstream disturbances [Bernal and Roshko 1986]. Although little two-dimensionality is observed in the plan views in the middle of the developing region, it is more evident in the plan views located toward the upper edge of the mixing layer, in both the developing and the developed regions.

Figure 27 presents spanwise views from the developing and fully developed regions

of the Case 1 mixing layer for different streamwise locations. The streamwise streaks in the plan views appear as dots initially that grow larger and perhaps merge as they convect downstream. Figure 27c shows a spanwise view cutting through a braid, and Fig. 27d shows a spanwise cut through a core of a spanwise structure. The streamwise vortices discussed above in reference to Figs. 26 and 27 are the most probable cause of the significant undulations in the braid region shown in Fig. 27c.

Figure 28 presents streamwise-transverse (X-Y) views for the $M_c = 0.86$ mixing layer (Case 2). In the developing region (Fig. 28a), the mixing region marked by the product formation is separated from the region marked by the passive scalar signal in the top free stream. This is an effect of the higher temperature in the boundary layer of the high speed stream formed on the splitter plate. The mixing region in this case has no indication of structures with well defined core and braid regions observed in Case 1. Figures 28b and 28c present the streamwise-transverse images using only the passive scalar technique in the fully developed region for Case 2. Large structures and the associated intermittency at the edge of the mixing region are clearly present, although no indications of the high degree of structural organization seen in Case 1 were found.

Figure 29 shows plan (X-Z) views for the developing and fully developed regions for Case 2. In the middle of the mixing layer in the developing region (Fig. 29a), there is no sign of organized structures, but one thing that is observable is the delay of product formation until about 25 mm downstream. This is most probably due to the lack of mixing of cold supersonic and moist subsonic streams at this higher compressibility level. In all the images for this location, there was no indication of the streamwise streaks shown in the Case 1, suggesting that the streaks could perhaps be an important mechanism in the reduced growth rate with increasing compressibility level. Figures 29b and 29c display two passive scalar plan views for the fully developed region of case 2. Two types of relatively distinct spanwise oblique structures can be seen. One type of oblique structure is seen to branch from a streamwise core (Fig. 28b). In another type of structure, such as that shown in Fig. 29c, an entire large scale structure appears with oblique orientation in the shear layer. The portrait of large scale structures emerging from these visualizations seems to be in accord with that of our pressure results (Figs. 22 & 24) and that reported by Sandham and Reynolds [1991].

3.3 Particle Dispersion Results:

Long-exposure schlieren images of the $M_c = 0.51$ and $M_c = 0.86$ free shear layers show (Figs. 3 and 4) that matching the static pressures of the top and bottom streams maintains a straight shear layer with respect to the splitter plate and the top and bottom walls bounding the flow. Also, the results in Sections 3.1 and 3.2 indicate that the structures in the $M_c = 0.51$ case are similar to incompressible mixing layers in that they are relatively well organized, two-dimensional to a large degree, and possess relatively well defined core and braid regions. However, in the $M_c = 0.86$ free shear layer the structures are much less organized and more three-dimensional, and the mixing layer is characterized by substantially reduced growth rate and turbulent momentum exchange relative to the $M_c = 0.51$ case.

Long exposure time photograph-like composite images of particle-laden mixing layers were generated by superimposing many digital images in order to explore the general trends in the dispersion of particles in compressible mixing layers. Figures 30 to 35 each show the superposition of particle locations from over three hundred images. Two adjacent viewing areas were necessary to cover the total 25 cm streamwise segment of the mixing layer shown in the figures. Approximately one-hundred and fifty images were used from each the upstream (x = -1.0 to +15.0 cm) and the downstream (x = 10.0 to 26.0 cm) viewing areas for these superimposed images. The final plots therefore include an overlapping area in the range from approximately x = 10.0 to 15.0 cm. The origin of these plots (x,y=0,0) represents the trailing edge of the splitter plate. The dark solid line on the schlieren images (Figs. 3 and 4) indicates the physical x-coordinate location. The solid circles used to mark the particle locations on the figures are the same size for all cases, and thus do not reflect the true particle size or the recorded particle image size. It should be mentioned that the mass loadings of particles (the ratio of particle mass flow to carrier gas mass flow) were very small. As was mentioned earlier, each image was examined and any image with clustered particles was eliminated to maintain the very low particle loading data. Previous researchers have concluded that with a such small particle loading, the effect of particles on the base flow is essentially negligible [e.g. Crowe et al. 1988].

Figures 30 to 32 represent the flow field in Case 1, $M_c = 0.51$, with three different particle groups; groups a, b, and c. These three cases therefore will be called Cases 1a, 1b,

and 1c, respectively. Table III lists the particle diameter range and the dimensional Stokes number (St) for these cases. In this table, St_δ [$St_\delta = (St) \times (\delta)$ where δ is the flow length scale] is listed rather than St. The flow length scale is changing substantially in the streamwise direction. If one takes the flow length scale to be the mixing layer thickness, the length scale changes from a very small value at $x = 0$ cm to approximately 2 cm at $x = 22$ cm. Thus, for Case 1a the Stokes number changes from a very large value close to the splitter plate to approximately 3.5 further downstream in the mixing layer.

Since the flow length scale is the same for Cases 1a, 1b, and 1c ($M_c = 0.51$), the differences in the results for these three cases can be directly attributed to Stokes number differences. If the flow length scale is taken to be 1 cm, which corresponds to the mixing layer thickness at approximately $x = 10$ cm, the Stokes number changes from 7 for Case 1a (Fig. 30) to 1116 for Case 1c (Fig. 32). It should be mentioned that the wider size distribution (larger standard deviation of the particle diameters) of particle group a relative to groups b and c may slightly mask the results. Many particles in Case 1a and some in Case 1b are thrown deep into the supersonic free stream. The likely mechanism for this observation is that these particles were entrained into large scale structures and subsequently thrown out of the mixing layer due to centrifugal forces. As mentioned previously, several studies have highlighted this type of selective dispersion on the basis of Stokes number. These studies seem to suggest that particles will be ejected from the mixing layer for a mid-range Stokes numbers. The dispersion for Case 1a shown in Fig. 30 (for which the representative Stokes number is calculated to be 7) seems to represent this mid-range Stokes number based on the theoretical predictions. Furthermore, Cases 1a, 1b and 1c in Figs. 30 through 32 seem to follow the expected trend from Stokes number arguments [e.g. Chein and Chung 1988, Crowe et al. 1988, Lazaro and Lasheras 1989, and Samimy and Lele 1991]. Namely, the particles characterized by higher Stokes numbers spread less into the high speed side of the shear layer.

Instead of being totally unaffected by fluid motion, the particles of largest Stokes number appear to be affected to some extent by the skewed divergence of the shear layer. It is well documented that as one moves downstream in a mixing layer composed of one supersonic and one subsonic stream, lines of constant velocity diverge farther from the center

Table III   Dimensional Stokes Number

particle material: solid glass				
particle material density: 2.5 g/cm^3				
Dimensional Stokes number for M_c=0.51				
	Size	dp(μm)	τ_p(s)	St$_\delta$(cm)
Case 1a	min	1	0.0001	.3
	avg	5	0.0002	7
	max	7	0.0006	19
Case 1b	min	15	0.0021	65
	avg	17	0.0027	84
	max	20	0.0037	116
Case 1c	min	60	0.0332	1045
	avg	62	0.0354	1116
	max	65	0.0389	1226
Dimensional Stokes number for M_c=0.86				
	size	d_p(μm)	τ_p(s)	St$_\delta$(cm)
Case 2a	min	1	0.0001	.5
	avg	5	0.0003	12
	max	7	0.0007	30
Case 2b	min	15	0.0024	106
	avg	17	0.0031	136
	max	20	0.0042	189
Case 2c	min	60	0.0380	1700
	avg	62	0.0406	1815
	max	65	0.0446	1995

of the mixing layer in the subsonic side than in the supersonic side [Ikawa 1973 and Petrie 1984]. For example, Ikawa showed the lower-most constant lines of the mixing layer to be at a diverging angle approximately four times the upper-most ones. The schlieren photographs shown in Figs. 3 and 4 do not indicate this phenomenon due to the weak density gradient in the subsonic side. This misleading schlieren phenomenon can be seen in Figs. 3 and 4 where the incoming boundary layer for the high speed side is clearly shown but the boundary layer on the subsonic side is not visible. It appears that the downstream evolution of the average particle location is representative of this diverging shear layer structure at high Stokes numbers (Cases 1b and 1c).

Figures 33 to 35 show the superimposed images for Cases 2a, 2b, and 2c. The flow in these cases is $M_c = 0.86$ and the particles for cases a, b, and c are from the same groups as in Figs. 30 to 32, respectively. Neglecting the very few particles that were ejected into the supersonic free stream in Case 2a, one does not see any observable Stokes number effects in these figures as far as the penetration of particles into the supersonic stream is concerned. The striking feature of these results is that the mixing region marked by these particles has been substantially skewed (or bent) toward the low-speed side of the mixing region. As previously discussed, this is a constant pressure mixing layer and schlieren photographs shown in Fig. 4 clearly show that the mixing layer is straight.

A possible explanation for the apparent particle dispersion independence of Stokes number in Cases 2a, 2b, and 2c can be formulated if one considers more closely the flow time scale. The results in Sections 3.2 indicate that the large-scale flow structures in the mixing layer of Case 2 ($M_c = 0.86$) are much less organized than in Case 1 ($M_c = 0.51$) and appear to be more three-dimensional and oblique in the spanwise direction. Consequently, the flow length scale becomes significantly smaller in Case 2 causing the Stokes number to increase, possibly resulting in Case 2a (and subsequently 2b and 2c) belonging to the broad category of particles having Stokes numbers sufficiently high that their dispersion is not affected by fluctuations in the fluid motion. Samimy and Lele's [1991] for M_c values up to 0.6 did not show any compressibility effects. However, their

recent results (work in progress) show a significant compressibility effect for the Mc=0.86 case.

This trend, where the trajectory of particles are reminiscent of the skewed divergence of the shear layer, is similar to that seen in Case 1c. One might think that the trend seen in Figs. 32 to 35 is caused by the force of gravity. However, calculations show that the downward trajectory of the particles cannot solely be an effect of gravity [Glawe 1991].

Figure 36 shows the average particle location for all the six cases shown in Figs. 30 through 35. The Stokes number dependence in Cases 1a, 1b, and 1c is quite clear. From this figure it is also clear that the same vertical particle location at the tip of the splitter plate (x=0 cm) is not achieved for all of the cases. Ideally, the particles achieve the subsonic free stream velocity by the time they reach the tip of the splitter plate and are introduced into the mixing layer at the same location. However, achieved experimental conditions are far from ideal. The particle velocity is unknown and the average particle y-location at the splitter plate tip (x=0 cm) decreases as the particle size increases, especially for Case 2. Based on a simple calculation, this is not entirely an effect of gravity [Glawe 1991]. The calculated vertical displacement due to gravity by the time the particle reaches the end of the splitter plate (x=0 cm) is only y= -0.196 cm for the largest particles. The most probable cause of this displacement is the interaction of the particles with the boundary layer on the bottom side of the splitter plate.

The fact that the vertical particle elevation at the tip of the splitter plate decreases with increasing particle size may be a cause for reduced dispersion. However, recent spatially evolving numerical simulations by Samimy and Lele (work in progress) seem to indicate that regardless of the initial particle release location, the particles with the same Stokes number get entrained into the mixing layer and eventually follow similar paths. This phenomenon is particularly evident in Case 2 since 2a, 2b and 2c where all cases have high Stokes numbers (far into category 3). Figure 36 shows the average particle location for Cases 2a, 2b, and 2c to be initially different. However, this difference vanishes further downstream as the particles average location for the three

cases converges for $x > 15$ cm. Cases 1a, 1b, and 1c do not show this phenomenon since their smaller Stokes numbers fall in different categories; thus making them behave differently.

In these experiments we do not have any particles with a small enough Stokes number to accurately follow the flow (category 1). Case 1a seems to fall into the category of particles with medium Stokes numbers which are significantly affected by large scale structures (category 2). Cases 1c, 2a, 2b, and 2c seem to fall into the category of particles with large Stokes numbers which are not significantly affected by large scale structures and disperse much less than fluid elements (category 3). The particles in Case 1b seem to be on the borderline of the latter two categories.

One might expect Case 2a to be in category 2 or on the borderline of categories 2 and 3 because St_δ for Case 2a is comparable to St_δ for Case 1a. However, this does not appear to be the case. A probable explanation is the previously discussed differences in the large-scale flow structures of Cases 1 and 2. As discussed previously, this results in an increased Stokes number, pushing the particles of Case 2 into category 3.

In case 1a (Fig. 30), the majority of isolated particles appear to reside near the central region of the view areas, ($x = 8$ to 13 cm) and ($x = 19$ to 22 cm). While one might conclude that this is the result of selective dispersion due to some nearly stationary vortices at these streamwise locations, it is more probable that this is an effect of the Gaussian distribution of the illuminating laser sheet light. The Gaussian distribution causes the intensity of the laser sheet light to be most intense at the center and decrease toward the edges. Particles passing through the edges of the sheet are illuminated by less intense light. The resulting light intensity scattered by the particles may be so low that it is not distinguished from the background intensity by either the CCD camera or the subsequent image processing. Therefore the number of validated samples is significantly larger for the central region of the viewing areas. The apparent low particle populations from $x = 0$ to 8 cm and $x = 14$ to 19 cm are most likely not a true particle dispersion effect.

4.0 CONCLUSIONS

An extended experimental research effort has been conducted to study the effects of compressibility in high Reynolds number turbulent mixing layers. Four sets of experiments have been performed, namely (1) laser Doppler velocimetry (LDV) experiments, (2) space-time pressure correlation experiments, (3) particle-laden mixing layer experiments, and (4) filtered Rayleigh/Mie scattering experiments. Complete results have been obtained in the first three sets. Although much qualitative information has been acquired in the fourth set of experiments, work is ongoing to obtain planar instantaneous density and velocity measurements. Compressible mixing layers having convective Mach numbers (M_c) of 0.51, 0.64, and 0.86 were studied in the LDV experiments. The two extreme M_c cases were investigated in the other three sets of experiments.

All of the obtained experimental results show the effect of compressibility on the mixing layer to be significant. In accord with the results obtained by other investigators, the growth rate of the mixing layer vorticity thickness (normalized by the corresponding growth rate of an incompressible mixing layer having the same velocity ratio) decreases significantly with increasing compressibility. While the $M_c = 0.51$ mixing layer growth rate is only slightly less than that of its incompressible counterpart, the growth rate of the $M_c = 0.86$ mixing layer is approximately 50% less than that of its incompressible counterpart. Despite this, significant differences between the $M_c = 0.51$ case and the incompressible case were found in the turbulence results.

Streamwise and lateral turbulence intensities and Reynolds shear stress decrease with increasing M_c. However, the anisotropy ratio (σ_u/σ_v) distribution remains essentially constant for all M_c cases, indicating a similar compressibility effect on both normal components of the Reynolds stress. Mixing layer profiles of the correlation coefficient ($R_{uv} = -\overline{u\,v}/\sigma_u\sigma_v$) and higher order moments of velocity fluctuations indicate that compressibility sharply reduces the large structures' ability to extend into the free stream and entrain fresh fluid into the mixing region (especially at the high speed edge of the mixing region). Two-point static pressure space-time correlations were used to

36

investigate the topology and streamwise evolution of the large scale structures. For increasing streamwise probe separation, the coherence decreased much more rapidly for $M_c = 0.86$ than $M_c = 0.51$, indicating a significant compressibility effect on the streamwise evolution of the large scale structures. Convective velocities of individual large scale structures were calculated. It was found that: 1) even at $y^* \approx 0$ where the average U_c is equal to the theoretical U_c, structures have a wide range of convective velocities, 2) both the average and distribution of convective velocities change with the lateral location (y^*), and 3) the variation with y^* becomes larger as the compressibility level is increased. Spanwise correlations showed the large structures of the $M_c = 0.51$ mixing layer to be spanwise-aligned similar to those observed in incompressible mixing layers, while the large structures of the $M_c = 0.86$ case were found to be spanwise-oblique with angles within $\pm70°$. Furthermore, although the rms pressure fluctuations of the $M_c = 0.86$ case were spatially uniform in the developing region, spanwise and lateral variations were found in the fully developed region. This suggests that some degree of spanwise organization is present since the structures appear to occur at "preferred" spanwise locations. This complicated three-dimensional structure orientation is similar to that found in the direct numerical simulations of Sandham and Reynolds[1991].

Filtered Rayleigh/Mie scattering based visualizations were obtained to qualitatively assess structure topology and evolution. In accord with the pressure correlation results, the large scale structures of the $M_c = 0.51$ mixing layer were aligned in the spanwise direction and possessed well defined braid and core regions similar to the structures of incompressible mixing layers. Indications of streamwise vorticity were found in the developing region of the $M_c = 0.51$ mixing layer. Similar to the pressure correlation results, visualizations of the $M_c = 0.86$ case revealed a much decreased degree of large scale organization relative to the $M_c = 0.51$ case, with a tendency for the large structures to be oriented spanwise-oblique. Further, no evidence of streamwise vorticity was found in the $M_c = 0.86$ mixing layer.

Investigations of particle dispersion in the mixing layer for six different Stokes numbers showed stark differences between the $M_c = 0.51$ and $M_c = 0.86$ cases. For

the lowest Stokes number, the $M_c = 0.51$ mixing layer displayed a significant ability to entrain particles (originally present in the subsonic freestream) into the mixing region and subsequently disperse them into the supersonic freestream. The $M_c = 0.51$ mixing layer's ability to entrain and disperse particles decreased with increasing Stokes number, similar to results for incompressible mixing layers. The $M_c = 0.86$ mixing layer was unable to entrain and disperse the solid particles. Instead, the particle trajectories seem to reflect the asymmetric development of the shear layer. As previously discussed, the streamline divergence associated with growth of the shear layer is skewed towards the subsonic free stream. The lower levels of particle dispersion are thought to result from the decreased large scale organization in the $M_c = 0.86$ mixing layer. It is likely that the less-organized, three-dimensional large scale structures result in a smaller flow length scale, and subsequently higher Stokes number, St. This could conceivably account for the lower levels of particle dispersion.

5.0 REFERENCES

Barre, S., Quine, C., and Dussauge, J.P., 1992, "Compressibility Effects on the Structure of Supersonic Mixing Layers: Experimental Results," Note IMST 1/92, Marseille, France.

Bernal, L.P. and Roshko, A., 1986, "Streamwise Vortex Structure in Plane Mixing Layers," J. Fluid Mech., 170, 499-525.

Birch, S.F. and Eggers, J.M., 1972, "A Critical Review of the Experimental Data for Developed Free Shear Layers, Free Turbulent Shear Flows, NASA SP 321, pp. 11-40.

Bogdanoff, D.W., 1983, "Compressibility Effects in Turbulent Shear Layers," AIAA J., 21, 926-927.

Bonnet, J.P. and Debisschop, J.R., 1992, "Analyse Experimentale de la Turbulence dans les Couche de Melange Supersonique," CEAT, Poitiers, France; also AIAA Paper, January 1993.

Bradshaw, P., 1977, "Compressible Turbulent Shear Layers," Ann Rev Fluid Mech, 63, 449-464.

Browand, F.K., and Troutt, T.R., 1980, "A Note on Spanwise Structure in the Two-Dimensional Mixing Layer," J. Fluid Mech., 917, 771-781.

Brown, G.L. and Roshko, A., 1974, "On Density Effects and Large Scale Structure in Turbulent Mixing Layers," J. Fluid Mech, 64, 775-816.

Chein, R., and Chung, J.N., 1988, "Simulation of Particle Dispersion in a Two-Dimensional Mixing Layer," AIChE Journal, Vol. 36, No. 6, pp. 946-954.

Chinzei, N., Masuya, G., Komuro, T., Murakami, A., and Kodou, K., 1986, "Spreading of Two Stream Supersonic Turbulent Mixing Layer," Phys Fluids, 29, 1345-1347.

Clark, R.L., Jr., Ng, W.F., Rettew, A.L., Walker, D.A., and Schetz, J.A., 1988, "Turbulence Measurements in a High Speed Shear Flow Using a Dual-Wire Probe," AIAA-88-3055A.

Clemens, N.T. and Mungal, M.G., 1991, "A Planar Mie Scattering Technique for Visualizing Supersonic Mixing Flows," Experiments in Fluids, Vol. 11, pp. 175-185.

Clemens, N.T. and Mungal M.G., 1992a, "Two- and Three- Dimensional Effects in the Supersonic Mixing Layer," AIAA Journal, Vol. 30, pp. 973-981.

Clemens, N.T. and Mungal M.G., 1992b, "Effects of Sidewall Disturbances on the Supersonic Mixing Layer," J. Propulsion, Vol.8 , No. 1, pp. 249-250.

Crowe, C.T., Gore, R.A., and Troutt, T.R., 1985, "Particle Dispersion by Coherent Structures in Free Shear Flows,"Particulate Science and Technology, Vol. 3, pp. 149-158.

Crowe, C.T., Chung, J.N., and Troutt, T.R., 1988, "Particle Mixing in Free Shear Flows," Prog. Energy Combust. Sci., Vol. 14, pp. 171-194.

Dimotakis, P.E. and Brown, G.L., 1976, "The Mixing Layer at High Reynolds Number: Large-Structure Dynamics and Entrainment," J. Fluid Mech, 78, 535-560.

Dolling, D.S., Fournier, E., and Shau, Y.R., 1990, "Effects of Vortex Generators on the Growth Rate of a Compressible Turbulent Shear Layer," AIAA-90-1979.

Elliott, G.S., 1989, "Effects of Compressibility on Free Shear Layers," Masters Thesis, The Ohio State University.

Elliott, G.S. and Samimy, M., 1990, "Compressibility Effects in Free Shear Layers," Phys Fluids, 2, 1231-1240.

Elliott, G.S., Samimy, M., and Arnette, S.A., 1992, "A study of Compressible Mixing Layers Using Filtered Rayleigh Scattering," AIAA-92-0175; also will appear in Vol. 30, no. 11 of AIAA Journal.

Fernandez, F.L. and Zukoski, E.E., 1969, "Experiments in Supersonic Turbulent Flow with Large Distributed Surface Injection", AIAA Journal, Vol. 7, No. 9, pp. 1759-1767.

Fourguette, D.C., Mungal, M.G. and Dibble, R.W., 1991, "Time Evolution of the Shear Layer of a Supersonic Axisymmetric Jet at Matched Conditions," AIAA Journal, Vol. 29, pp. 1123-1130.

Glawe, D.D., 1991, "Dispersion of Large Particles in Compressible Free Shear Layers", M.S. Thesis, Ohio State University.

Glawe, D. and Samimy M., 1992, "Dispersion of Particles in Compressible Mixing Layers," AIAA-92-0176; also will appear in Journal of Propulsion and Power.

40

Goebel, S. and Dutton, J.C., 1991, "Experimental Study of Compressible Turbulent Mixing Layers," AIAA J., 29, 538-546.

Gutmark, E., Schadow, K.C., and Wilson, K.J., 1991, "Effect of Convective Mach Number on Mixing of Coaxial Circular and Rectangular Jets," Phys. Fluids, Vol. 3, pp. 29-36.

Hanson, R.K., Chang, A.Y., Seitzman, J.M. Lee, M.P., Paul, P.H. and Battles, B.E., 1990, "Laser-Induced Fluorescence Diagnostics for Supersonic Flows," AIAA-90-0625.

Ikawa, H., 1973, "Turbulent Mixing Layer Experiment in Supersonic Flow," Ph.D. Thesis, California Institute of Technology.

Ikawa, H. and Kubota, T., 1975, "Investigation of Supersonic Turbulent Mixing Layer with Zero Pressure Gradient," AIAA J., 13, 566-572.

Jackson, T.L. and Grosch, C.E., 1989, "Inviscid Spatial Stability of a Compressible Mixing Layer," J. Fluid Mech, 208, 609-637.

Jimenez, J., 1983, "A Spanwise Structure in the Plane Shear Layer," J. Fluid Mech, 197, 319-336.

Jones, G., Planchon, H.P., and Hammersly, R.J., 1973, "Turbulent Correlation Measurements in a Two-Stream Mixing Layer," AIAA J., 11, 1146-1150.

Kamalu, N., Wen, F., Troutt, T.R., Crowe, C.T., and Chung, J.N., "Particle Dispersion by Ordered Motion in Turbulent Mixing Layers, 1988, " ASME Forum on Cavitation and Multiphase Flow, pp. 150-154.

Kamalu, N., Tang, L., Troutt, T.R., Chung, J.N., and Crowe, C.T., "Particle Dispersion in Developing Shear Layers, 1989, " International Conference on Mechanics of Two-Phase Flows, Taipei, Taiwan, pp. 199-202.

Komine, H., Brosnan, S.J., Litton, A.B. and Stappaerts, E.A., 1991, "Real-Time Doppler Global Velocimetry," AIAA-91- 0337.

Lázaro, B.J., and Lasheras, J.C., 1989, "Particle Dispersion in a Turbulent, Plane, Free Shear Layer," Physics of Fluids A, Vol. 1, No. 6, pp.1035-1044.

Lasheras, J.C., Cho J.S., and Maxworthy, T., 1986, "On the Origin of Streamwise Vortical Structures in a Plane Free Shear Layer," J. Fluid Mech, 172, 231-258.

Lele, S., 1989, "Direct Numerical Simulation of Compressible Free Shear Flows," AIAA-89-0374.

Longmire, E.K., 1990, "Structure and Control of a Particle-Laden Jet," PhD Thesis, Stanford University, California.

Lu, P.J. and Wu, K.C., 1991, "Numerical Investigation on the Structure of a Confined Supersonic Mixing Layer," Phys. Fluids A, Vol. 3, PP. 3063-3079.

McLaughlin, D.K., Martens, S., and Kinzie, K.W., 1992, "An Experimental Investigation of Large Scale Instabilities in a Low Reynolds Number Two-Stream Supersonic Shear Layer," AIAA-92-0177.

McIntrye S.S. and Settles, G.S., 1991, "Optical Experiments on Axisymmetric Compressible Turbulent Mixing Layers," AIAA-91-0623.

Messersmith, N.L., Dutton, J.C., and Krier, H., 1991, "Experimental Investigation of Large Scale Structures in Compressible Mixing Layers," AIAA Paper 91-0244.

Miles, R.B., Lempert, W.R. and Forkey, J., 1991, "Instantaneous Velocity Fields and Background Suppression by Filtered Rayleigh Scattering," AIAA-91-0357.

Morkovin, M.V., 1961, "Effects of Compressibility on Turbulent Flows," Mechanique de la Turbulence, Marseille, France.

Morkovin, M.V., 1991, "Mach Number Effects on Free and Wall Turbulent Structures in Light of Instability Flow Interactions," in Studies in Turbulence (ed., Gatski, Sarkar, and
Speziale), Springer-Verlag, 1991.

Morris, P.J. and Giridharan, M.G., 1991, "The Effect of Walls on Instability Waves in Supersonic Shear Layers," Phys. Fluids A, Vol. 3, pp. 356-358.

Naughton, J.W., Cattafesta, L., and Settles. G.S., 1989, "An Experimental Stud of the Effect of Streamwise Vorticity on Supersonic Mixing Enhancement," AIAA-89-2456.

Oster, D. and Wygnanski, I., 1982, "The Forced Mixing Layer Between Parallel Streams," Journal of Fluid Mechanics, Vol. 123, pp. 91-130.

Papamoschou, D. and Roshko, A., 1988, "The Compressible Turbulent Mixing Layer: an Experimental Study," J. Fluid Mech, 197, 453-477.

Papamoschou, D., 1991, "Structure of the Compressible Turbulent Shear Layer," AIAA J., 29, pp. 680-681; also, AIAA Paper AIAA-89-0126.

Petrie, H.L., 1984, "A Study of Compressible Turbulent Free Shear Layers Using Laser Doppler Velocimetry, Ph.D. Thesis, University of Illinois.

Petrie, H.L., Samimy, M., and Addy, A.L., 1986, "Compressible Separated Flows," AIAA Journal, Vol. 24, pp. 1971-1978.

Ragab, S.A. and Wu, J.L., 1989, "Linear Instabilities in Two-Dimensional Compressible Mixing Layers, Phys Fluids, 1, 957-966.

Reeder, M.F., 1991, "A Study of the Effects of Compressibility in Mixing Layers Using Two-Probe Pressure Correlations," MS Thesis, Ohio State University.

Samimy, M., Petrie, H.L., and Addy, A.L., 1986, "A Study of Compressible Turbulent Reattaching Free Shear Layers," AIAA Journal, Vol. 24, pp. 209-267.

Samimy, M. and Abu-Hijleh, B.A./K., 1989, "Performance of LDV with Polydisperse Seed Particles in High Speed Flows," Journal of Propulsion and Power, pp. 21-25.

Samimy, M., Erwin, D.E., and Elliott, E.S., 1989, "Compressibility and Shock Wave Interaction Effects on Free Shear Layers," AIAA-89-2460.

Samimy, M. and Elliott, G.S., 1990, "Effects of Compressibility on the Characteristics of Free Shear Layers," AIAA J., 28, 439-445.

Samimy, M., and Lele, S.K., 1990, "Particle-Laden Compressible Free Shear Layers," AIAA-90-1977.

Samimy, M., and Lele, S.K., 1991, "Motion of Particles with Inertia in a Compressible Free Shear Layer," Physics of Fluid A, Vol. 3, No. 8, pp. 1915-1923.

Samimy, M., Elliott, G.S., and Erwin, D.E., 1991a, "Shock Wave/Free Shear Layer Interaction," Intl. J. of Gas Turbines and Jet Engines, Vol. 8.

Samimy, M., Zaman, K.B.M.Q., and Reeder, M.F., 1991b, "Supersonic Jet Mixing Enhancement by Vortex Generators," AIAA-91-2263.

Samimy, M., Reeder, M.F., and Elliott, G.S., 1992, "Compressibility Effects on Large Structures in Free Shear Flows," Physics of Fluids A, Vol. 4, No. 6, pp. 1251-1258.

43

Sandham, N.D. and Reynolds, W.C., 1991, "Three-dimensional Simulations of Large Eddies in the Compressible Mixing Layer," Journal of Fluid Mech., Vol. 224, pp. 133- 158.

Sarkar, S. and Lakshmanan, B., 1991, "Application of a Reynolds Stress Turbulence Model to the Compressible Shear Layer," AIAA Journal, Vol. 29, pp. 743-749.

Schlichting, 1964, Boundary Layer Theory, 6th Edition, McGraw-Hill, pp. 689-690.

Shau, Y.R. and Dolling, D.S., 1990, "The Detection of Large Scale Structure in Undisturbed and Disturbed Comp. Turbulent Free Shear Layers," AIAA Paper 90-0711.

Shimitzu, H., Lee, S.A., and C.Y. She, 1983, "High Spectral Resolution Lidar System with Atomic Blocking Filters for Measuring Atmospheric Parameters," Applied Optics, Vol. 22, pp. 1373-1381.

Smith, D.R., Poggie, J., Konrad, W. and Smits, A.J., 1991, "Visualization of the Structure of Shock Wave Turbulent Boundary Layer Interactions Using Rayleigh Scattering," AIAA-91-0651.

Smits, A.J., Alving, A.E., Smith, R.W., Spina, E.F., Fernando, E.M., and Donovan, J.F., 1988, "A Comparison of the Turbulence Structure of Subsonic and Supersonic Boundary Layers," Proc. of the 11th symposium on Turbulence, Univ. of Missouri at Rolla.

Snyder, T.S., Jarymowycz, T.A., Pace, K.K., and Kuo, K.K., 1990, "Solid Fuel Ignition and Combustion Characteristics under High-Speed Crossflows," AIAA/SAE/ASME/ASEE 26th Joint Propulsion Conf., AIAA 90-2075.

Soetrisno, M., Greenough, J.A., Eberhardt, D.S., Riley, J.J., 1989, "Confined Compressible Mixing Layers: Part I. Three dimensional instabilities," AIAA Paper 89-1810.

Tam, C.K.W. and Hu, Q.F., 1989, "The Instability and Acoustic Wave Modes of SuperSonic Mixing Layers Inside a Rectangular Channel," J. Fluid Mech, 203, 51-76.

Tillman, T.G., Paterson, R.W., and Presz, W.M., 1992, "Supersonic Nozzle Mixer Ejector," Journal of Propulsion and Power, Vol. 8, 1992, pp. 513-519.

Waltrup, P.J., 1987, "Liquid-Fueled Supersonic Combustion Ramjets: A Research Perspective," Journal of Propulsion, Vol. 3, No. 6, pp. 515-524.

Zaman, K.B.M.Q., Reeder, M.F., and Samimy, M., 1992, "Supersonic Jet Mixing Enhancement by "Delta Tabs"'" AIAA-92-3548.

Zeman, O., 1990a, "Dilation Dissipation: The Concept and Application in Modeling Compressible Mixing Layers," Phys. Fluids A, pp. 178-188.
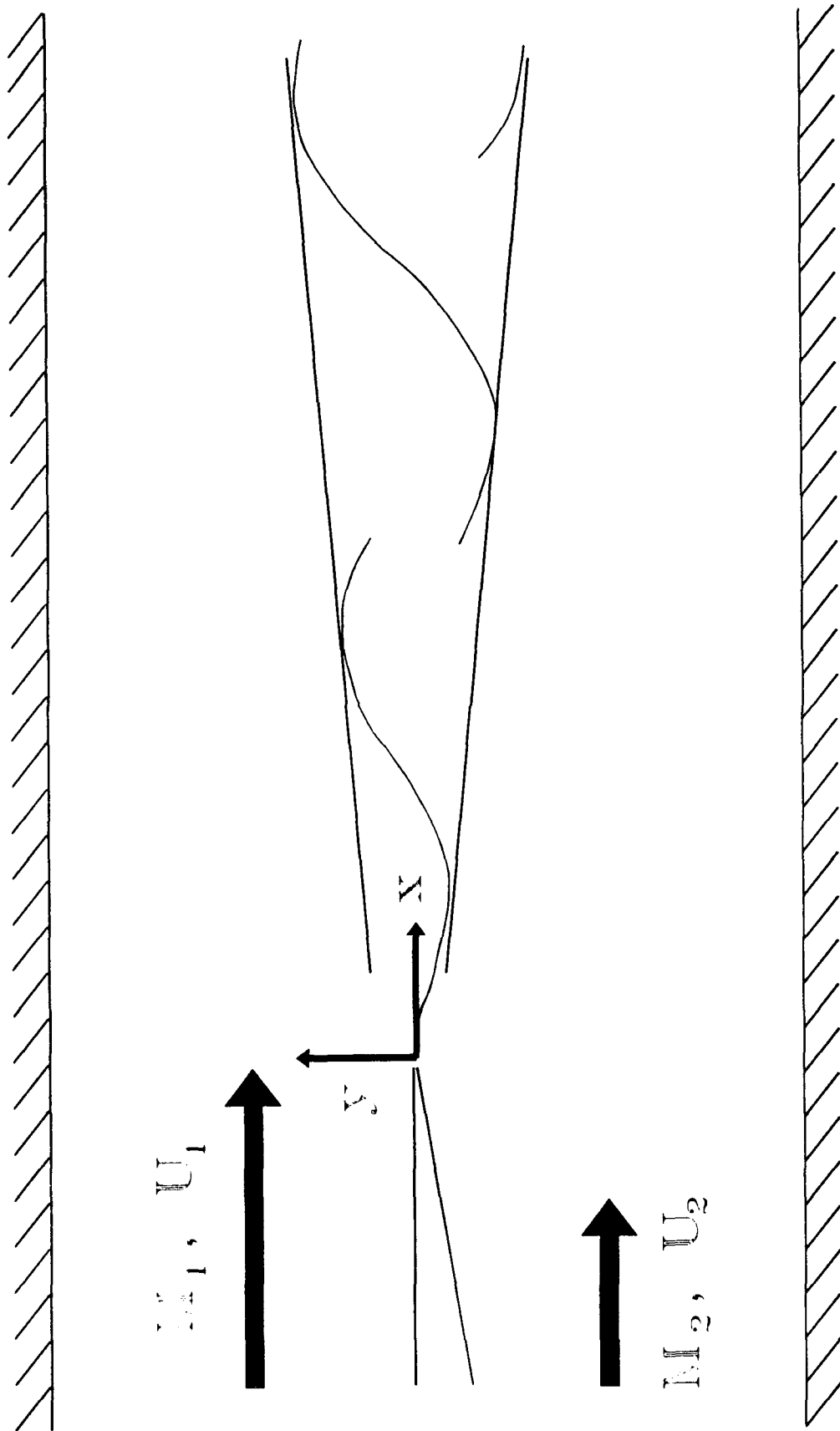
Fig. 1 Schematic of the flow field

46
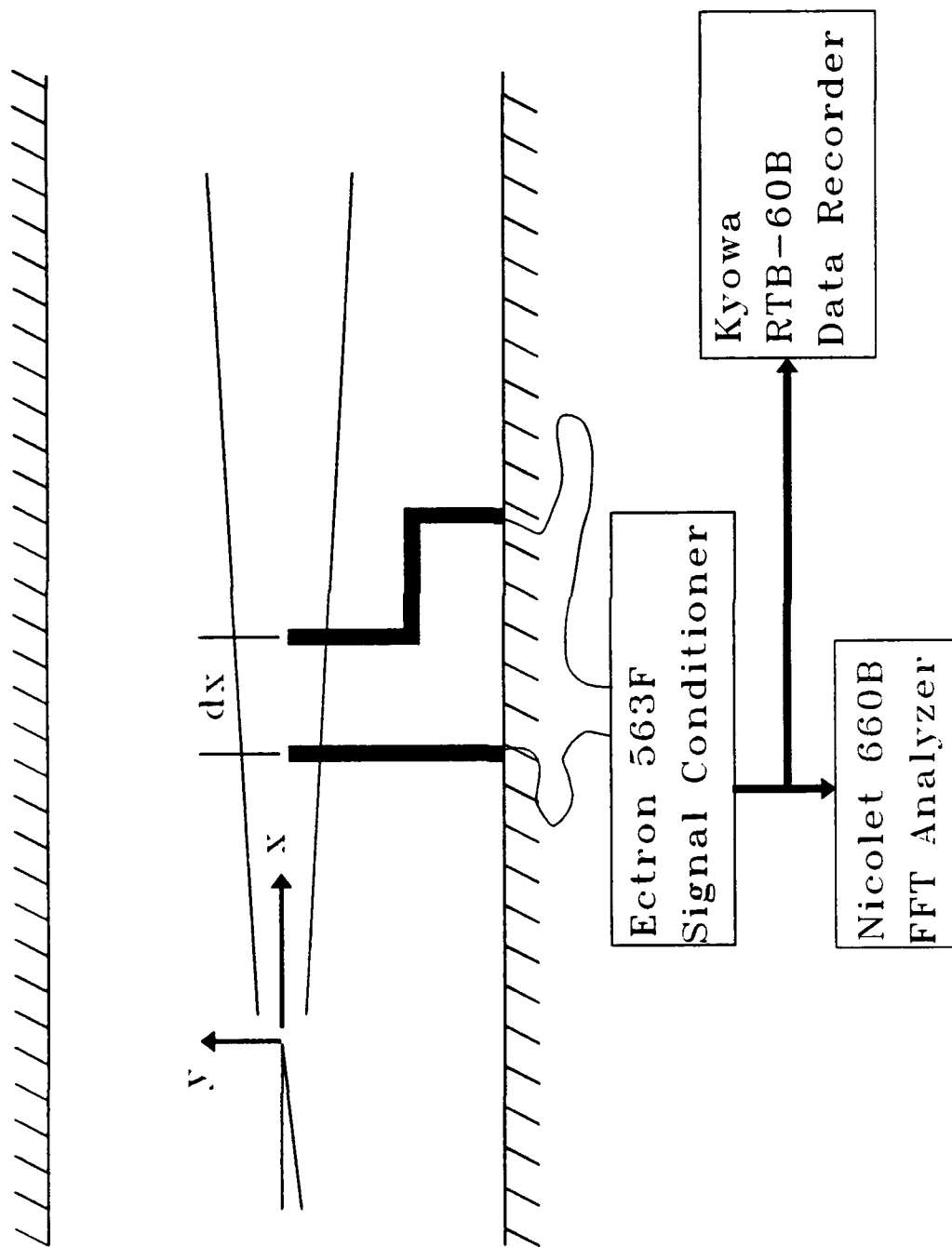
Fig. 2 Schematic of the test section with pressure probes in it

47
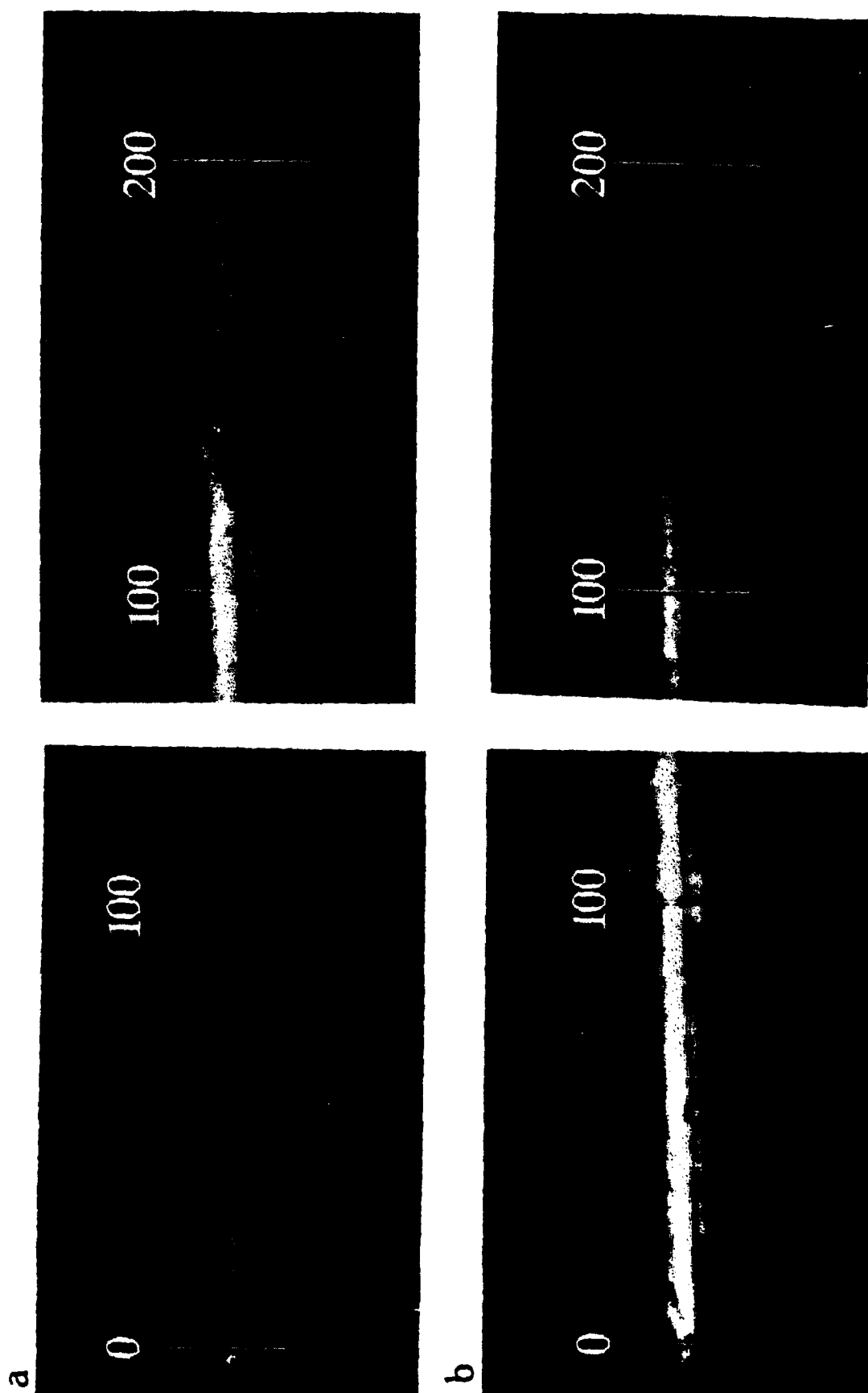
Fig. 3 Schlieren image of $M_c = 0.51$ a) without injection wedge b) with injection wedge
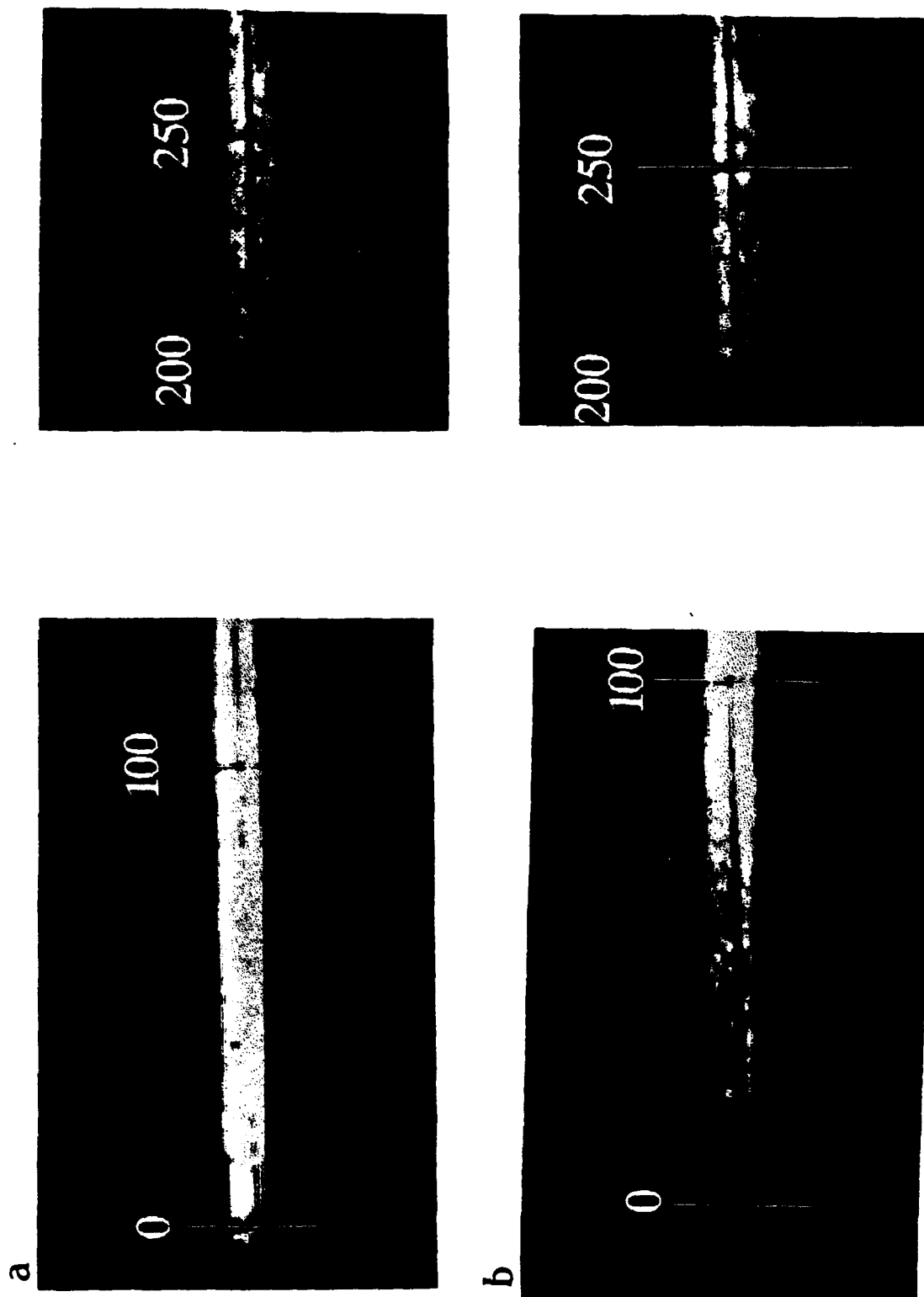
Fig. 4 Schlieren image of $M_c = 0.86$ a) without injection wedge b) with injection wedge
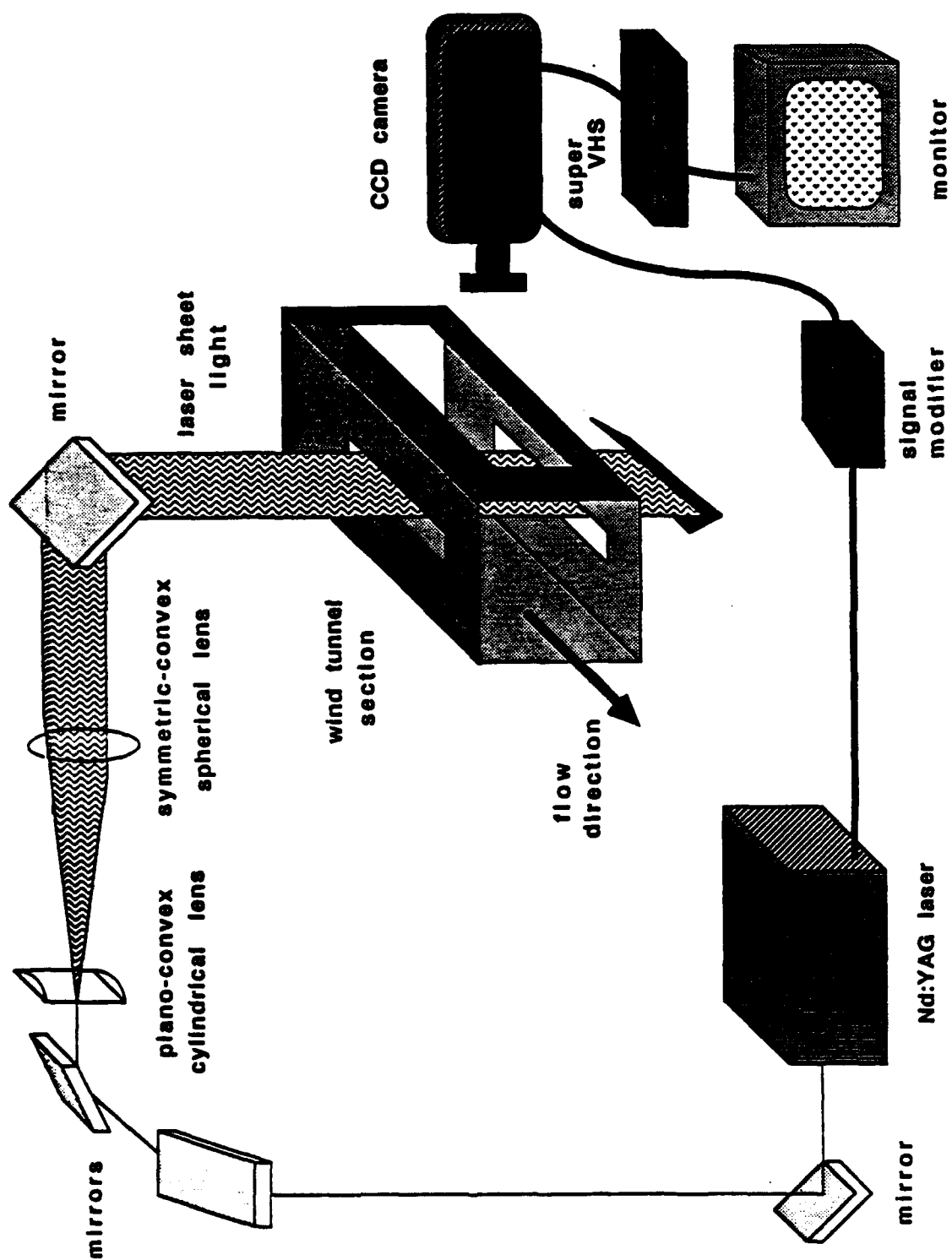
Fig. 5 Laser sheet lighting and image recording system
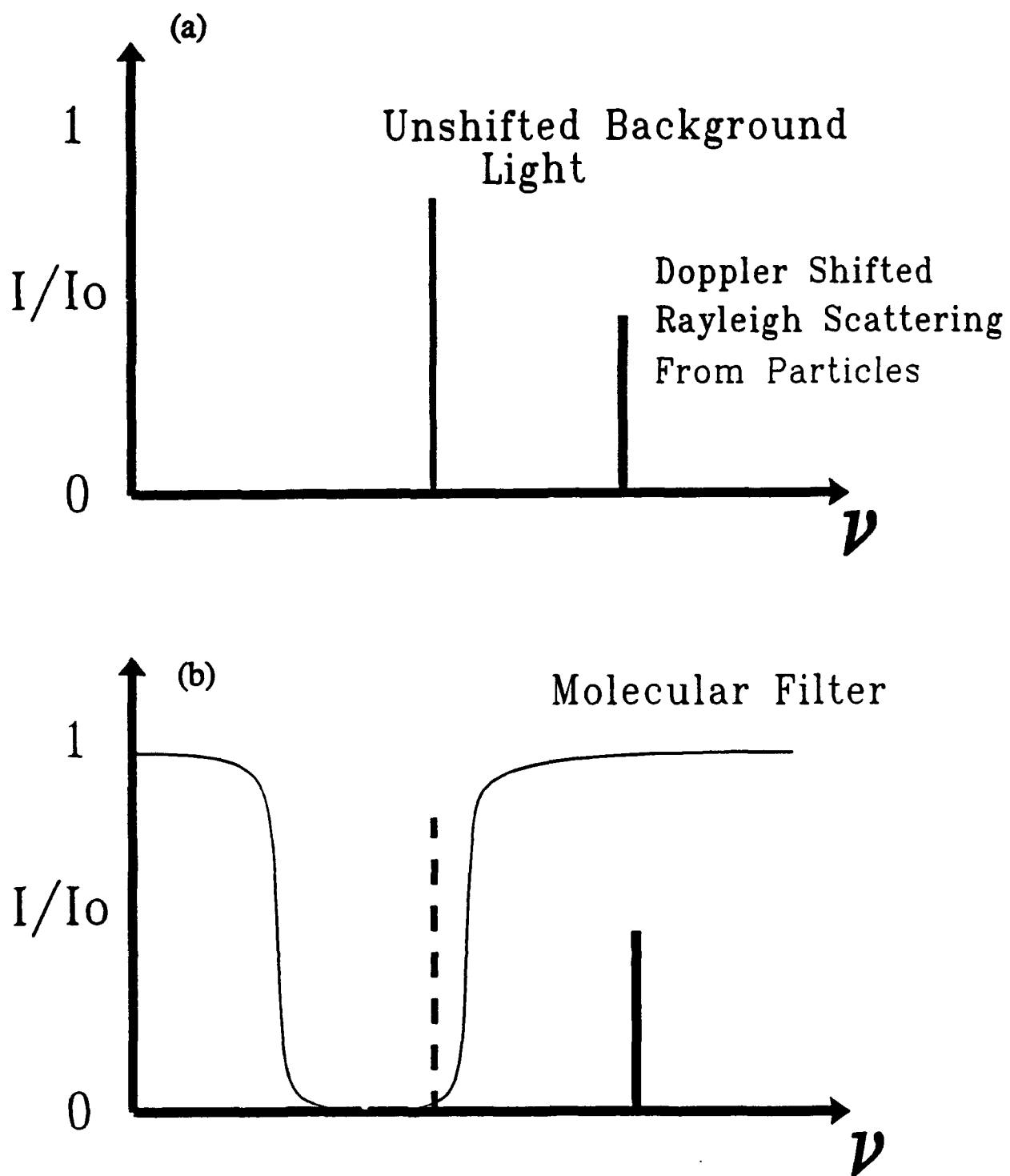
Fig. 6 Filter Rayleigh scattering technique using particles as the scattering medium
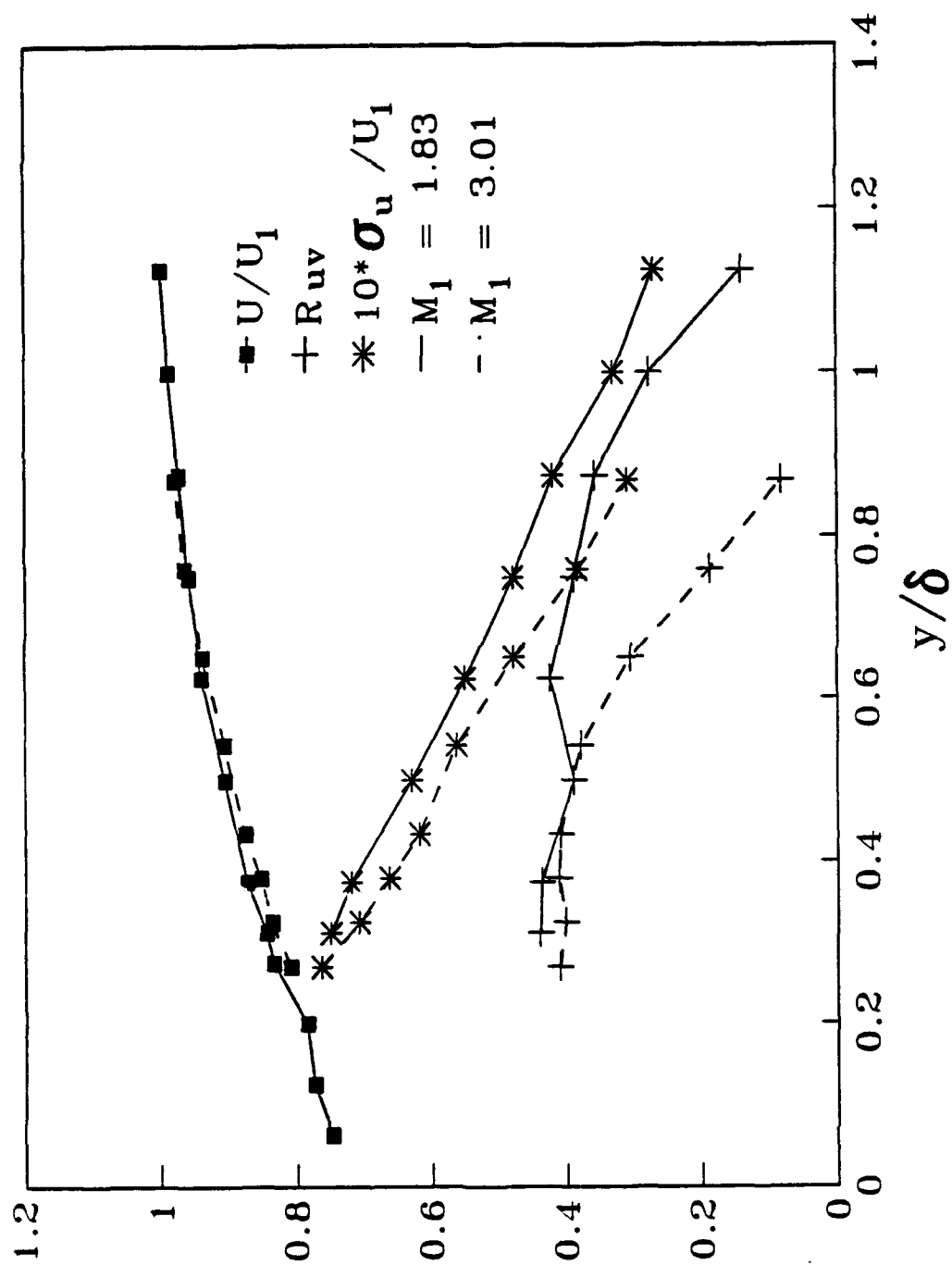
Fig. 7 Incoming boundary layer characteristics U/U₁, R_uv, and 10*σ_u/U₁, for both incoming flows
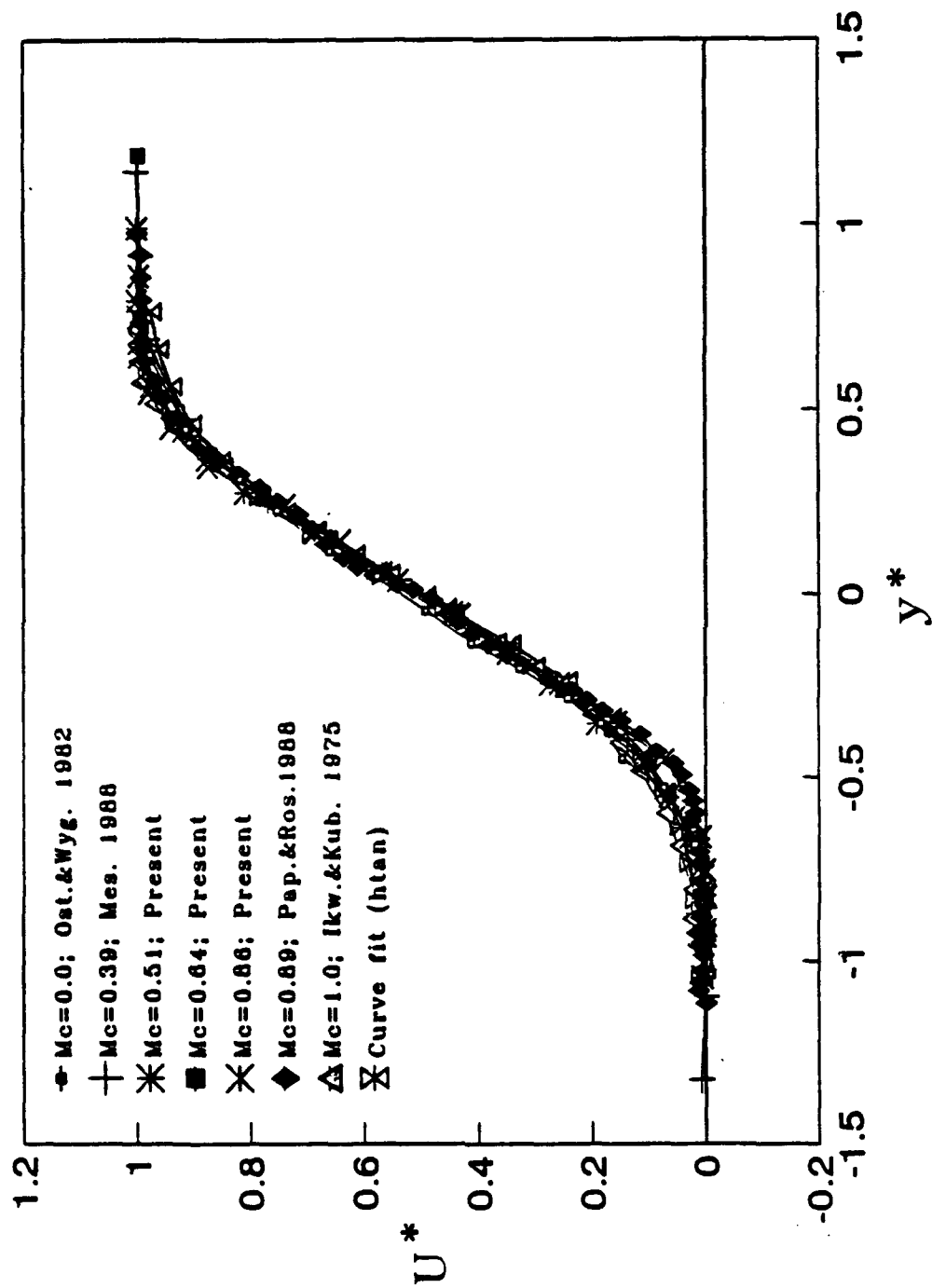
Fig. 8 The mean velocity profiles from various experiments
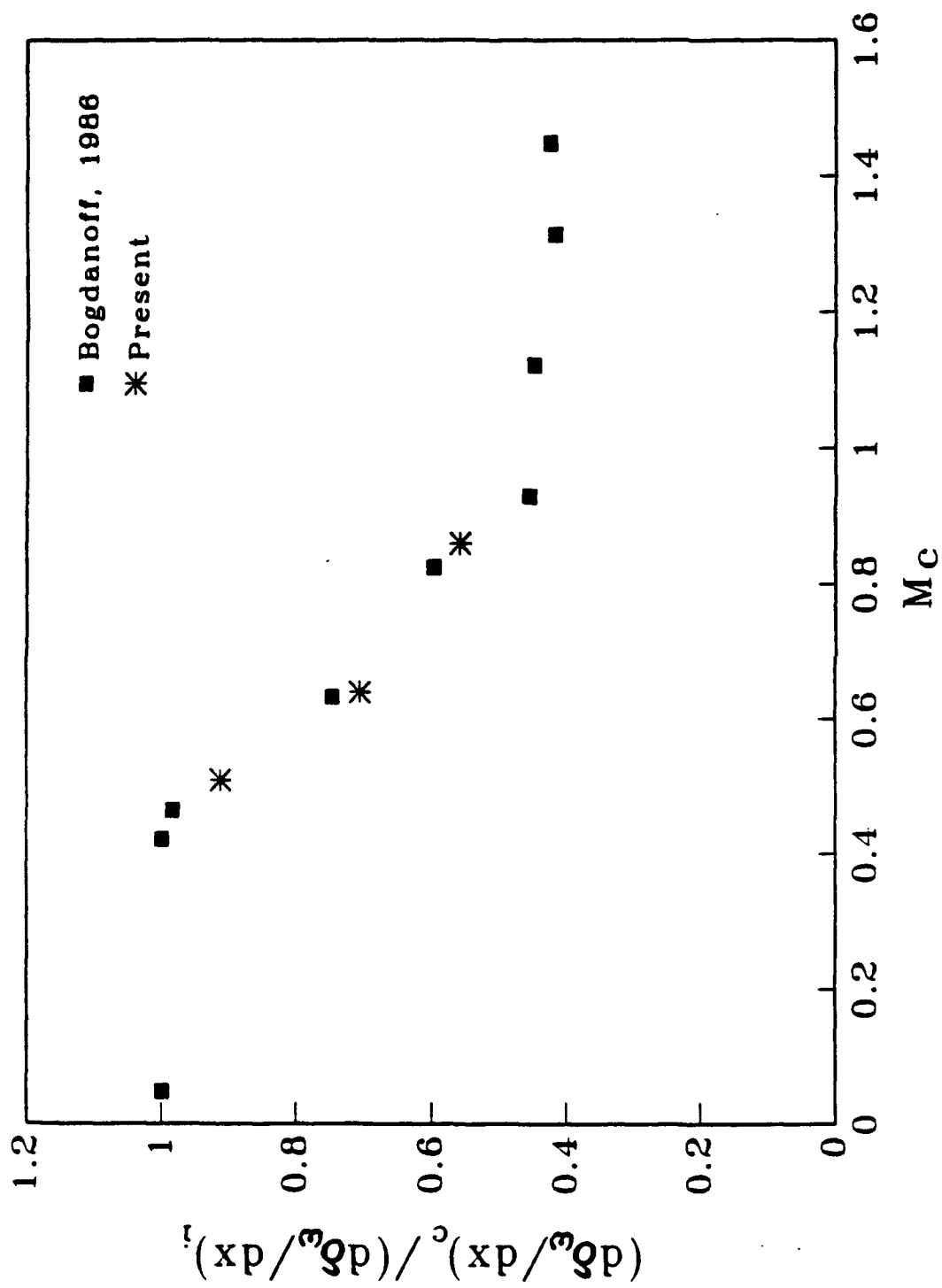
Fig. 9 Vorticity growth rate from various experiments
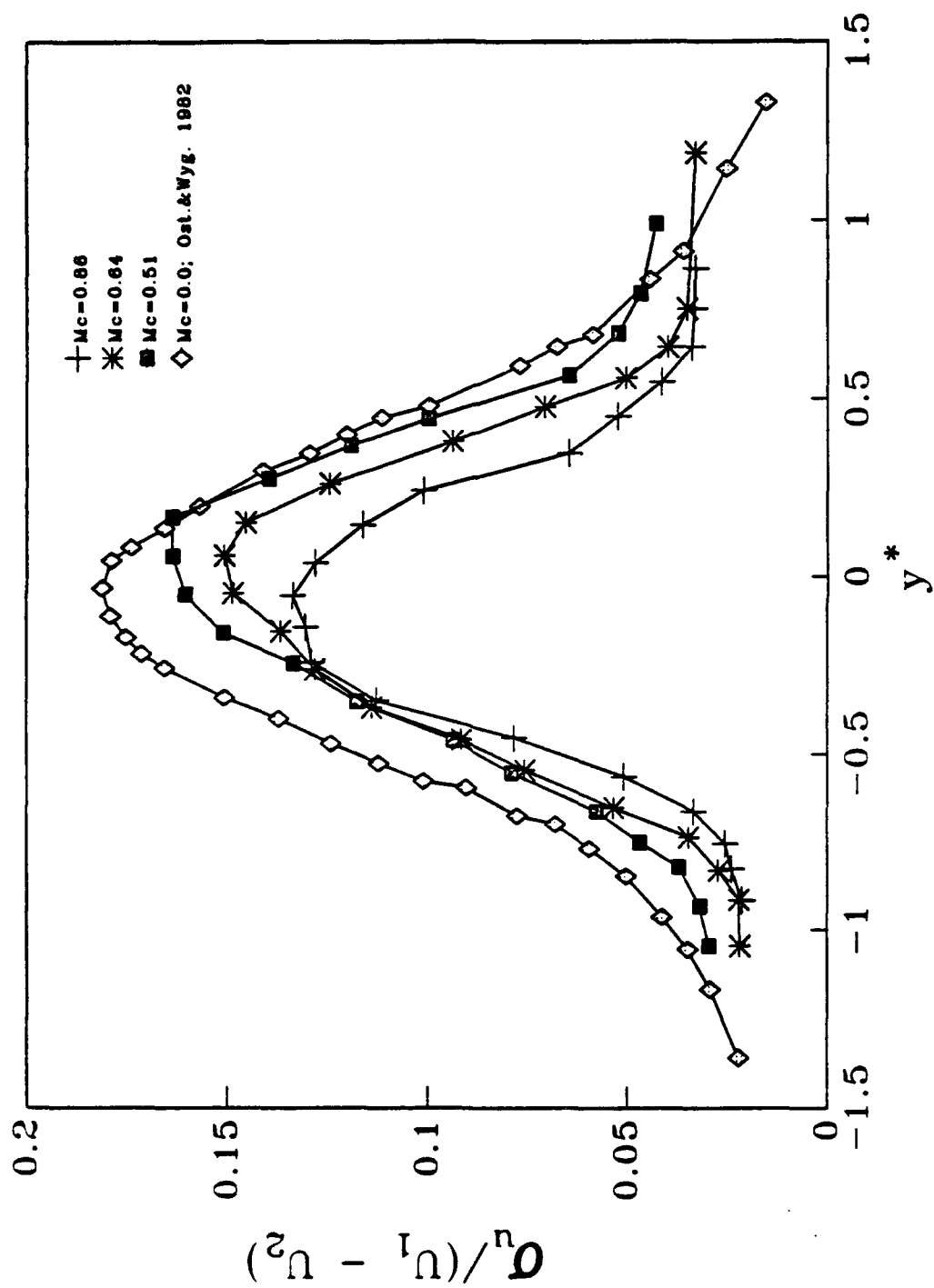
Fig. 10 Streamwise turbulence intensity in the fully developed region
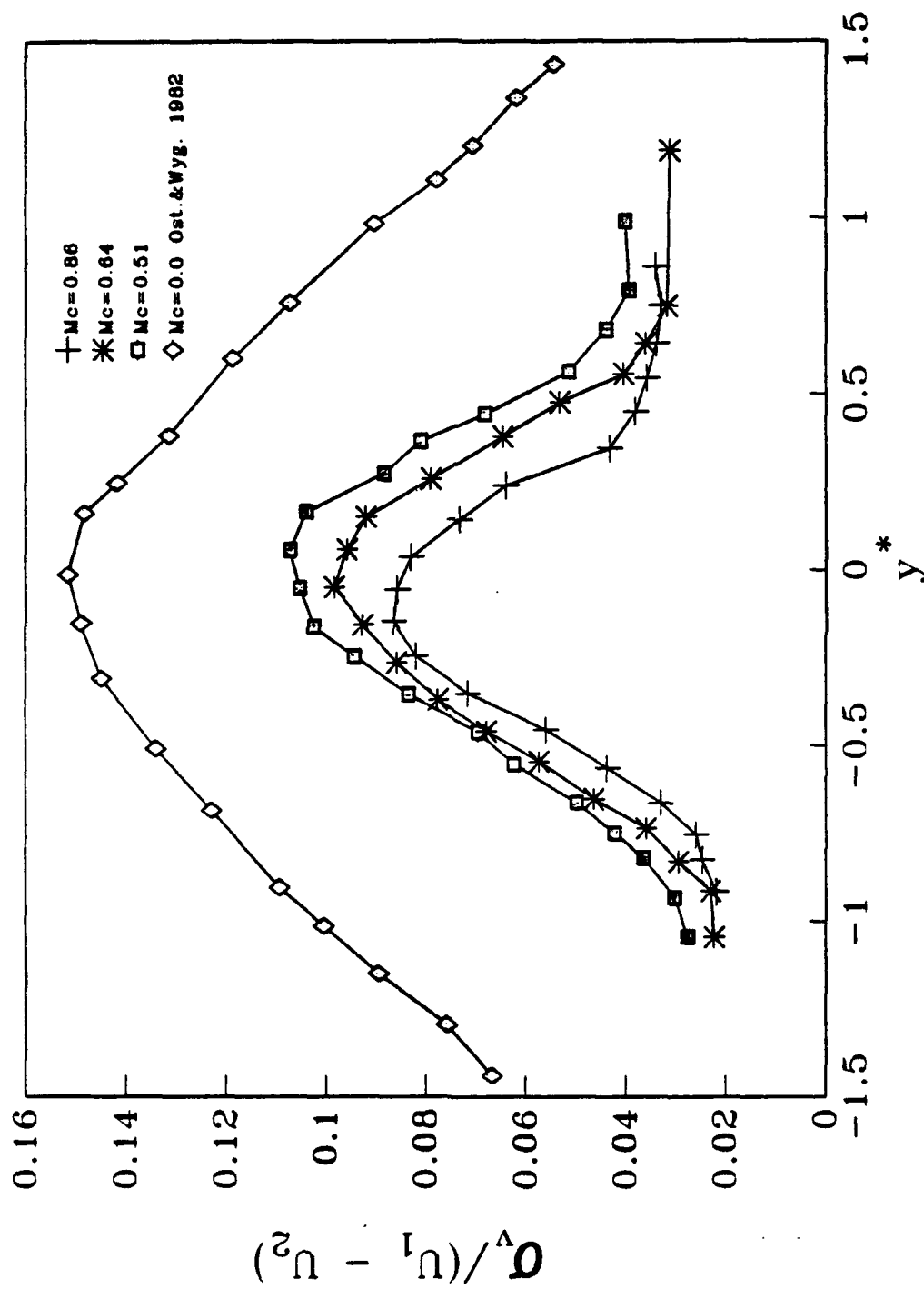
Fig. 11 Lateral turbulence intensity in the fully developed region
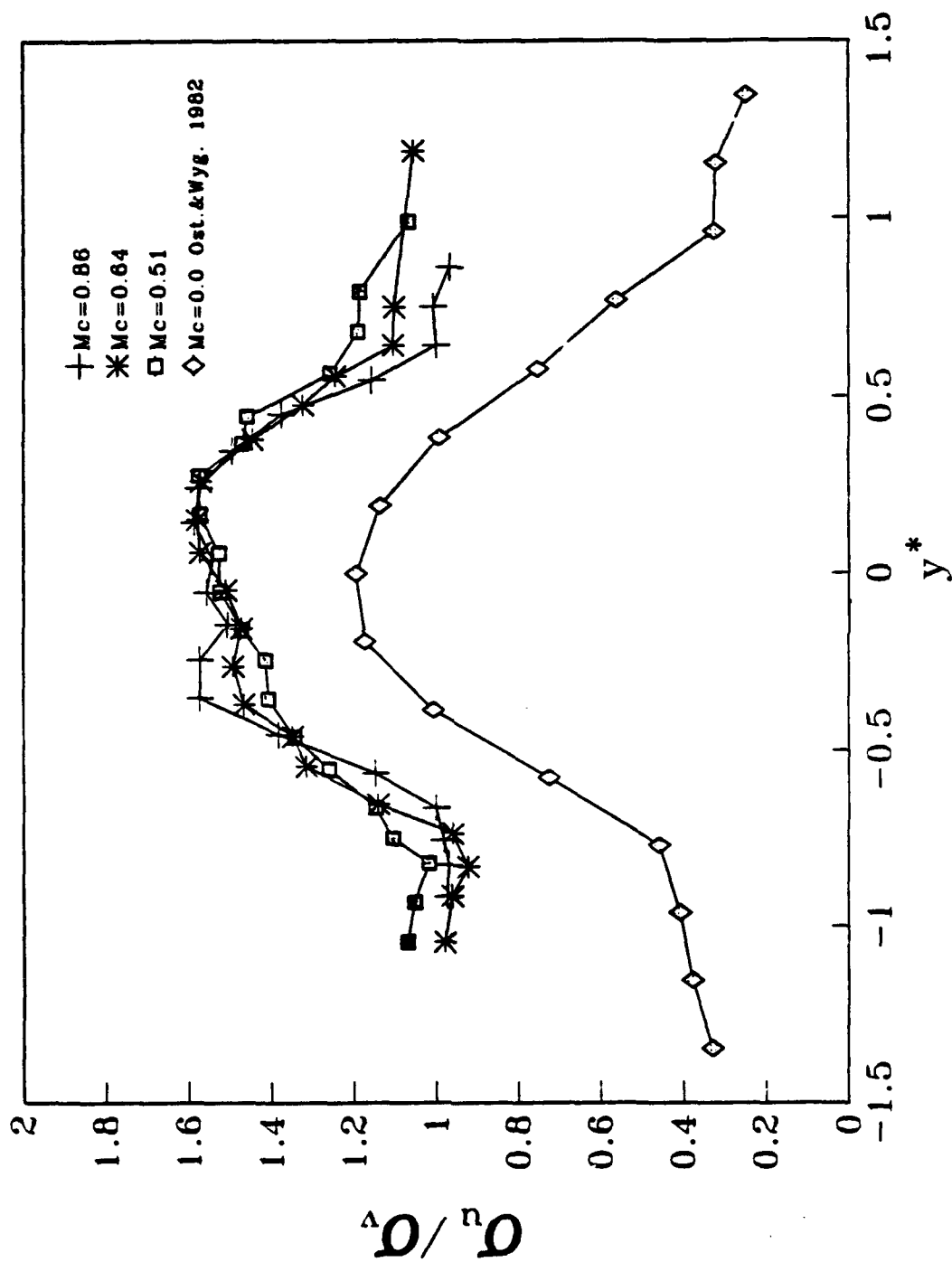
Fig. 12 Anisotropy ratio for the fully developed region

57
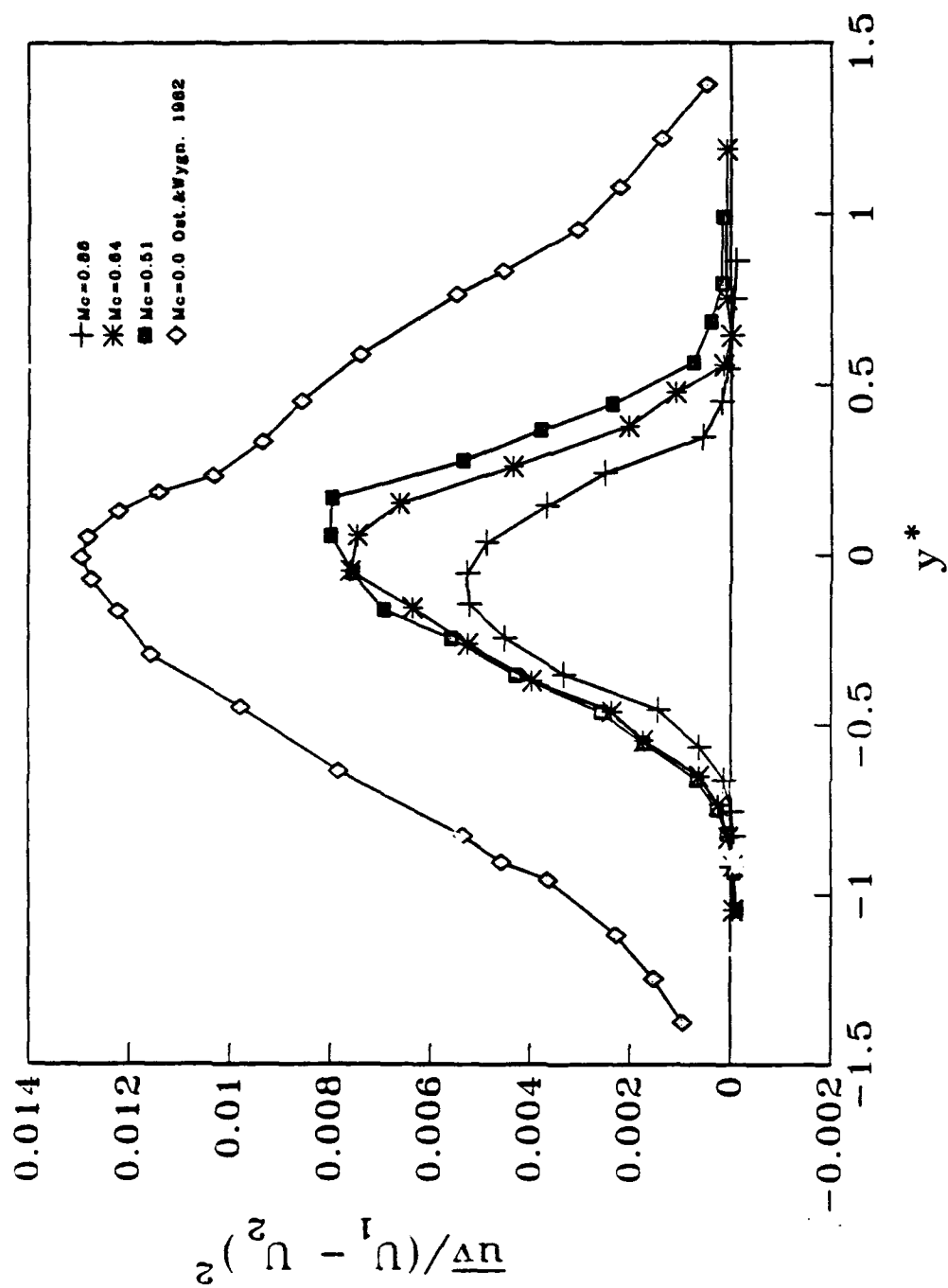
Fig. 13 Reynolds stress profiles in the fully developed region.
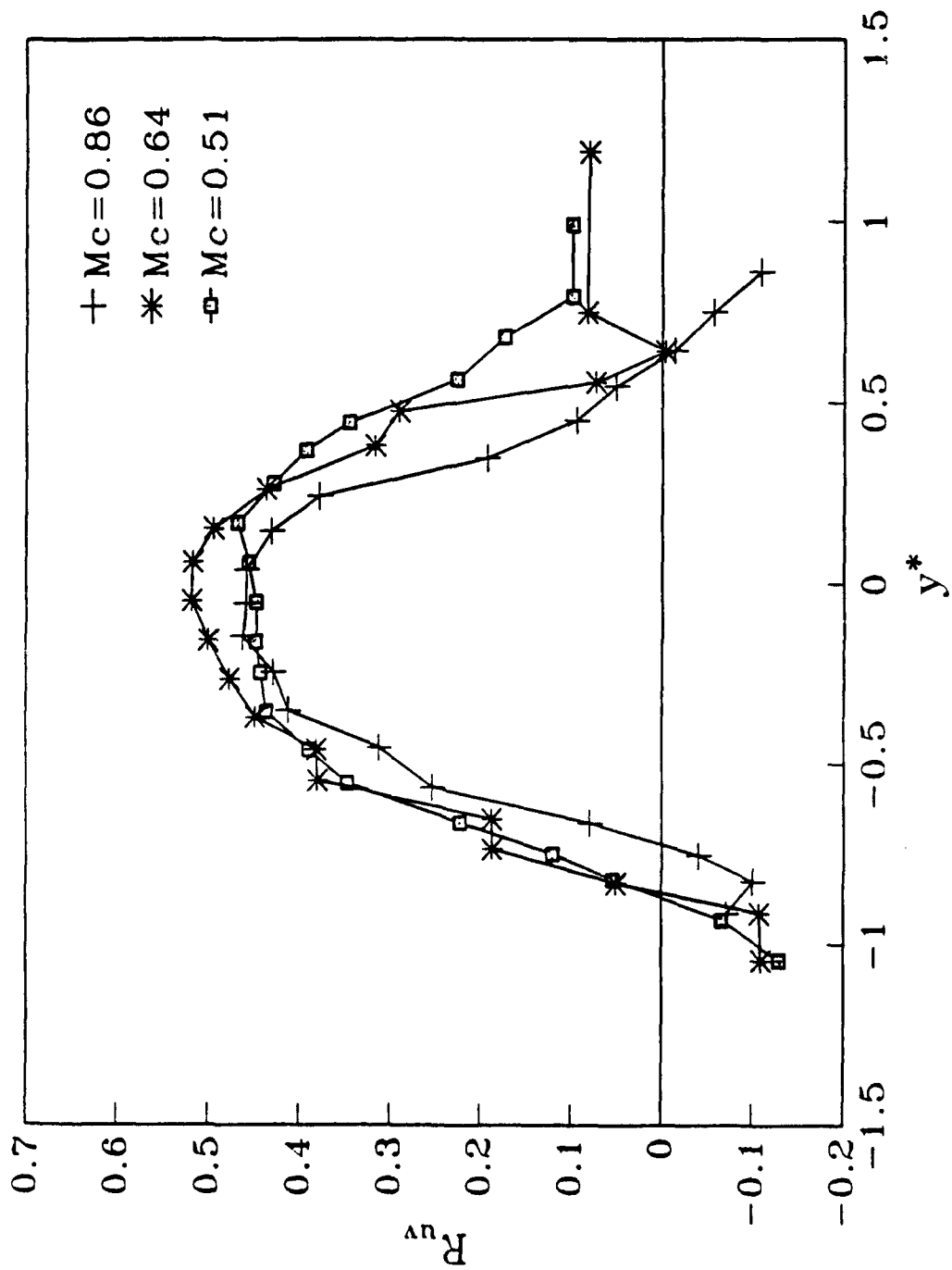
Fig. 14 Correlation coefficient for the fully developed region
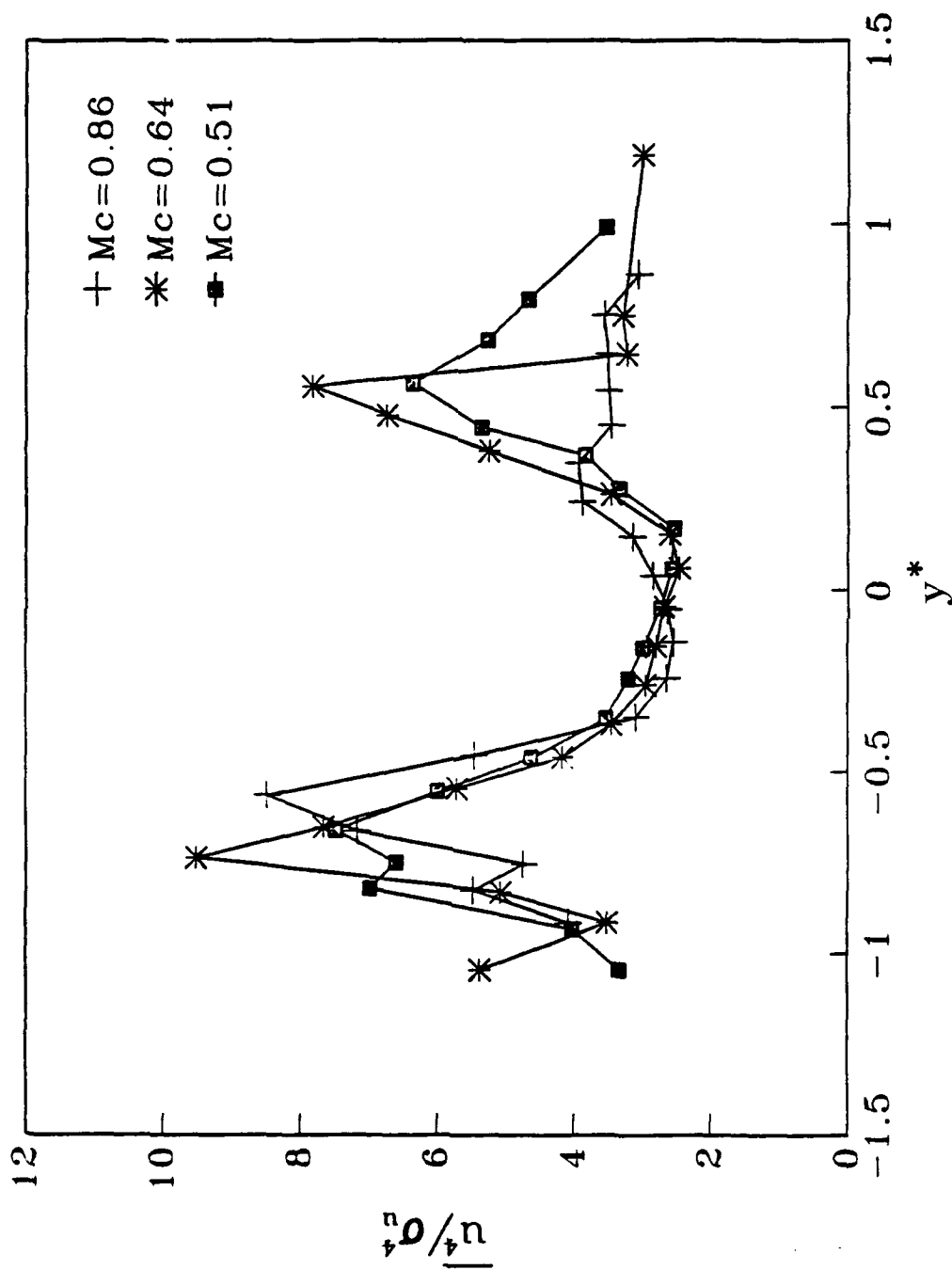
Fig. 15 Streamwise flatness in the fully developed re3ion
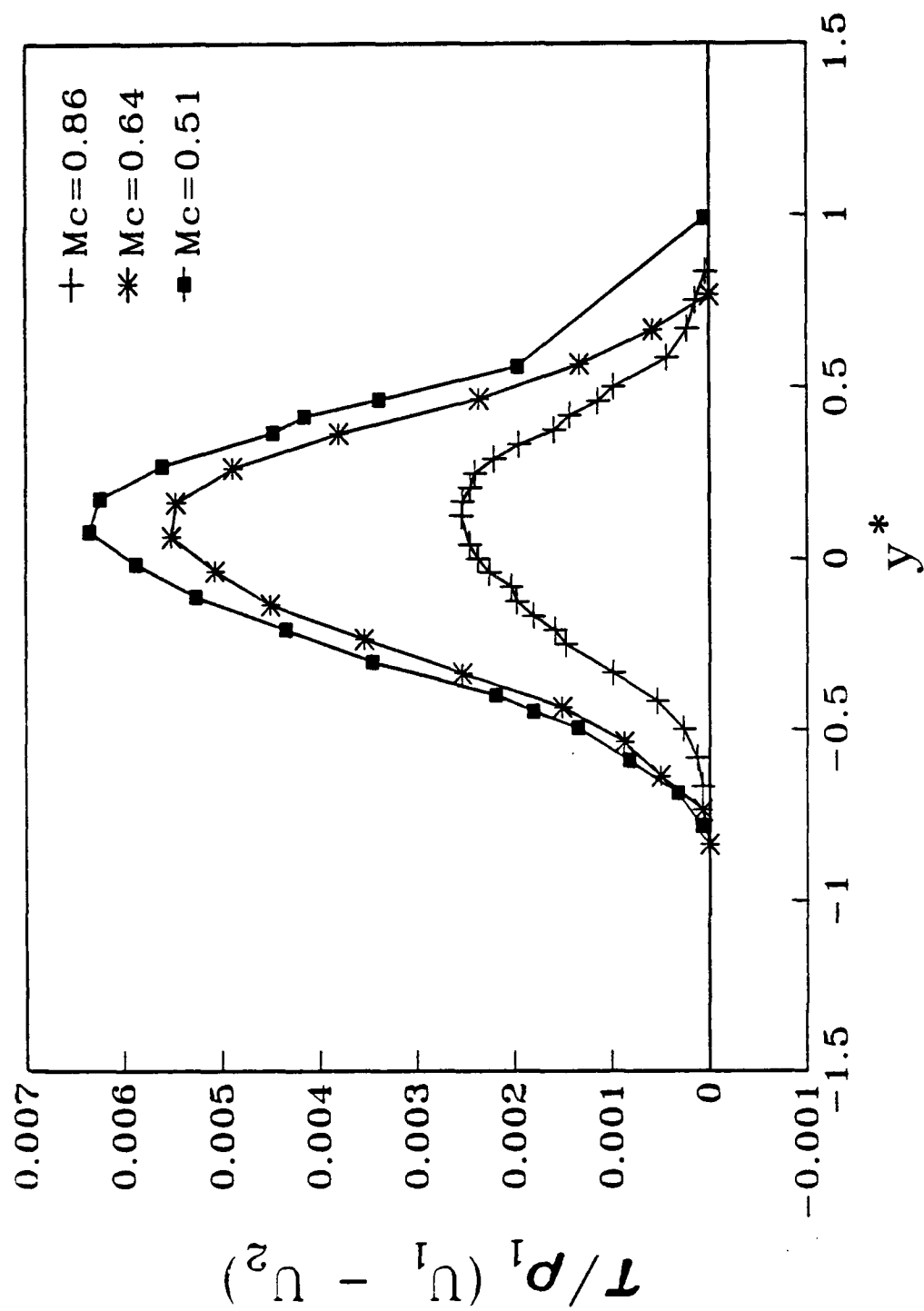
Fig. 16 Shear stress calculated from the velocity profiles

61
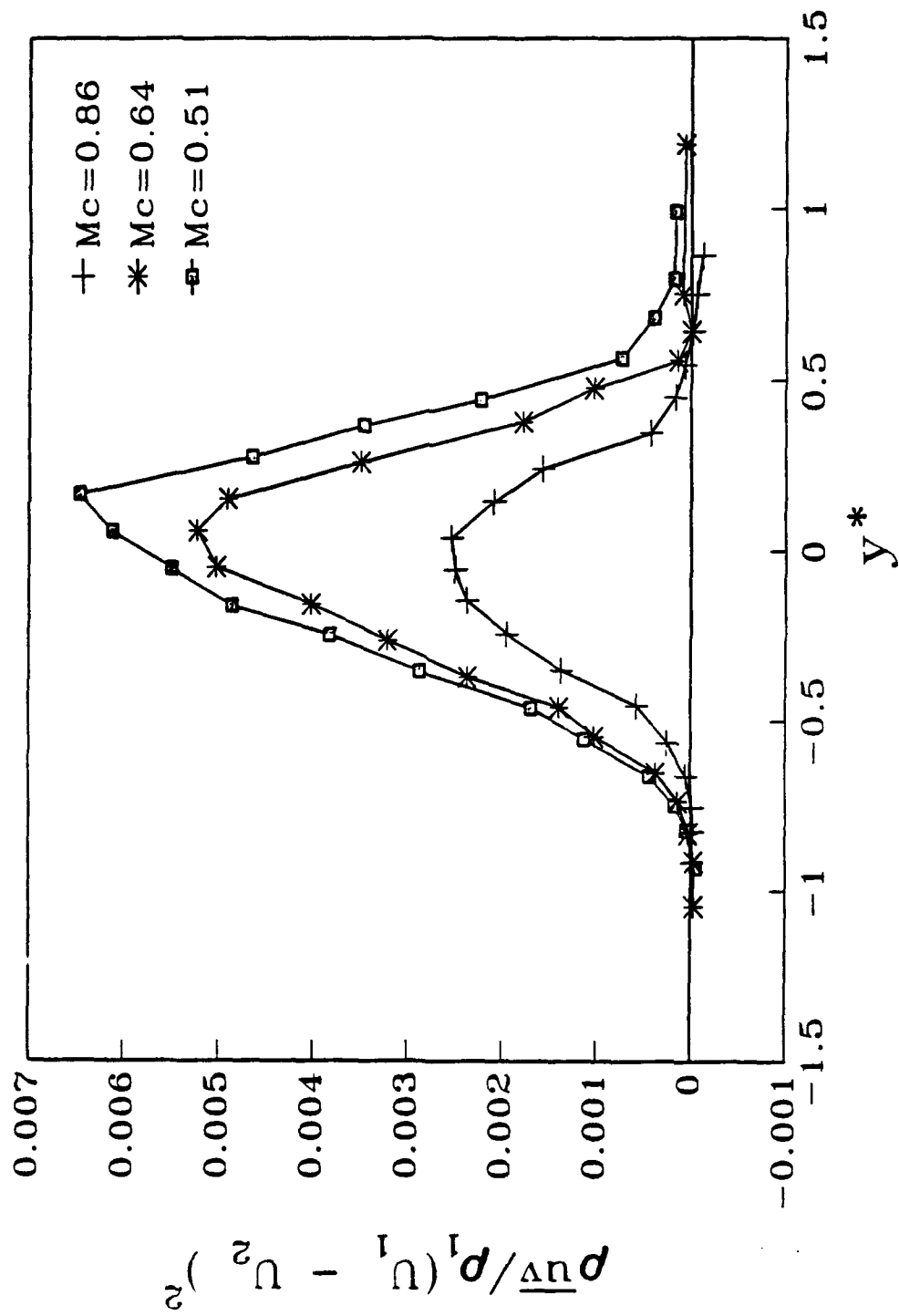
Fig. 17 Reynolds stress profiles in the fully developed region normalized by the density ratio

Coherence for Varied Streamwise Separations
M_c=0.51 x_1=162mm y^*=0 z=−30mm

δ_ω =17mm

——	dx= 9mm
- - -	dx=30mm
········	dx=80mm

Coherence for Varied Streamwise Separations
M_c=0.86 x_1=162mm y^*=−0.15 z=−30mm

δ_ω =24mm

——	dx = 12 mm
- - -	dx = 24 mm
········	dx = 30 mm
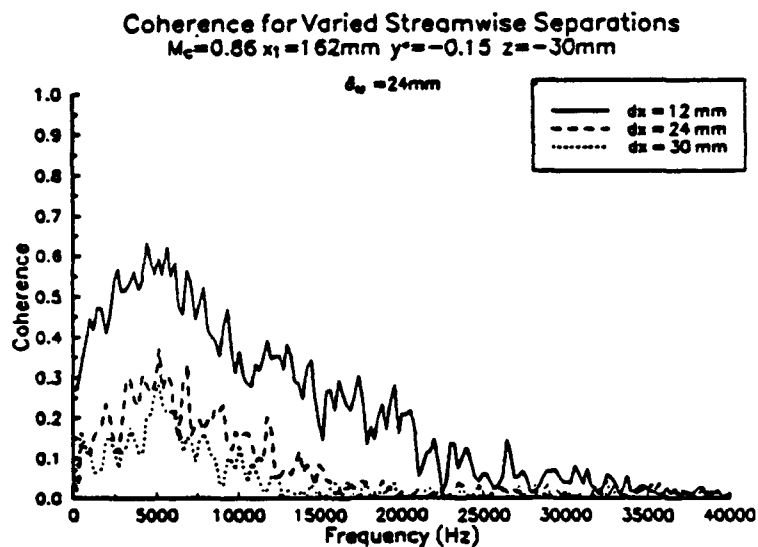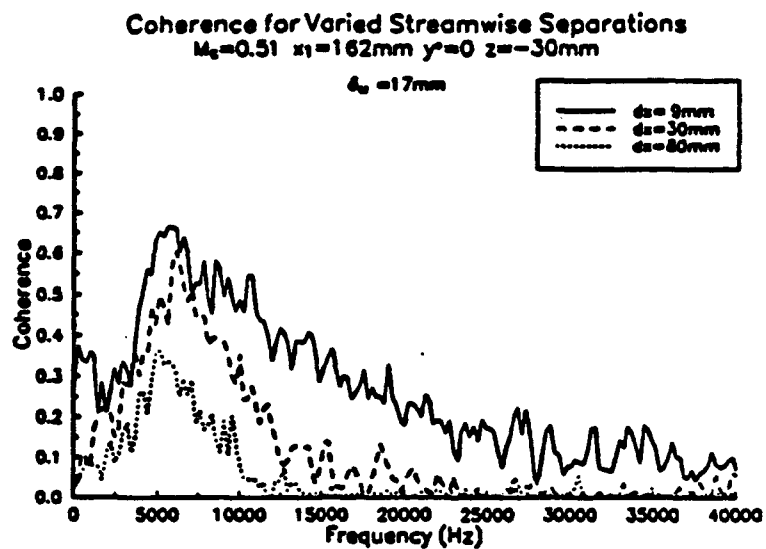
Fig. 18 Streamwise coherence for various separation distances in the fully developed region: (a) case 1 and (b) case 2.

63
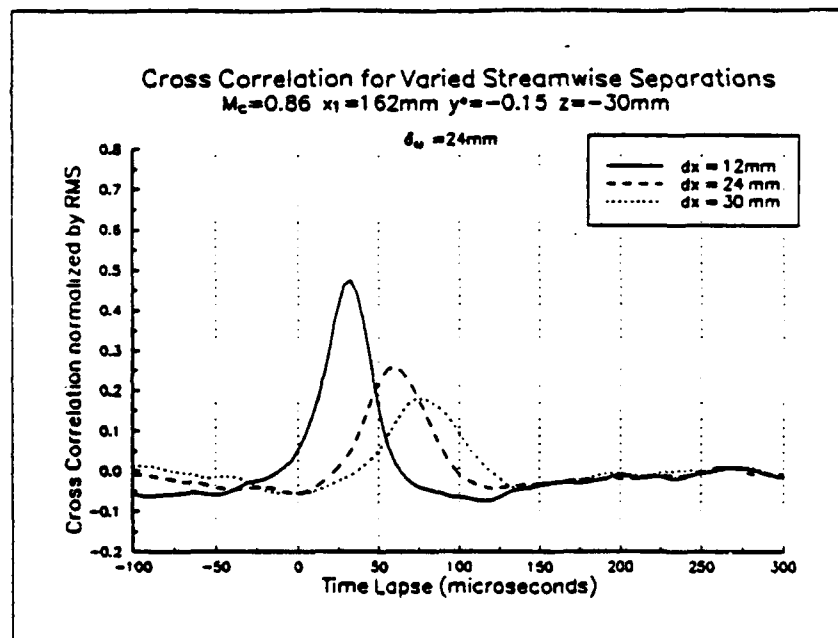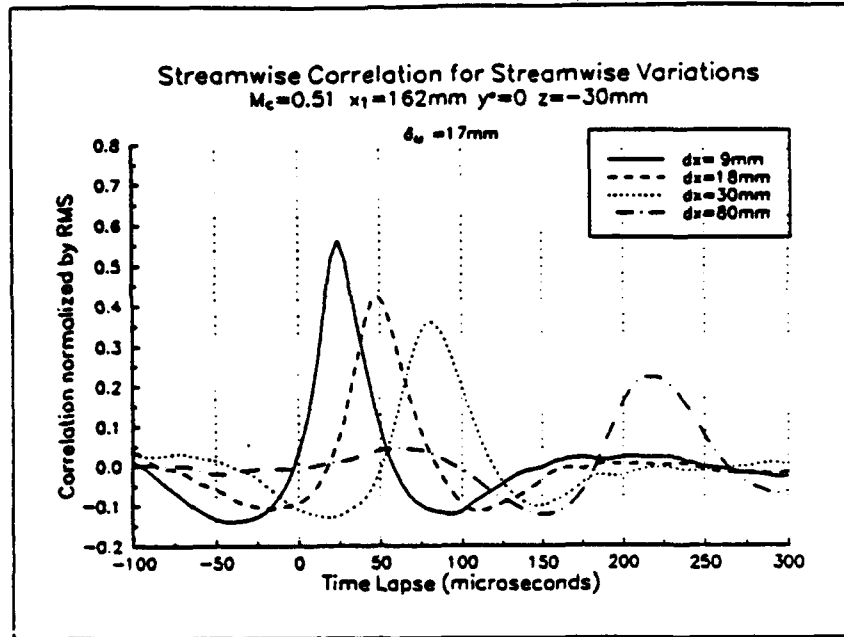
Fig. 19 Streamwise space-time correlations for various probe separations in the fully developed region: (a) case 1 and (b) case 2.

U_C distribution

$M_c=0.51$ $y^\circ=-0.21$ $x_1=162mm$ $x_2=180mm$ $z=-30mm$

Average $U_c=332m/s$

U_C distribution

$M_c=0.51$ $y^\circ=0$ $x_1=162mm$ $x_2=180mm$ $z=-30mm$

Average $U_c=355m/s$
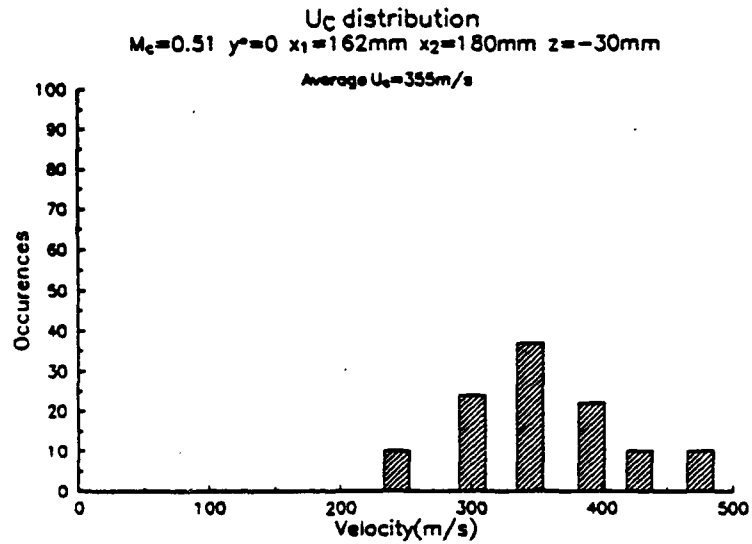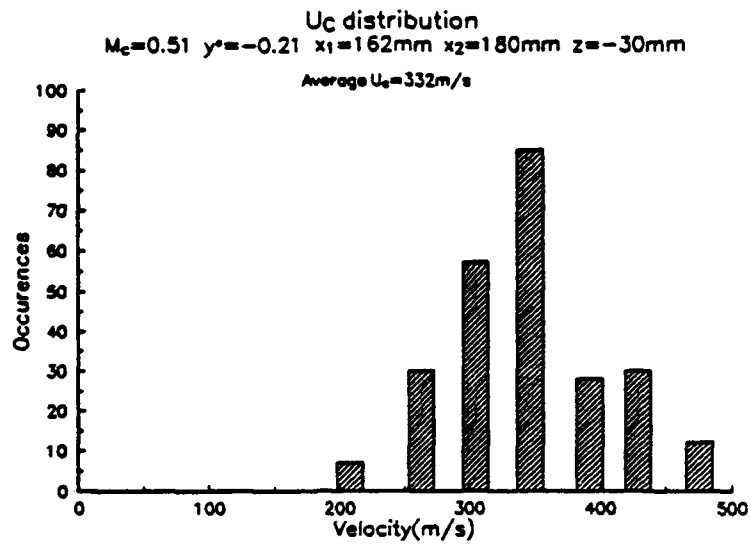
Fig. 20 Histogram of U_c at various lateral positions in the fully developed region for case 1.
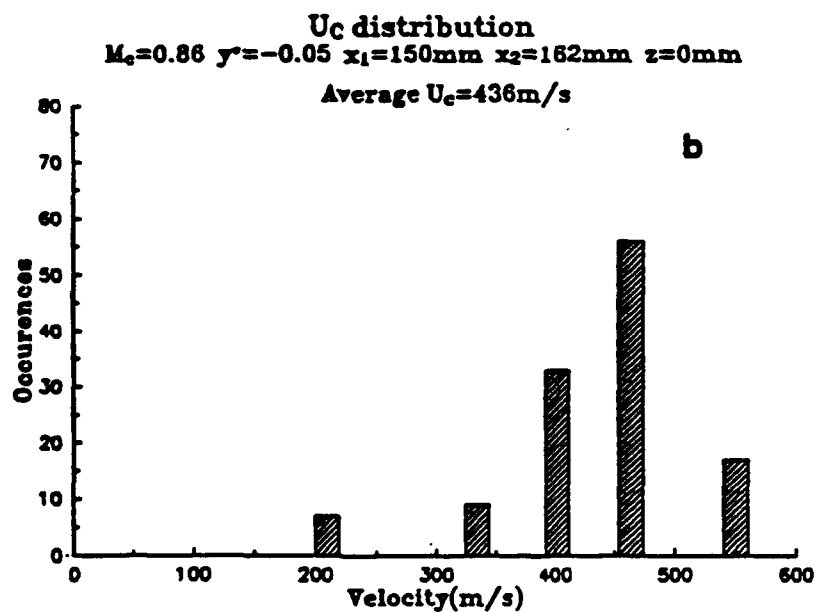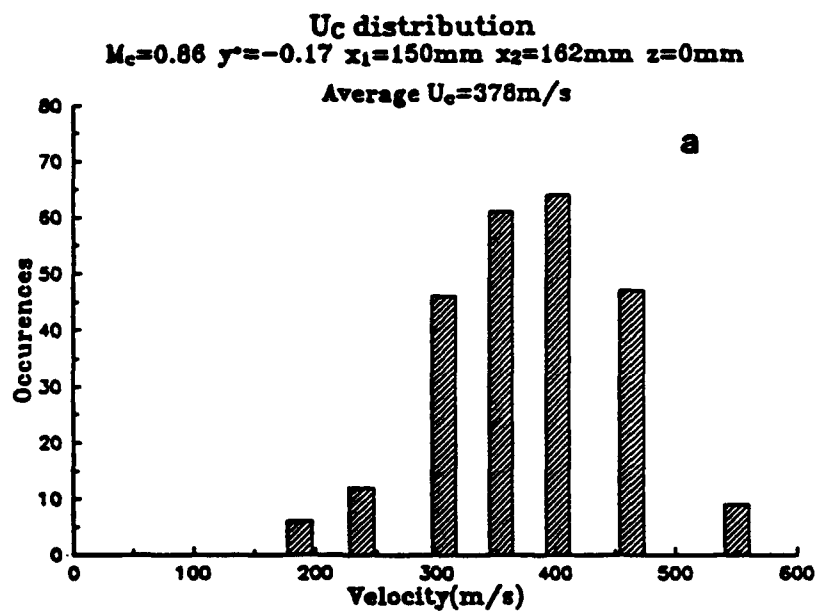
Fig. 21 Histograms of U_c at various lateral positions in the fully developed region for case 2.
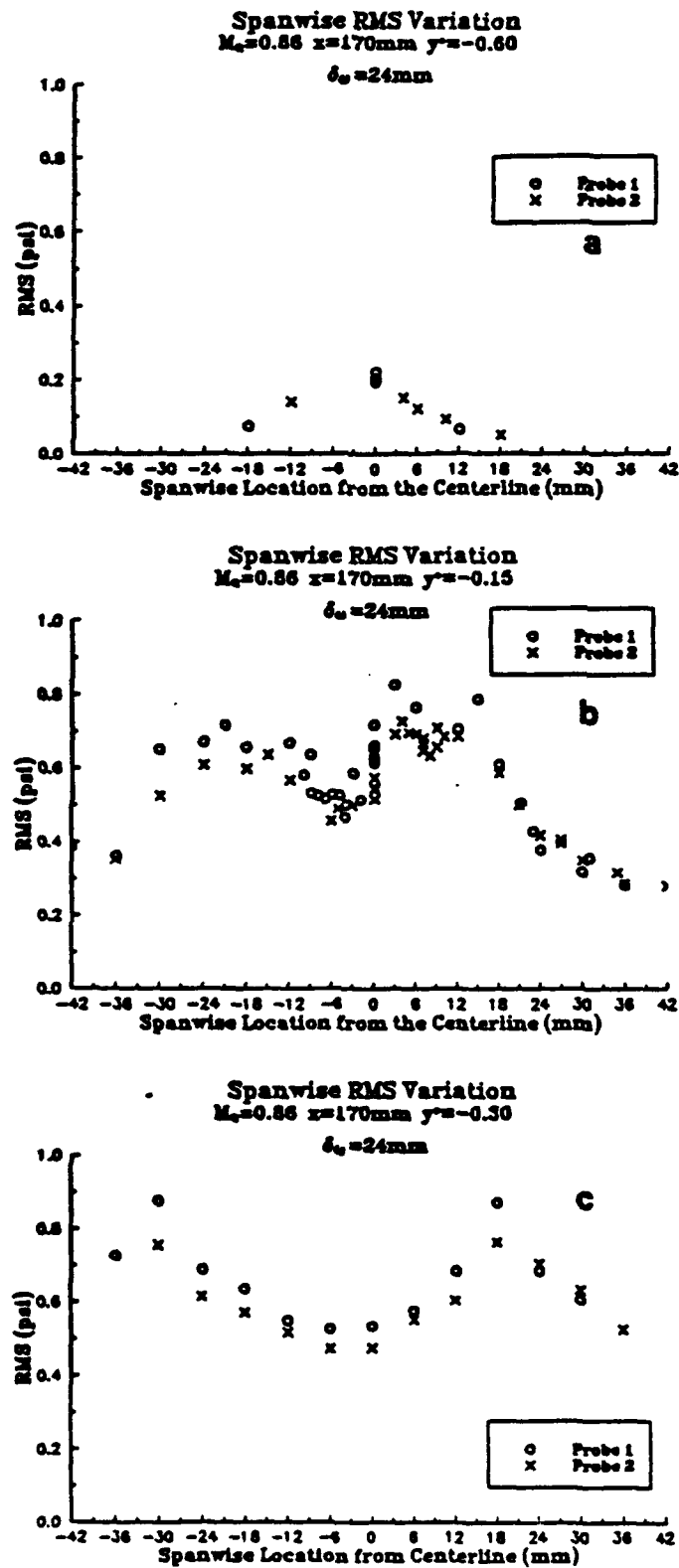
Fig. 22 Root mean square pressure fluctuations across the span of case 2 in the developed region at $y^* =$ (a) -0.6, (b) -0.15, and (c) 0.06.
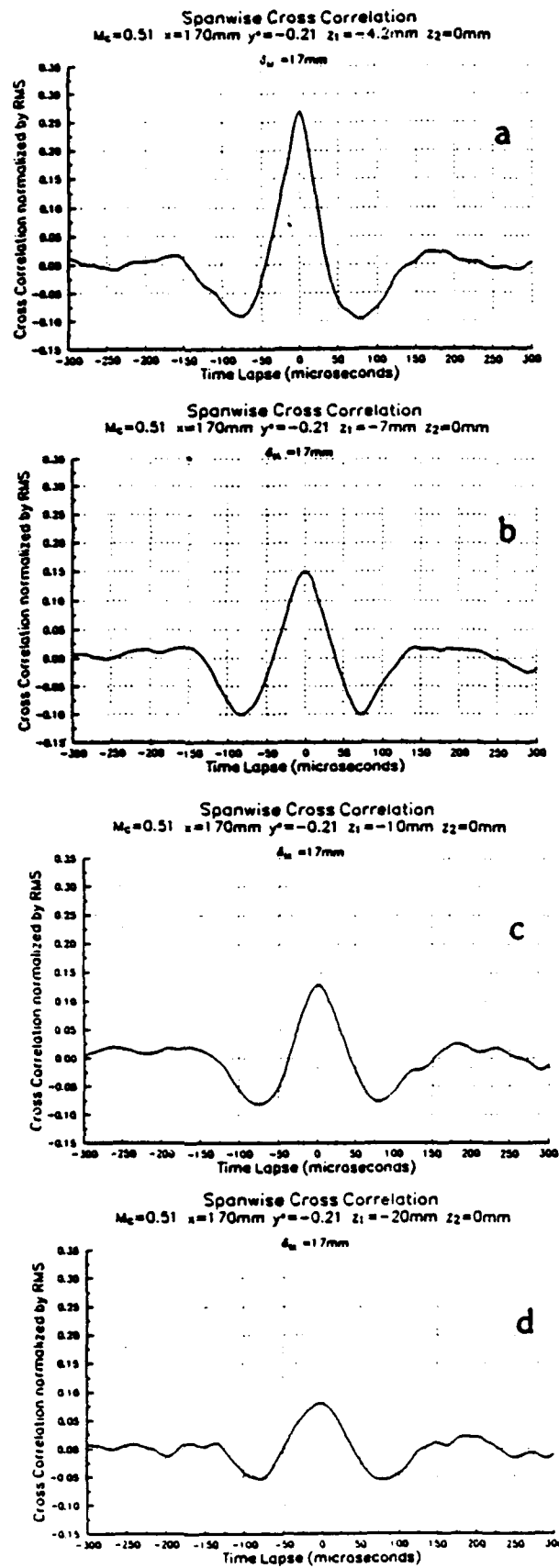
Fig. 23 Spanwise space-time correlations for varied spanwise probe separations in the fully developed region of case 1.
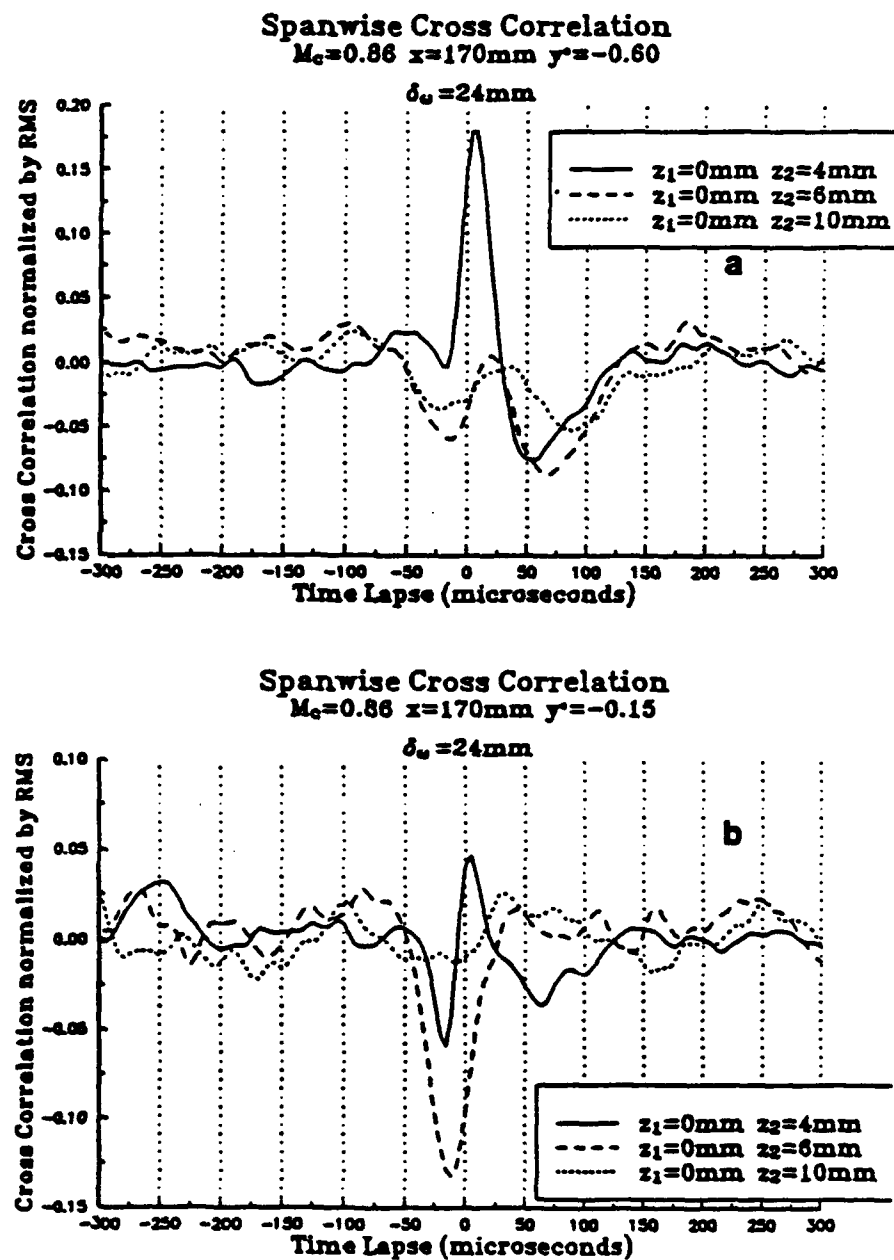
Fig. 24 Spanwise space-time correlations for varied spanwise probe separations and for varied lateral locations for case 2.

69

100 mm   50 mm   0

200 mm   150 mm
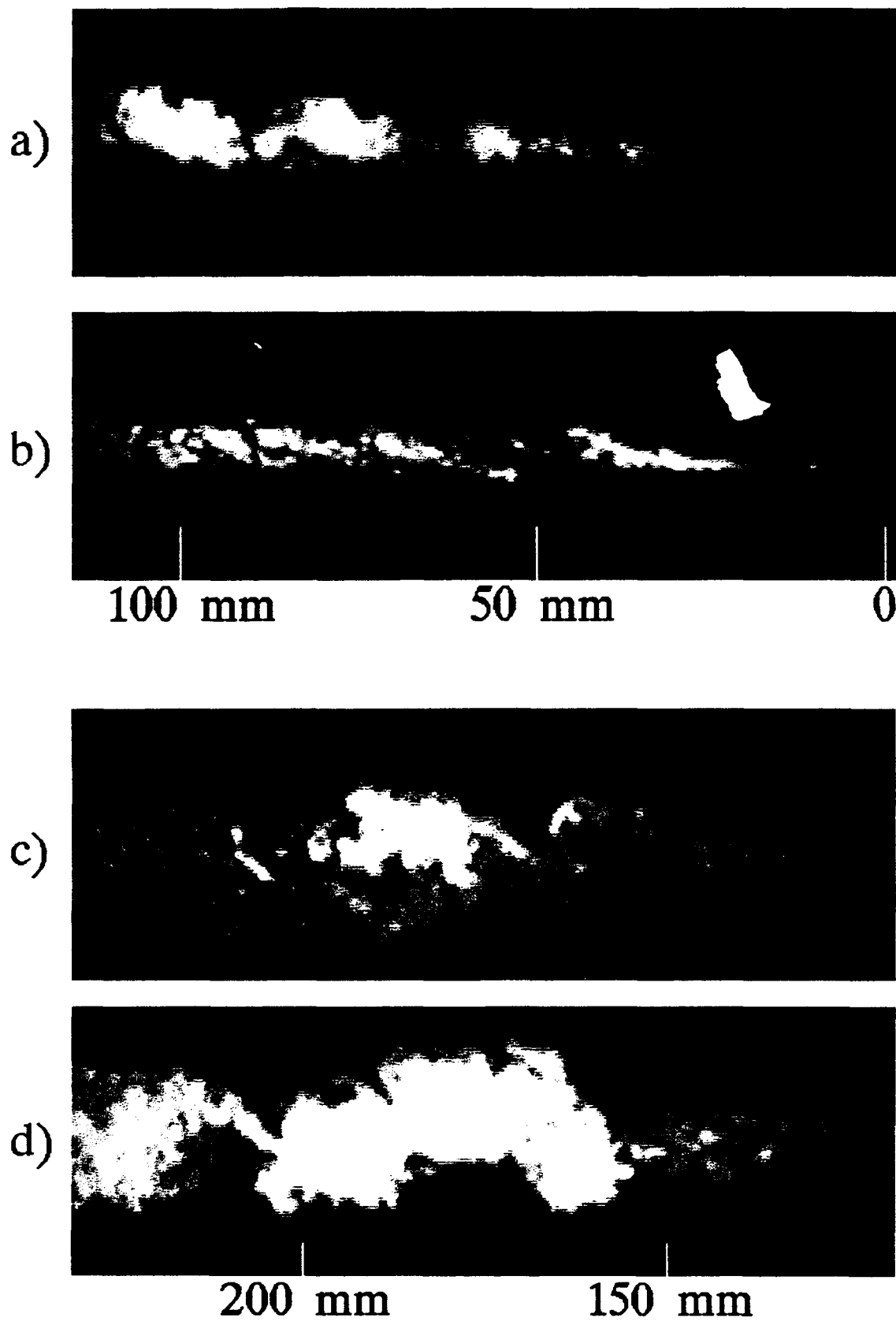
Fig. 25   Streamwise-Transverse (X-Y) view in the developing (a & b) and fully developed (c & d) regions for M_c=0.51

a)

b)

100 mm   0

c)

200 mm   150 mm
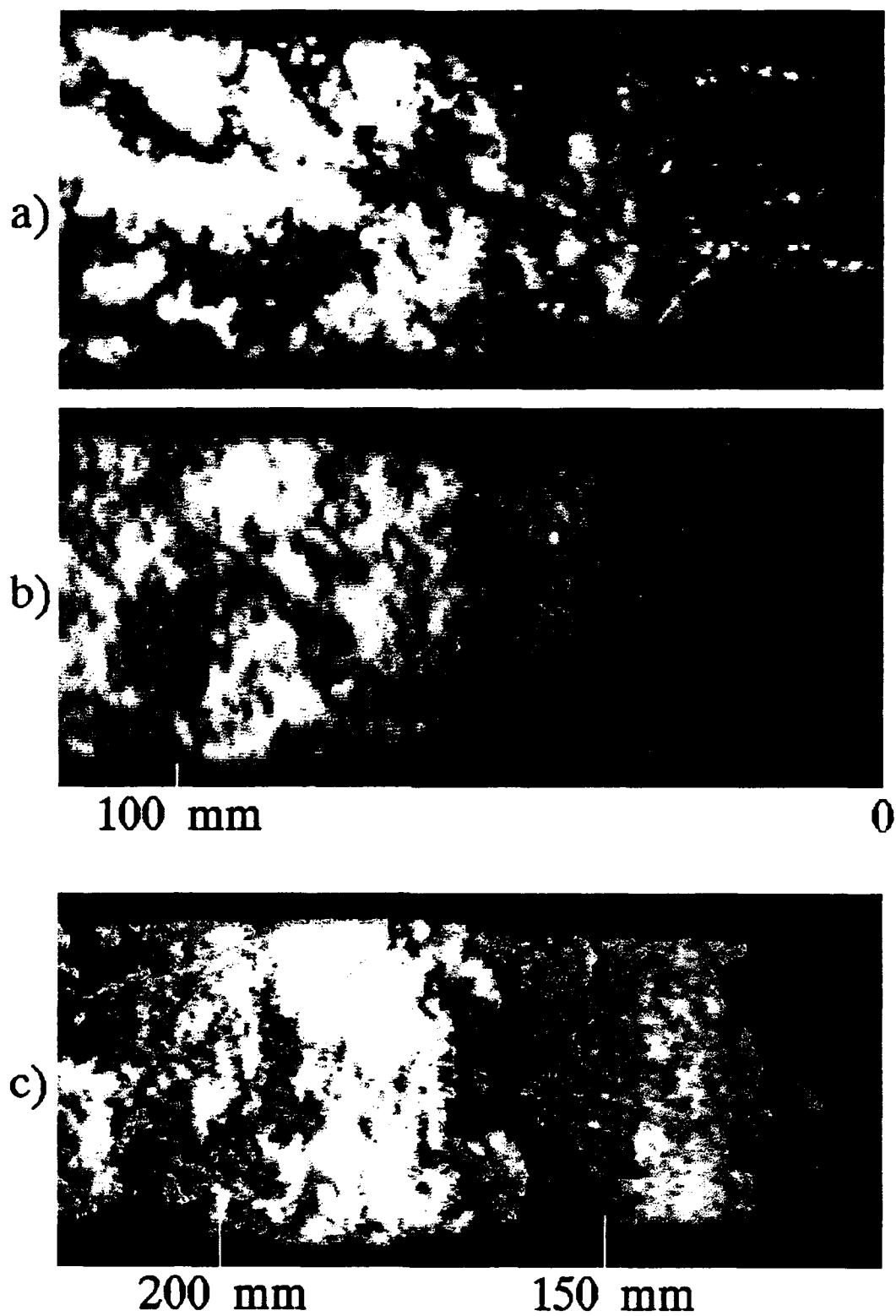
Fig. 26 Plan (X-Z) view in the developing (a & b) and fully developed (c) regions
for $M_c = 0.51$

71
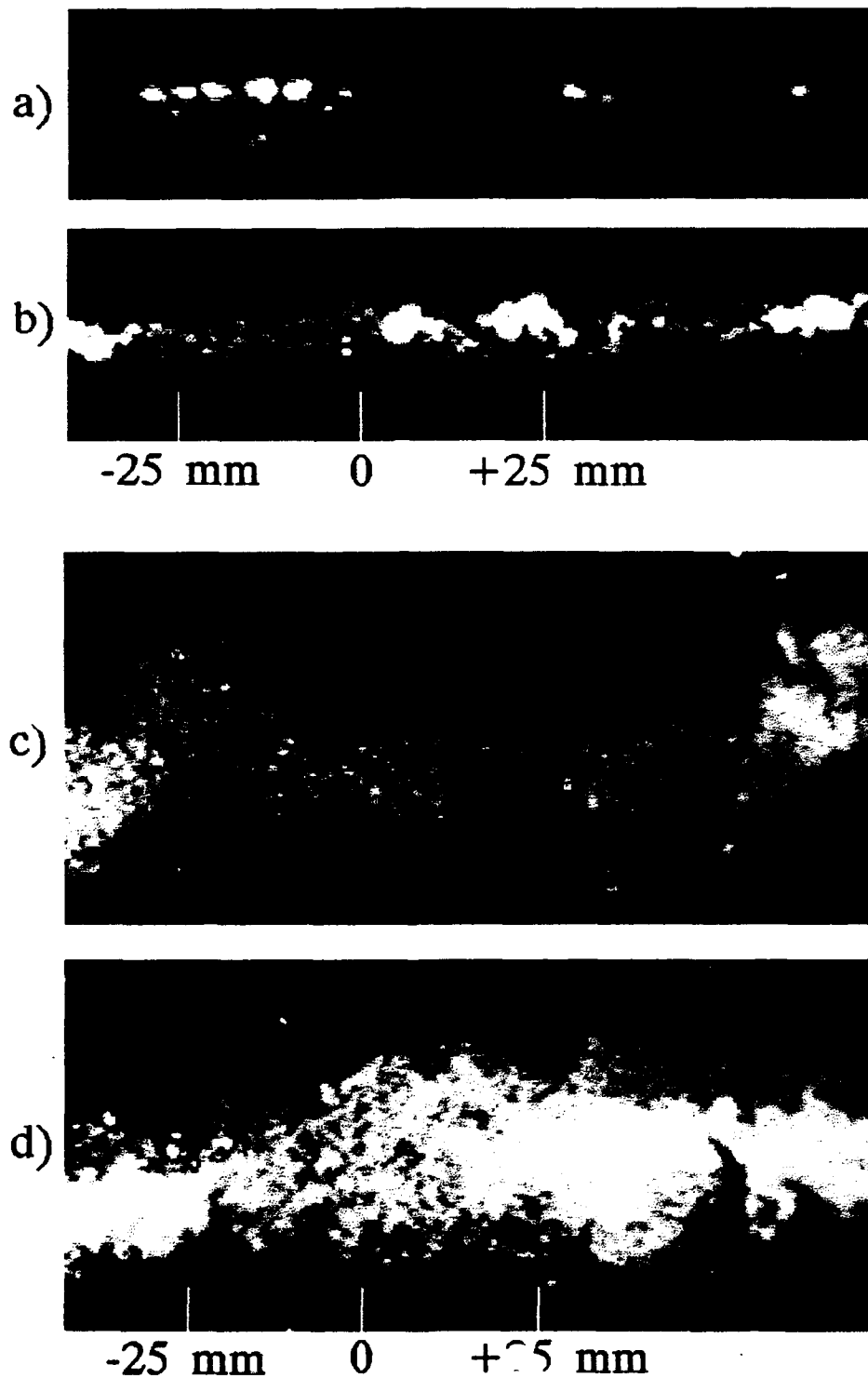
Fig. 27 Spanwise (Y-Z) view in the developing (a & b) and fully developed (c & d) regions for M_c=0.51
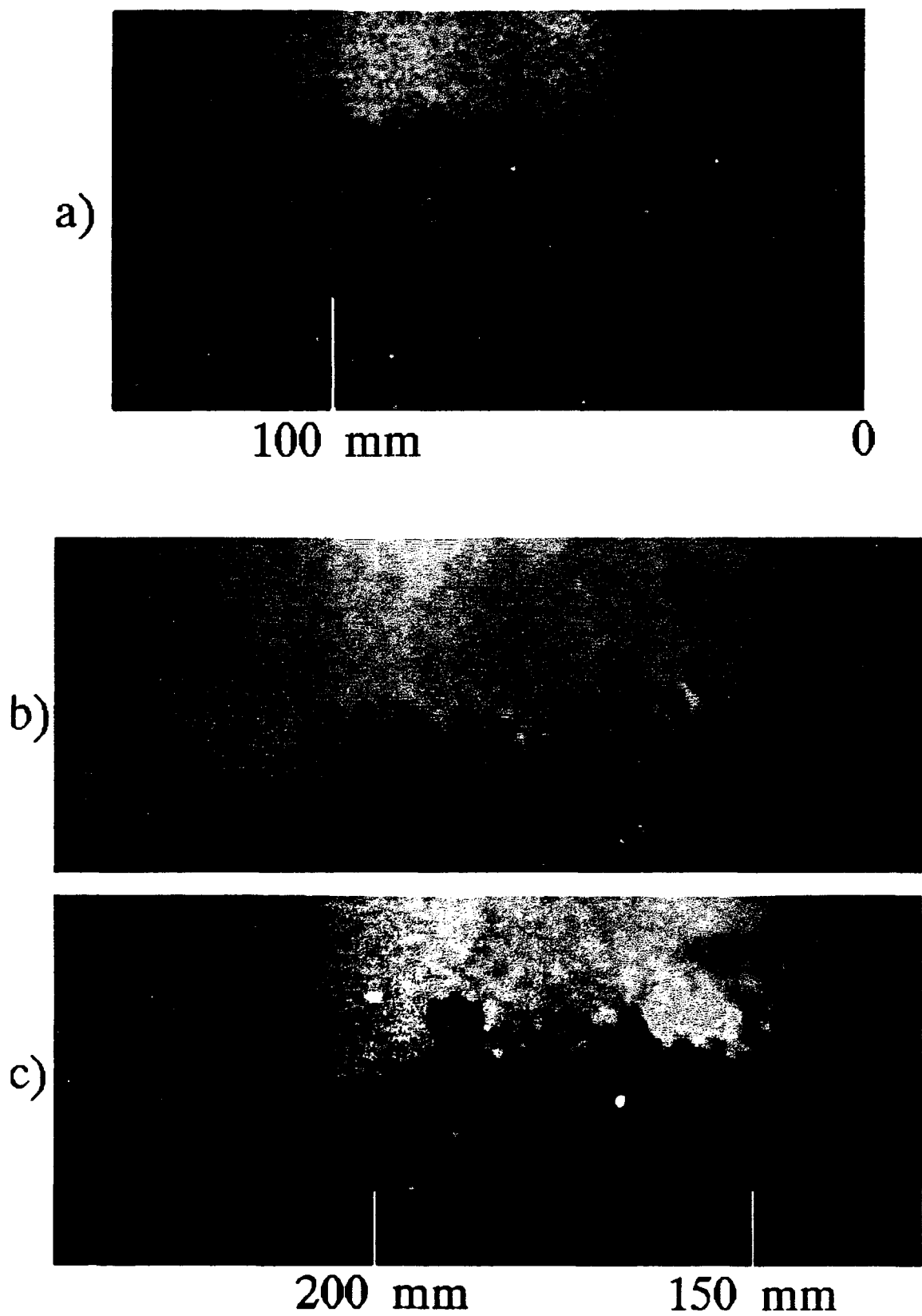
Fig. 28 Streamwise-Transverse (X-Y) view in the developing (a) and fully developed (b & c) regions for M_c=0.86

100 mm   0

200 mm   150 mm

Fig. 29 Plan (X-Z) view in the developing (a) and fully developed (b & c) regions
for $M_c = 0.86$

Particle Locations for Case 1a
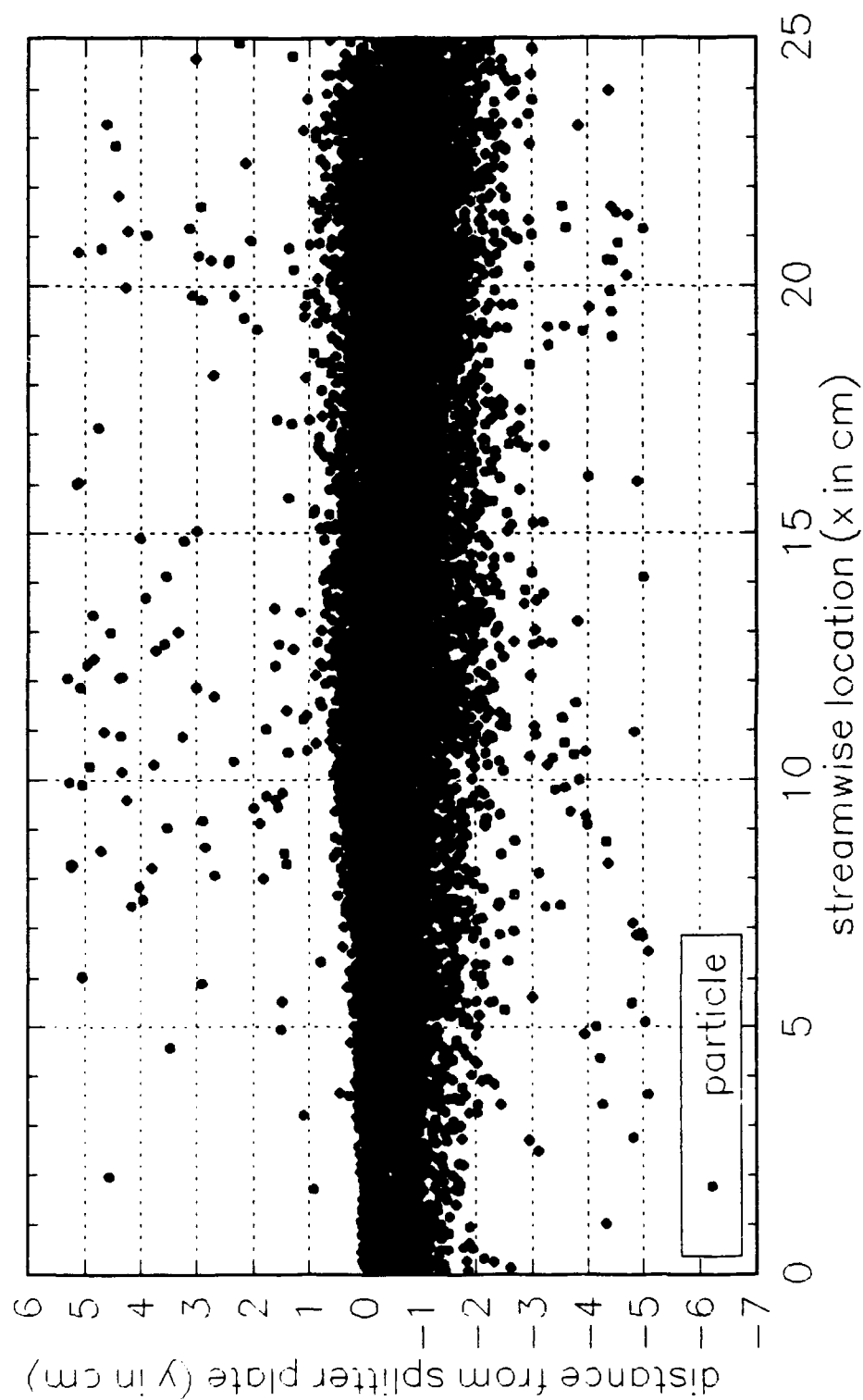
Fig. 30 Particle locations for Case 1a: $M_c = 0.51$, particle size = 1-8μm, $St_\delta = 7$

Fig. 31 Particle locations for Case 1b: $M_c=0.51$, particle size $= 15\text{-}20\mu m$, $St_\delta = 84$

Particle Locations for Case 1c
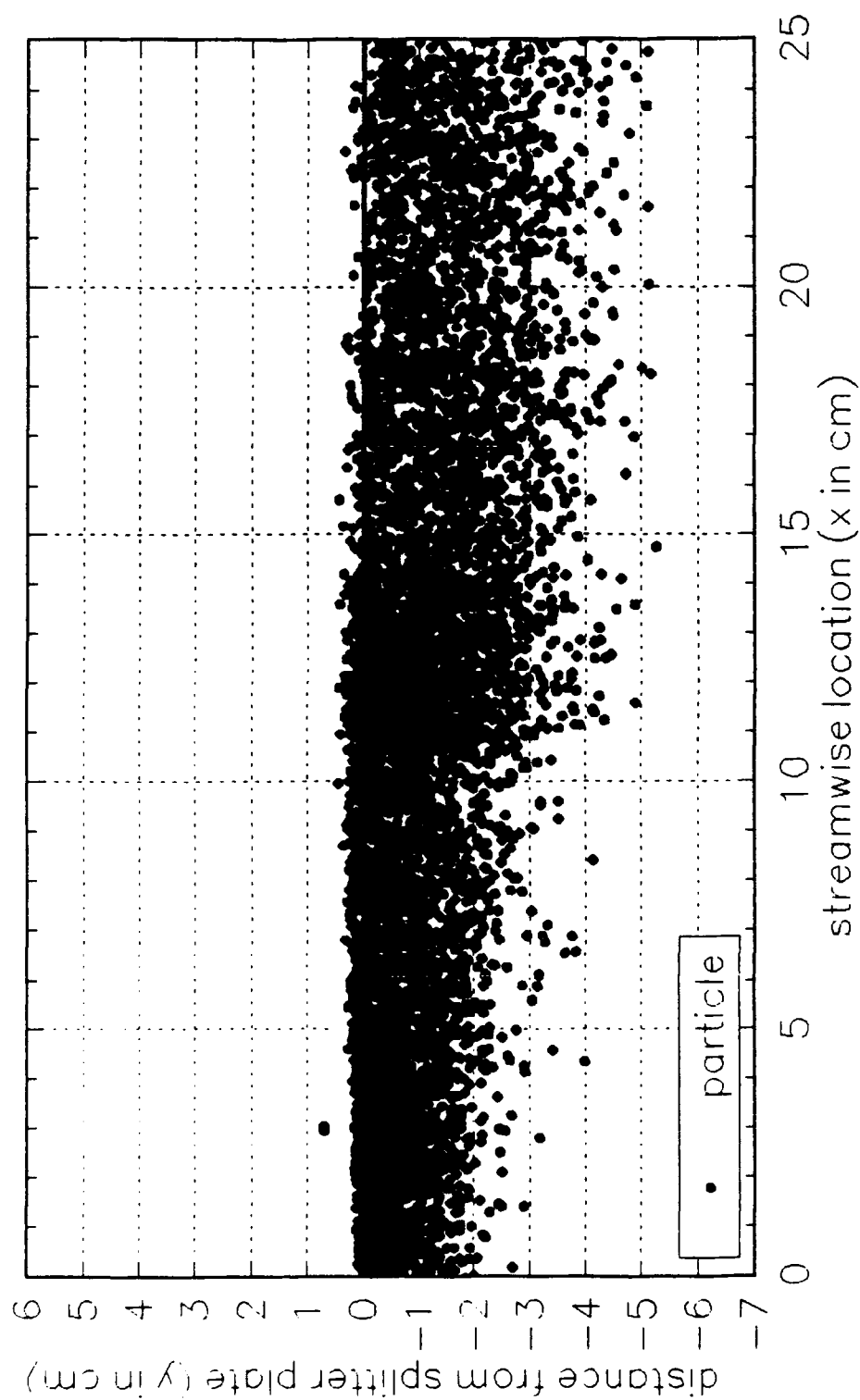
Fig. 32 Particle locations for Case 1c: M_c =0.51, particle size = 10-65μm, St_δ = 1116
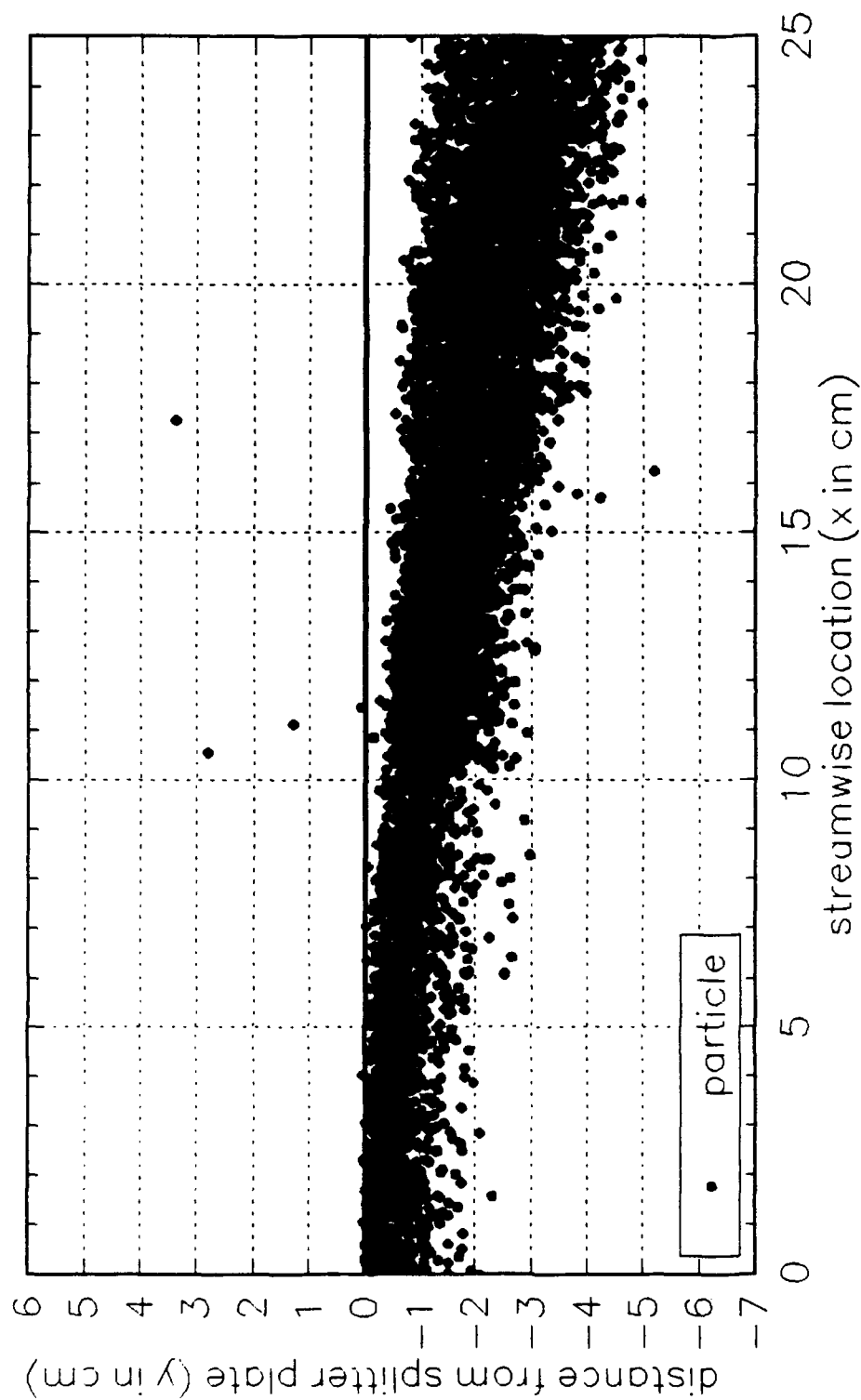
Particle Locations for Case 2a

Fig. 33 Particle locations for Case 2a: $M_c = 0.86$, particle size = 1-8μm, $St_\delta = 12$

Particle Locations for Case 2b
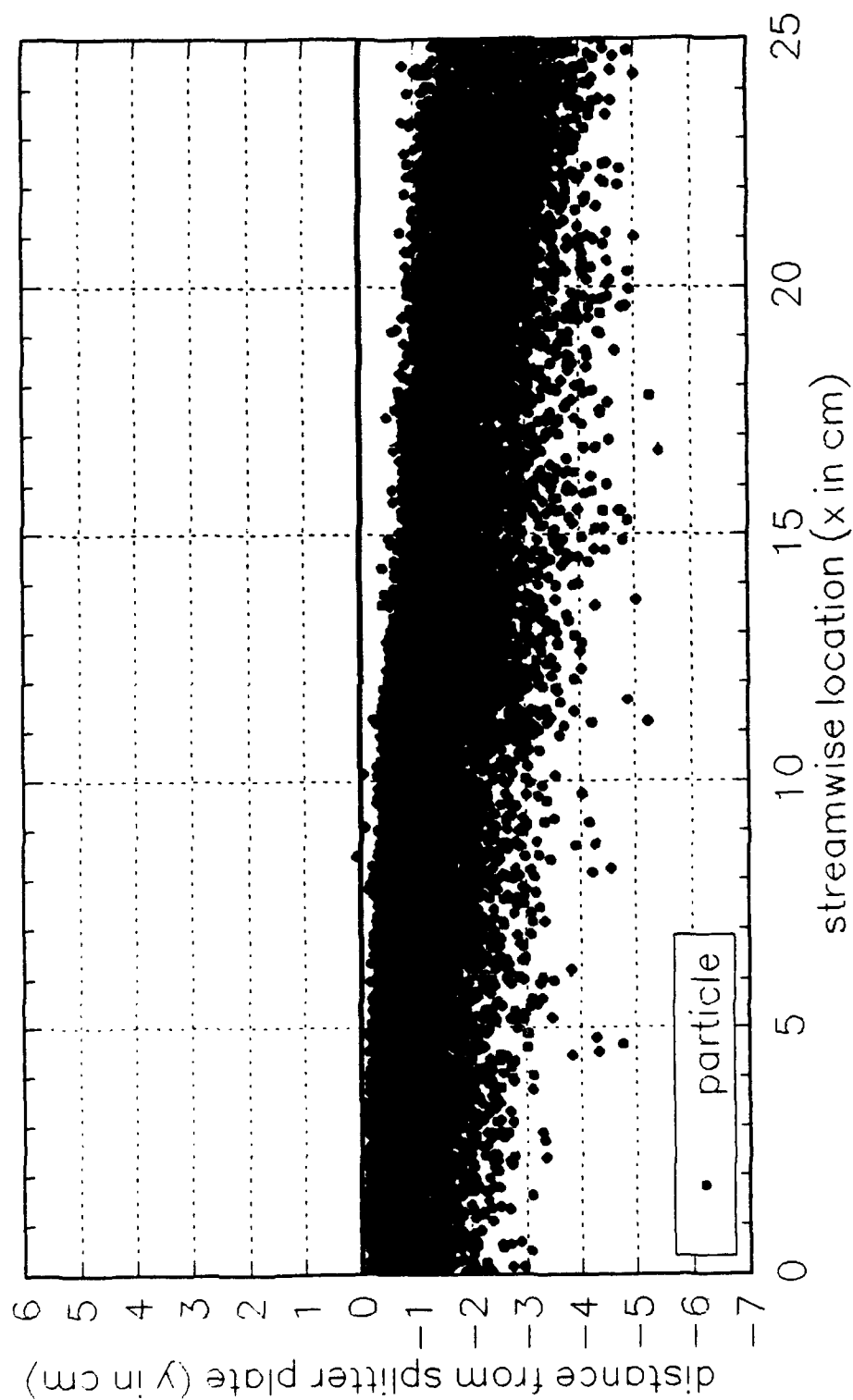
distance from splitter plate (y in cm)

streamwise location (x in cm)

particle

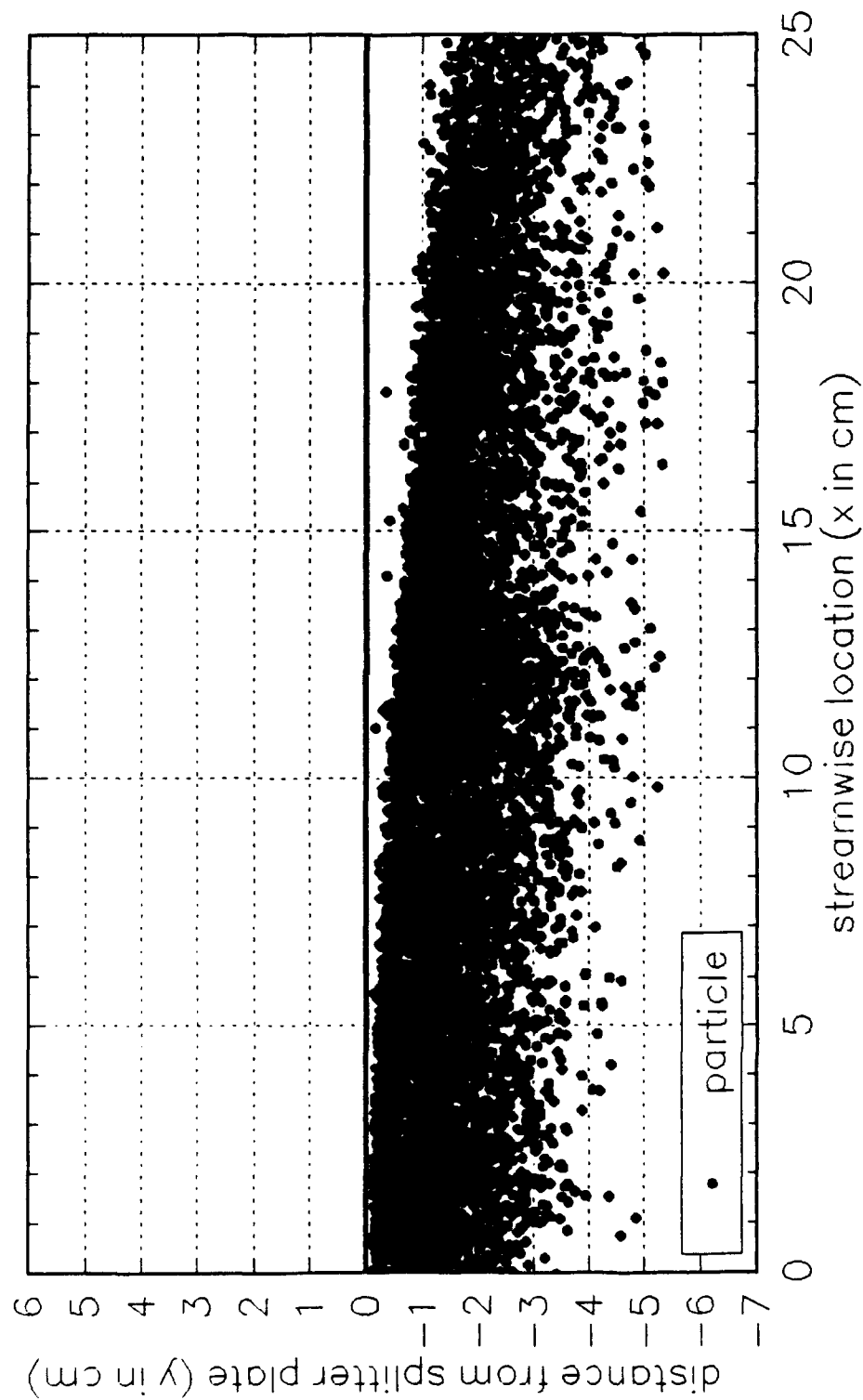Fig. 34 Particle locations for Case 2b: $M_c=0.86$, particle size $= 15\text{-}20\mu m$, $St_\delta = 136$

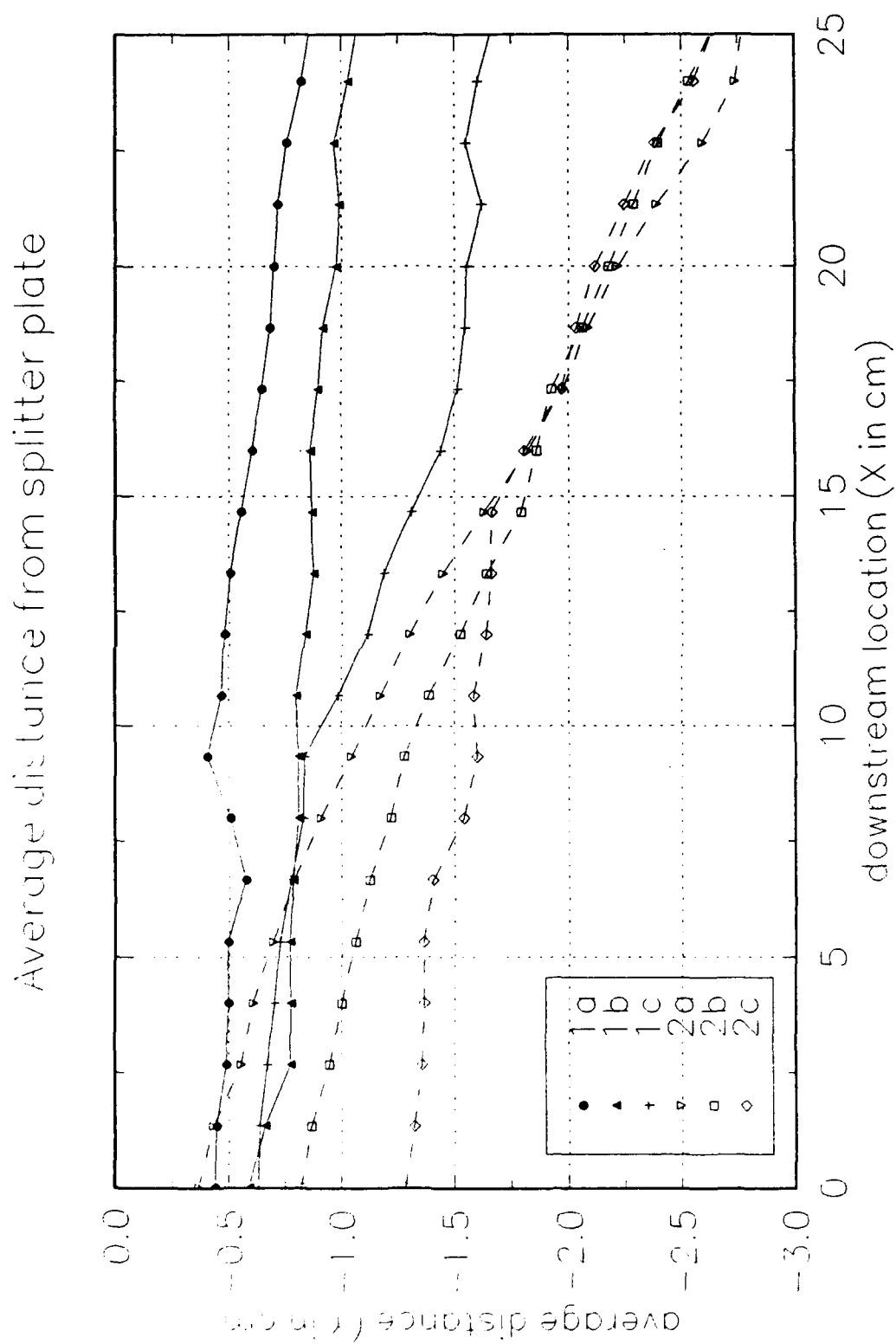Fig. 35 Particle locations for Case 2c: M_c=0.86, particle size = 60-65μm, St_b = 1995

Fig.36 Particle average location relative to the splitter plate